



---

## FABRICATION AND CHARACTERIZATION OF SOLUTION PROCESSED THIN FILM SOLAR CELLS

---

*Author:*

Patrick Tonui

*Supervisor:*

Prof. Genene Tessema Mola

A thesis submitted for the fulfilment of the requirements for the Doctoral

Degree in Physics

School of Chemistry and Physics

College of Agriculture, Engineering and Science

University of KwaZulu-Natal, Pietermaritzburg Campus

South Africa.

2018

# Preface

The research contained in this thesis was completed by the candidate under supervision and guidance of Professor Genene Tessema Mola in the Discipline of Physics, School of Chemistry and Physics in the College of Agriculture, Engineering and Science-University of Kwazulu-Natal(CAES-UKZN). This research was financially supported by CAES-UKZN, the National Research Foundation funds-SA and Masinde Muliro University of Science and Technology, Kenya. The content of this work has not been submitted in any form to another University, and where work of other authors is made use of, it is duly acknowledged in the text. Results reported herein are due to investigations by the candidate.

Signature(Student):



Date: 15<sup>th</sup> November, 2018

Signature(Supervisor):.....Prof. .G.T. Mola..... Date:...19-02.-2019

# Abstract

This research focused on developing new organic and inorganic semiconductor materials and techniques for use in design and fabrication of organic photovoltaic solar cells. Despite OPVs having benefitted from material development and device preparation conditions optimization, the power conversion efficiency(PCE) of perovskite based solar cells is slightly over 22% while that of polymer based counterparts is still relatively low close to 13%. This is attributed to narrow optical absorption range in the solar spectrum and poor charge transport.

Reproducibility, stability, durability and lifetime in addition to use of toxic lead and chlorinated solvents in OPV still remain major challenge to overcome before commercialization. Optimization of photoactive layer structure, interfacial layers and morphology is a major factor influencing the improvement of OPV device performance. Although organic solar cells, polymer solar cells and perovskite solar cell are at different stages of development, it is important to note that they are fabricated using similar procedures and encounter similar challenges.

Bimetallic nanocomposites were successfully synthesized and used to optimize the fabricated perovskite and polymer solar cells. Incorporation of narrow bandgap metal nanoparticles were employed at various layers as hole transport layer, electron transport layer and in the photoactive layer in order to investigate their effect on optical absorption, charge extraction and transport. Results indicated that bimetallic nanoparticles significantly improve the photovoltaic device performance through surface plasmonic resonance effects.

## **Dedication**

To my late father who could not live to taste what he invested in me. To my dear mother who never cease to pray for me always.

## DECLARATION 1- PLAGIARISM

**Patrick Tonui, declare that:**

1. The research reported in this thesis, except where otherwise indicated, is my original research.
2. This thesis has not been submitted for any degree or examination at any other university.
3. This thesis does not contain other persons data, pictures, graphs or other information, unless specifically acknowledged as being sourced from other persons.
4. This thesis does not contain other persons' writing, unless specifically acknowledged as being sourced from other researchers. Where other written sources have been quoted, then:
  - Their words have been re-written but the general information attributed to them has been referenced.
  - Where their exact words have been used. then their writing has been placed in italics and inside quotation marks, and referenced.
5. This thesis does not contain text, graphics or tables copied and pasted from the Internet, unless specifically acknowledged, and the source being detailed in the thesis and in the references sections.

Signature(Student):



Date: 15<sup>th</sup> November, 2018



## CONFERENCES, WORKSHOPS AND SEMINARS

1. College of Agriculture, Engineering and Science- **UKZN, Durban- South Africa**  
Research and innovation day, (26<sup>th</sup> October, 2016).
2. College of Agriculture, Engineering and Science- **UKZN, Durban- South Africa**  
Research and innovation day, (25<sup>th</sup> October, 2017).
3. **University of Pretoria, South Africa.** Postgraduate Spring School on Solar Energy  
and Photosynthesis, (1<sup>st</sup> to 5<sup>th</sup> October, 2018).
4. College of Agriculture, Engineering and Science- **UKZN, Durban- South Africa**  
Research and innovation day, (25<sup>th</sup> October, 2018).

## DECLARATION

### **Declaration - Publications**

My role in each paper is indicated below each publication.

1. Authors :**Mbuyise, X. G.**; Tonui, P.; Mola, G. T., The effect of interfacial layers on charge transport in organic solar cell. *Physica B: Condensed Matter* 2016, 496, 34-37.

My role in this research article was to analyze data, report results, draft manuscript, edit and submit to co-authors for editing before submitting for publication.

2. Authors :**Tessema Mola, G.**; Mbuyise, X. G.; Oseni, S. O.; Dlamini, W. M.; Tonui, P.; Arbab, E. A.; Kaviyarasu, K.; Maaza, M. In Nanocomposite for Solar Energy Application, *Nano Hybrids and Composites, Trans Tech Publ: 2018; pp 90-107.*

My role in this review article was to conduct a wide book chapter review, draft a section of the manuscript, edit bibliography and submit to co-authors for editing before submitting for publication.

**Chapter 3** Title : Perovskites photovoltaic solar cells: overview of current status

Authors : **Patrick Tonui**, Saheed Oseni, Gaurav Sharma, Qingfeng Yan and G. T. Mola

Status : Published (*Renewable & Sustainable Energy Reviews* ( 441), 33, 2017).

My role in this review article was to conduct a in-detpth review, draft the manuscript and submit to co-authors for editing before submitting for publication.

**Chapter 4** Title: Metal nano-composite as charge transport co-buffer layer in perovskite based solar cell

Authors :**Patrick Tonui**, Elhadi Abdalla Adam Arbab, and G. T. Mola

Status : Published (*Journal of Physics and Chemistry of Solids* ( 09), 019, 2018).

My role in this article was to conduct experiments, analyze the data, report and edit the manuscript until it was published.

**Chapter 6** Title : Electron transport co-buffer layer for improved charge extraction in polymer solar cell

Authors :**Patrick Tonui** and G. T. Mola

Status : in press (*Journal of Electronic Materials* ( xxx), xxxx, 2018).

My role in this article was to conduct experiments, analyze the data, report and edit the manuscript until it was published.

# Acknowledgement

First and foremost I thank God for looking after me during these past years and for granting me the ability to complete this degree.

My gratitude goes to Masinde Muliro University of Science & Technology and University of Kwazulu-Natal for the joint scholarship they offered me.

Many individuals have contributed either directly or indirectly to this research but I am indebted to my supervisor Prof Mola G. T for welcoming me to his research group, overseeing the work, reading the write-up, his helpful guidance in preparation of the thesis and for always being available even when other duties of being the Head of Physics department demanded all his time.

All my lecturers from Physics department and the entire staff for their timely, encouragement and advice which I greatly appreciate. I also appreciate the assistance from Ntombozuko Matyumza and Loreka Beukes of Microscopy and Microanalysis Unit (MMU) School of Life Sciences.

My greatest appreciation however goes to my wife Norah for encouraging me to leave my lecturing career at Masinde Muliro University of Science & Technology and realize my dream of returning to the student life and to my family for the sacrifice, support and encouragement during the time away from home.

In particular I would like to thank Dr. Elhadi A. A. Arbab for his inspiration, constant encouragement and excellent insight into how to get things done. Others are Dr. Saheed Oseni, Mohammed Saeid, Xolani Mbuyise and Yotasha Thaver all of whom were members of our research group for their invaluable support, discussions, patience and encouragement during the entire research.

To all may God really bless you.

## LIST OF FIGURES

1.1	World energy consumption quadrillion Btu. . . . .	2
1.2	Globally averaged combined land and ocean surface temperature anomaly . . . . .	3
2.1	Working principle of an organic solar cell . . . . .	8
2.2	Diagram of a Dye sensitized solar cell . . . . .	9
2.3	Device architecture of the (a) normal and (b) inverted BHJ OSCs . . .	11
2.4	Structure of tandem solar cell . . . . .	12
2.5	Current–voltage characteristics of an OPV cell . . . . .	16
3.1	Steady growth of power conversion efficiency of perovskite based solar cell . . . . .	23
3.2	Evolution of photovoltaic solar cells . . . . .	24
3.3	Charge transport channels in perovskite solar cells . . . . .	26
3.4	Dependence of the maximum efficiency limit on energy band gap . .	28
3.5	Equivalent electrical circuit for single-junction solar cell. . . . .	30
3.6	Various types of perovskite film preparation . . . . .	31
3.7	Current-voltage characteristics of perovskite solar cell produced by vapour deposition and solution processing . . . . .	34
3.8	Chemical structure of (a) Methyl ammonium and (b) Formamidinium	35
3.9	General crystal structure of $\text{CH}_3\text{NH}_3\text{PbX}_3$ perovskite . . . . .	36
3.10	Steady-state absorption and photoluminescence . . . . .	37
3.11	The effect of stoichiometric ratio of halides in the synthesis of organic lead perovskite . . . . .	39

3.12	The photograph of MAPbBr <sub>3</sub> single crystal film . . . . .	40
3.13	Structure models of (a) during the phase transition from cubic, tetragonal and orthorhombic structures . . . . .	42
3.14	The device structure of PSC . . . . .	43
3.15	Current-voltage(J-V) curves of the champion PSCs . . . . .	45
3.16	Energy levels of the the various materials used as the electron selective contact . . . . .	47
3.17	The SEM cross sectional view of the perovskite film morphology . . . . .	52
3.18	J-V curves of spiro-MeOTAD-based (black curve) and P3HT based devices . . . . .	54
3.19	Examples of most commonly used HTL . . . . .	55
3.20	Best ETM and HTM used in the preparation of high performance perovskite solar cell. . . . .	58
3.21	Chemical structures of (a) (Li-TFSI), (b) TBP and (c) CN (d) Polyvinyl alcohol (e) polyethylenimine . . . . .	60
3.22	The effect of DIO additive on the preparation of perovskite films . . . . .	61
4.1	Illustration of device structure of Psc . . . . .	88
4.2	J-V characteristic of perovskite based solar cells fabricated . . . . .	90
4.3	Space charge limited current for the best 5 fabricated devices. . . . .	92
4.4	Photoluminescence spectra of synthesized Zn, Ag and Ag:Zn BNCs. . . . .	94
4.5	U-V Absorbance of MAI, PbI <sub>2</sub> and PbMAI <sub>3</sub> solutions. . . . .	95
4.6	Ag:Zn BNps Absorbance, transmittance and optical bandgap (inset). . . . .	96
4.7	SEM images of Ag:Zn NPs . . . . .	97
4.8	X-Ray diffraction patterns of Ag:Zn BNCs. . . . .	98
5.1	Illustration of device structure of Psc. . . . .	109
5.2	J-V characteristic curves of device without and with Ag:Cu bimetallic nanoparticles. . . . .	111
5.3	Space Charge limited currents for device with and without Ag:Cu BNCs. . . . .	112

---

5.4	U-V Optical absorbance of devices with and without Ag:Cu BNCs. . .	113
5.5	Synthesized Ag:Cu nano-composite in powder form . . . . .	115
5.6	XRD patterns of the synthesized (a) Ag: Cu NPs . . . . .	116
6.1	Fabricated polymer solar cell structure. . . . .	124
6.2	J-V characteristic curves of solar cell with and without Ag:Cu BNCs. .	126
6.3	Dark Ln J-V characteristic curves of device without(a) and with Ag:Cu BNCs (b). . . . .	127
6.4	Space charge limited current for the best 3 fabricated devices . . . . .	129
6.5	U-V Optical absorbance of devices with and without Ag:Cu BNPs. . .	130
6.6	SEM micrographs showing surface morphology with elemental map- ping of Ag:Cu BNCs powder . . . . .	132
6.7	XRD patterns of the synthesized (a) Ag: Cu NPs . . . . .	134

## LIST OF TABLES

3.1	Optimal device performance reported with different perovskite deposition methods . . . . .	33
3.2	Crystal systems and transition temperatures (K) of $\text{CH}_3\text{NH}_3\text{PbX}_3$ ( $X = \text{Cl, Br, or I}$ ). . . . .	41
3.3	Summary of the device lead free perovskite solar cells . . . . .	46
3.4	Summary of the device evolution and performance of perovskite solar cells . . . . .	48
3.5	Table of Additives and power conversion efficiencies . . . . .	59
4.1	Photovoltaic parameters of reference solar cells . . . . .	89
4.2	Solar cell parameters calculated from J-V curves measured by forward scanning. . . . .	89
4.3	Charge transport parameter for the best four fabricated devices . . . . .	92
4.4	Analysis of XRD of Ag:Zn BNCs. . . . .	99
5.1	J-V characteristic curves of reference solar cell without BNCs. . . . .	110
5.2	Charge transport parameter for the best four fabricated devices . . . . .	112
5.3	EDX data of Ag:Cu core-shell nanoparticles . . . . .	114
5.4	Analysis of XRD of Ag:Cu bimetallic nanoparticles. . . . .	116
6.1	J-V characteristic curves of reference solar cell without Ag:Cu NPs. . . . .	125
6.2	With Ag:Cu NPs. . . . .	125
6.3	Charge transport parameter for the best three fabricated devices . . . . .	129
6.4	EDX data of Ag-Cu core-shell nanoparticles . . . . .	133
6.5	Analysis of XRD of Ag:Cu bimetallic nanoparticles. . . . .	134

# CONTENTS

<i>List of Figures</i> . . . . .	xi
<i>List of Tables</i> . . . . .	xiv
<i>1. General introduction</i> . . . . .	2
1.1 Justification: . . . . .	3
1.2 Aim of thesis . . . . .	4
1.3 Objectives of thesis . . . . .	4
1.4 Outline of this thesis . . . . .	4
<i>References</i> . . . . .	6
<i>2. Literature review</i> . . . . .	7
2.1 General Introduction . . . . .	7
2.1.1 Dye-sensitized solar cells(DSSCs) . . . . .	8
2.1.2 Organic solar cells . . . . .	9
2.1.3 Polymer solar cells . . . . .	9
2.1.4 Hybrid solar cells . . . . .	12
2.1.5 Perovskite based solar cells . . . . .	13
2.2 Nanomaterials in organic photovoltaics . . . . .	13
2.3 Solar cell Parameters . . . . .	15
<i>References</i> . . . . .	18

3. <i>Perovskites photovoltaic solar cells: overview of current status</i> . . . . .	21
3.1 Introduction . . . . .	21
3.1.1 Perovskite based solar cells evolution . . . . .	24
3.1.2 Working of perovskite solar cells . . . . .	26
3.1.3 Solar cell characterization . . . . .	27
3.2 Methods of perovskite film Preparation . . . . .	31
3.3 Organometal halide perovskites . . . . .	34
3.3.1 Composition and properties of perovskites . . . . .	34
3.3.2 Methylammonium lead triiodide ( $CH_3NH_3PbI_3$ ) . . . . .	36
3.3.3 Methylammonium lead tribromide ( $CH_3NH_3PbBr_3$ ) . . . . .	37
3.3.4 Mixed halide perovskite $CH_3NH_3PbI_{3-x}Cl_x$ . . . . .	38
3.3.5 Crystalline perovskite . . . . .	39
3.4 Phase transitions in perovskites . . . . .	41
3.5 Perovskite solar cell architectures . . . . .	42
3.5.1 Mesoporous/mesoscopic structures . . . . .	44
3.5.2 Planar structures . . . . .	44
3.6 Charge transport buffer layers . . . . .	46
3.6.1 Hole transport materials (HTMs) . . . . .	49
3.6.2 Electron transport materials (ETMs) . . . . .	55
3.7 The effect of solvent additives . . . . .	57
3.8 Conclusion . . . . .	61
<i>References</i> . . . . .	64
4. <i>Metal nano-composite co-buffer layer for charge carriers collection in perovskite solar cell</i> . . . . .	85
4.1 Introduction . . . . .	85
4.2 Materials and Methods . . . . .	87
4.2.1 Synthesis of Ag:Zn Nanocomposite . . . . .	87

---

4.2.2	Device fabrication . . . . .	87
4.3	Results and Discussion . . . . .	89
4.3.1	J-V Characteristics . . . . .	89
4.3.2	Charge Transport Properties Analysis . . . . .	91
4.3.3	Photoluminescence Study . . . . .	93
4.3.4	Optical Properties . . . . .	94
4.3.5	Morphology . . . . .	96
4.4	Conclusion . . . . .	100
4.5	Acknowledgments . . . . .	100
	<i>References</i> . . . . .	101
5.	<i>Effect of dual plasmonic resonance absorption in thin film perovskite solar cell</i> . . . . .	106
5.1	Introduction . . . . .	106
5.2	Materials and Methods . . . . .	108
5.2.1	Synthesis of Ag:Cu Nanocomposite . . . . .	108
5.2.2	Device fabrication . . . . .	108
5.3	Results and Discussion . . . . .	110
5.3.1	J-V Characteristics . . . . .	110
5.3.2	Charge Transport Properties Analysis . . . . .	111
5.3.3	Optical Properties . . . . .	113
5.3.4	Morphology . . . . .	114
5.4	Conclusion . . . . .	117
	<i>References</i> . . . . .	118
6.	<i>Electron transport co-buffer layer for improved charge extraction in polymer solar cell</i> . . . . .	121
6.1	Introduction . . . . .	121

---

6.2	Materials and Methods . . . . .	122
6.2.1	Synthesis of Ag:Cu Nanocomposite . . . . .	122
6.2.2	Device fabrication . . . . .	123
6.3	Results and Discussion . . . . .	124
6.3.1	J-V Characteristics . . . . .	124
6.3.2	Charge Transport Properties Analysis . . . . .	126
6.4	Optical Properties . . . . .	129
6.4.1	UV/Vis Analysis . . . . .	129
6.5	Morphology . . . . .	131
6.5.1	Scanning Electron Microscopy (SEM) . . . . .	131
6.5.2	X-Ray Diffraction (XRD) Study . . . . .	133
	<i>References</i> . . . . .	136
7.	<i>Conclusion</i> . . . . .	139

## 1. GENERAL INTRODUCTION

According to international energy outlook 2017 report[1] the world energy consumption is predicted to rise by 28% between 2015 and 2040 (see Figure 1.1). In order to address global climatic changes, energy security and environmental pollution major transformations are needed in the energy sector. The amount of solar energy released to the outer atmosphere far much exceeds the world energy requirement. In one hour the sun energy (16 TW) of which is equivalent to one year global energy demand. However the available technologies have not been able to exploit and conserve efficiently this energy resource[2, 3]. Renewable energy sources will definitely play significant role in future due to increasing costs and depletion of non-renewable sources as well as environmental pollution. The report further indi-

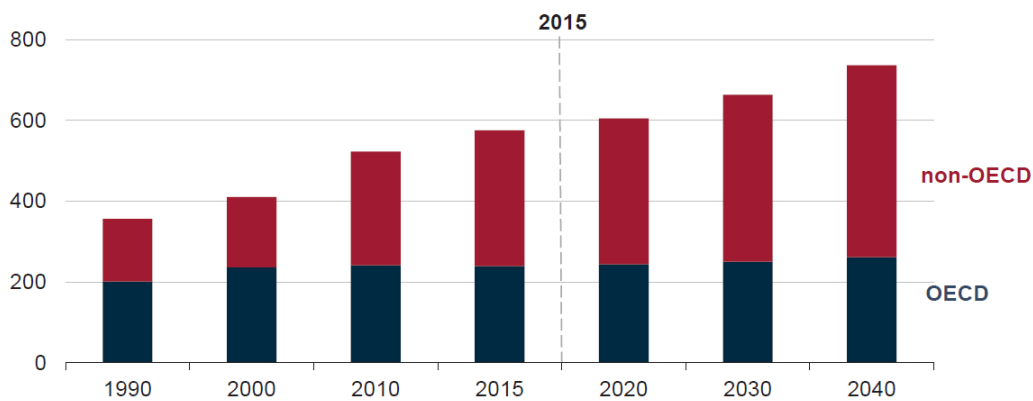


*Fig. 1.1: World energy consumption quadrillion Btu.*

cates that there is direct correlation between variations in global temperatures and the concentration of CO<sub>2</sub> released to the atmosphere. Therefore, it is of paramount importance to control processes that produce CO<sub>2</sub> in order to regulate future global temperature rises(see Figure 1.2). There is need to conserve energy and concurrently find alternative energy sources that are renewable. Most inorganic semiconductor solar cells are well-developed but their high cost prohibit extensive affordability and accessibility. Moreover, their existing solar cell technology is not compatible with solution process and roll to roll production. Photovoltaics technology on the

other hand has witnessed tremendous growth over the past few years and is likely to have the greatest potential to provide this increasing energy demand[3]. The main challenge has always been converting and storing solar energy in an efficient and cost-effective way. Despite Organic photovoltaics based solar cells having progressed in their development within a short period due to optimization of processing conditions, material design, and device architecture and the development of new device architecture but poor reproducibility, low PCE, instability in ambient environment, flexibility and toxic lead and chlorinated solvents remains major hurdles to overcome. Therefore, the future of renewable energy rely heavily on the success of

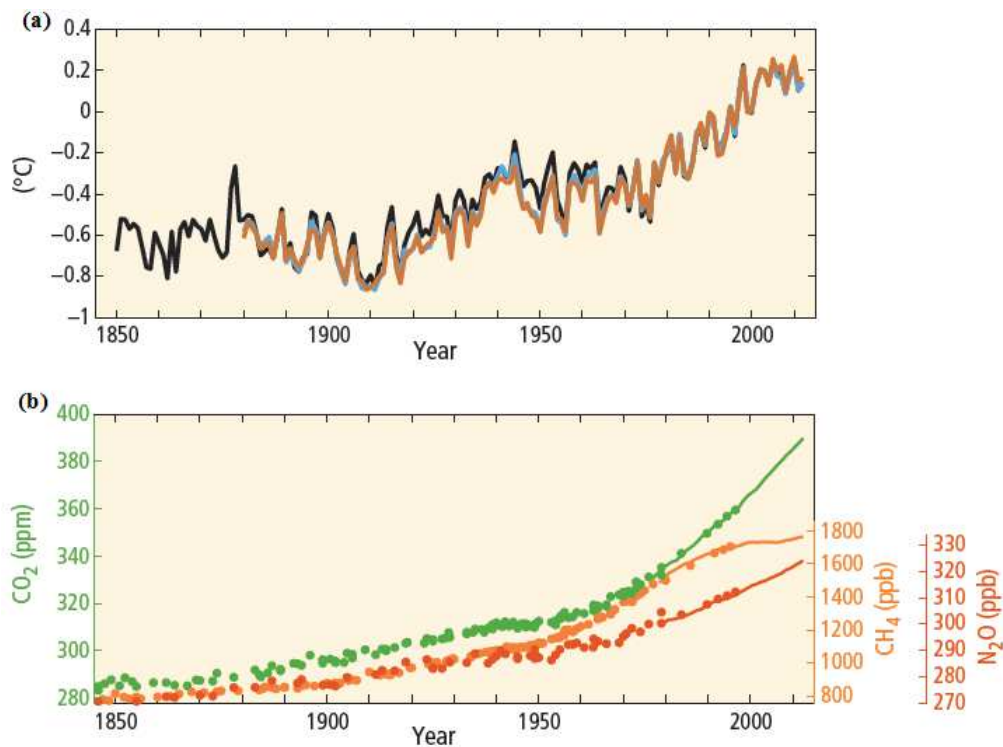


Fig. 1.2: Globally averaged combined land and ocean surface temperature anomaly (a) Globally averaged greenhouse gas concentrations (b)[4].

Organic photovoltaics (OPVs) in providing efficient, stable, environmental friendly and low-cost fabrication methods.

## 1.1 Justification:

Global energy consumption has been continually increasing with industrialization. This has put a strain on fossils fuels, gas and coal which raises the concentration of CO<sub>2</sub> which is not biodegradable in the atmosphere, which cause heavy global

warming, and adverse climatic changes. Therefore, there is urgent need for sources of energy which do not release carbon dioxide and other toxic gases and compounds into the atmosphere.

## 1.2 Aim of thesis

The primary aim of this research is to develop low cost, environmental friendly, solution-processed and reproducible photovoltaic devices with improved efficiency and stability with possibility of upscaling.

## 1.3 Objectives of thesis

- (a) To synthesis metal nanoparticles and employ them in solar cell fabrication.
- (b) Preparation and characterization of metal nanoparticles incorporated thin film solar cells.
- (c) Reduce or find suitable but environmental friendly replacement for toxic lead.

## 1.4 Outline of this thesis

This thesis provides an in-depth investigation on improving optical absorption and enhancing the efficiency of solution processed thin film solar cells particularly perovskite and polymer based solution processed devices. It explores a variety of optimization methods with their performance on thin film perovskite solar cells and provide insights into the physical understanding of their operation mechanism for further improvement.

The thesis comprises of 6 chapters covering the areas of synthesis, characterization and integration of bimetallic nanoparticles in fabrication thin film solar cells with improved device structures through interface engineering and morphology control. Chapter 1 is devoted to general introduction about global energy demand and supply with a critical look at the existing production technologies with a view of addressing environmental pollution. It also highlight the problem addressed by this

research its aims, objectives and justification and concludes with description of the thesis outline.

Chapter 2 gives a general introduction to the OPV field, giving brief discussions of organic solar cells and specifically describes the structure and the principle of operation of organic and polymer based photovoltaic devices highlighting the key issues and challenges experienced. Chapter 3 gives an overview of progress of perovskites based solar cell due to the use of different device architectures, fabrication techniques as well as on the use of various electron and hole transport interfacial layers (HTMs and ETMs). It also discusses the use of solvent additives and the basic mechanisms for device operation which provides better understanding on the properties of the various layers of device structures.

Chapters 4 and 5 reports the results of investigations on the effect of integration of plasmonic bimetallic nanoparticles as interfacial buffer layers into the inverted planar structure perovskite solar cell as ETL and HTL, respectively. Key results of which have been published in articles or already submitted .

Chapters 6 discusses results of investigations on the effect of integration of plasmonic nanoparticles into the active layer of polymer solar cell.

Finally, key conclusions are drawn in chapter 7 and the outlook for future development are discussed.

## References

- [1] Staub, J., International energy outlook. Outlook 2010, 484, 70-99.
- [2] Bauer, G. H., Photovoltaic solar energy conversion. Springer: 2015; Vol. 901.
- [3] Yang, Y.; Li, G., Progress in high-efficient solution process organic photovoltaic devices. Springer: 2016.
- [4] Schmidt Mende, L.; Weickert, J., Organic and hybrid solar cells: an introduction. Walter de Gruyter GmbH & Co KG: 2016.
- [5] Pachauri, R. K.; Allen, M. R.; Barros, V. R.; Broome, J.; Cramer, W.; Christ, R.; Church, J. A.; Clarke, L.; Dahe, Q.; Dasgupta, P., Climate change 2014: synthesis report. Contribution of Working Groups I, II and III to the fifth assessment report of the Intergovernmental Panel on Climate Change. Ipc: 2014.

## 2. LITERATURE REVIEW

### 2.1 General Introduction

The cost of silicon based solar cell production has continued to rise due to their high cost of manufacture and long energy payback time. As a result thin film solar cells based on organic, polymer and hybrid solar cells have gained prominence from their potential to be produced from cheap, non-toxic, earth-abundant raw materials and through solution processing environmentally friendly methods. Thin film solar cells are classified according to the nature of photoactive layer used. Organic solar cells forms part of the third generation solar cells which include dye-sensitized solar cells(DSSCs), and hybrid solar cells[1–3]. The fundamental working principle of organic photovoltaic devices is photoinduced charge separation between donor and acceptor materials. Charge generation begins with absorption of photons in the donor–acceptor blend. The excitons must be able to diffuse and reach the interface between the donor and acceptor materials where charge separation occurs. Therefore it is essential to control the morphology of these devices by keeping the thickness of the p-type and n-type material close to the exciton diffusion length of organic materials (5–20 nm)[4]. The excitons can be dissociated by induced electric field at the heterojunction or by the difference in electrode work functions. The separated charges are then transported to the respective electrodes. Finally electrons are collected by low work function metal which should be well matched with the lowest unoccupied molecular orbital(LUMO) energy level of the acceptor. At the same time holes are collected by a high work function metal which should be well matched with the highest occupied molecular orbital(HOMO) energy level of the donor. The choice of electrodes is crucial to avoid charge recombination as some electrodes like ITO and silver can extract both positive and negative charges from the active layer of the device. However, this is usually minimised through introduction of interfacial buffer layers between the electrodes and the photoactive layer [5].

Figure 2.1 illustrate the main processes in operation of an organic solar cell[6].

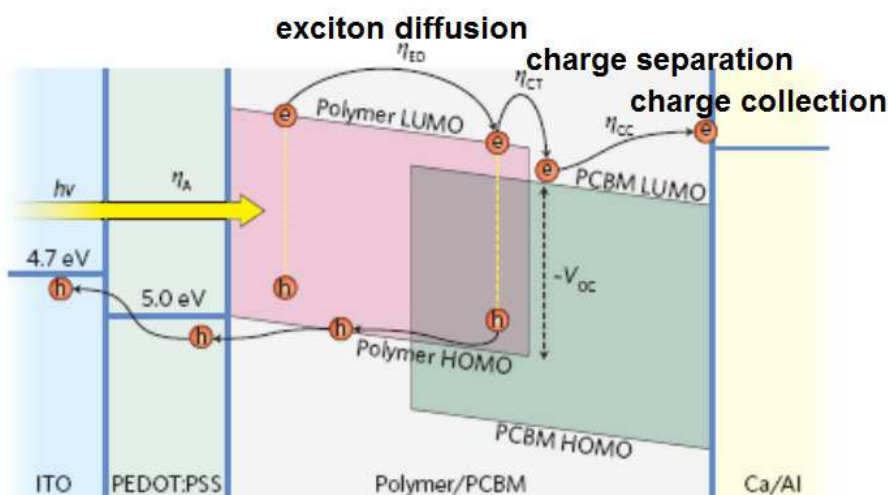


Fig. 2.1: Working principle of an organic solar cell[6].

Efficient exciton creation need broad optical absorption within the solar spectrum and depends on the absorption characteristics of the photoactive materials employed. Exciton diffusion to the interface or electrode is determined by nanoscale configuration of the device with interfaces within the diffusion length of the excitons. Charge separation on the other hand depends on the energy difference between the donor/acceptor (alignment of HOMO and LUMO) which enables charge separation. Finally the dissociated should possess high mobility. The overall PCE is low due to the fact that part of sunlight is reflected and not all photons are absorbed, and some excitons or charges may recombine before they reach the electrodes. The HOMO and LUMO of the donor and acceptor material must be designed in the scale of the exciton diffusion length of organic semiconductors (5–40 nm) in order to convert all the photons absorbed to useful electricity[4].

### 2.1.1 Dye-sensitized solar cells(DSSCs)

DSSCs employs n-type semiconductor of  $\text{TiO}_2$ /dye molecules, i.e. transparent inorganic anode usually nanoporous  $\text{TiO}_2$  sensitized with light-absorbing dye molecules. DSSCs work like photoelectrochemical cells in varied light conditions though it has limited absorption in the near infrared region. The dye upon absorption of light produce excitons, which are dissociated at the dye-semiconductor interface while the transparent semiconductor network provides a pathway for electrons to the

cathode[7]. Figure 2.2 illustrates the structure and working mechanism of Dye-sensitized solar cell.

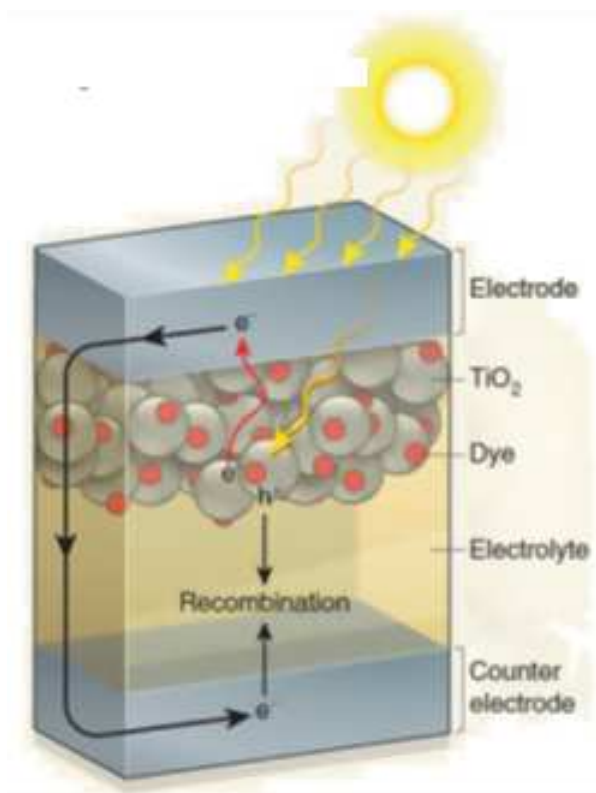


Fig. 2.2: Diagram of a Dye sensitized solar cell [7].

### 2.1.2 Organic solar cells

An organic solar cells contain a blend of of a wide bandgap organic small molecule or polymer donor and a C<sub>60</sub> fullerene derivative acceptor in the photoactive layer. Most fullerene derivatives absorb mainly in the UV, and to a less extend in the visible region of the solar spectrum. In order to obtain high  $J_{sc}$  values, low bandgap donor materials that absorb longer wavelengths of light is required. while high PCEs, needs a perfect alignment of donor /acceptor energy levels to strike an optimum balance between  $V_{oc}$  and  $J_{sc}$  as maximization of one leads to a decrease in the other.

### 2.1.3 Polymer solar cells

Solution-processed polymer solar cells consists of a blend of a p-type semiconducting polymer which acts as an electron donor and an n-type fullerene derivative as

an electron acceptor. Most polymer solar cells have been fabricated from materials such as P3HT and the fullerenes PC<sub>60</sub>BM and PC<sub>70</sub>BM with ITO as back electrode due to its good electrical conductivity with high transparency over a wide range of wavelengths.

Polymer solar cells suffer from short exciton diffusion length, low conductivity and hole mobility which limits the thickness of both the photoactive and charge transport layers to be very small [8].

*Single layered solar cell:* The device structure consist of a single layer of organic material is inserted between two different electrodes. The in-built voltage in single layer solar cells arises from the difference in work function of the electrodes used or from the potential barrier developed between the organic material/electrode interfaces. In each case the photovoltaic performance depends largely on the nature of the electrodes. Single layer solar cell suffer from low fill factor originating from high series resistance of organic material.

*Bilayer Solar Cell:* In a bilayer heterojunction structure the diffusion length of an exciton is restricted to about 10 nm, with the absorption distances is approximately 100 nm which often results in inadequate optical absorption. Bilayer solar cells require the use of two substrates soluble in different solvents to avoid the dissolution of the first substrate during deposition of the second layer. There is inadequate optical absorption in bilayer solar cell devices and only a small portion of the incident photons are converted to charge carriers which lowers the photocurrent in bilayer devices. Any photons absorbed with energy greater than the organic/inorganic semiconductor bandgap is lost as heat. However, bilayer configuration has the advantage of exciton direct single component pathway link between the interface and the electrodes

*Bulk Heterojunction Solar Cells:* Bulk heterojunction architecture was developed in an effort to overcome the limit of device thickness brought about by small exciton diffusion length in organic semiconductors. It involves the blending of both the donor and acceptor in a single layer to form films with high interfacial surface area which not only ensure that excitons are produced close to but also reach the interface before recombination [4]. In bulk heterojunction solar cells (BHJ) two or more single heterojunctions are fabricated directly stacked one on top of one another and connected in series as shown in figure 2.3. This enables optimization of individual

heterojunctions to absorb a specific part of the incident solar spectrum[4]. Optical absorption efficiency can be enhanced by employing two different donors or acceptors with complimentary absorption spectra. The main advantage of BHJ structure is the interpenetrated linkages of components all throughout the photoactive layer which increase the contact area resulting in more effective exciton dissociation.

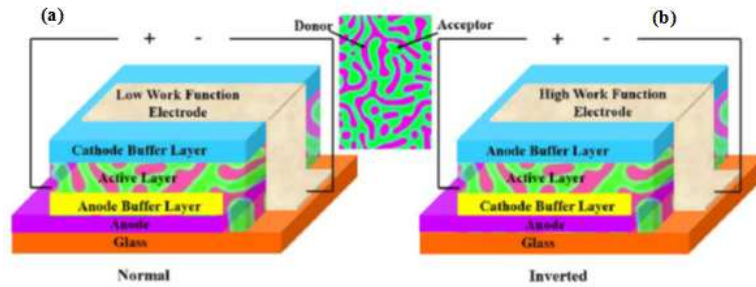


Fig. 2.3: Device architecture of the (a) normal and (b) inverted BHJ OSCs[9]

*Tandem Solar Cells:* Tandem solar cells were developed to minimise energy lost as heat from photons with energy greater than the bandgap of the semiconductor. This is normally brought about by the use of low work function metal electrodes like aluminium which react readily with oxygen or water causing degradation through formation of an insulating metal oxide layer at the interface between the active layer and the anode. The width of the oxide layer eventually increases and may cover the whole device inhibiting electron extraction from the active layer. Tandem solar cells extend optical absorption through the use of both high and low bandgap semiconductors to absorb high-energy photons and low-energy photons respectively. A simplified structure of tandem Solar Cells is provided in figure 2.4.

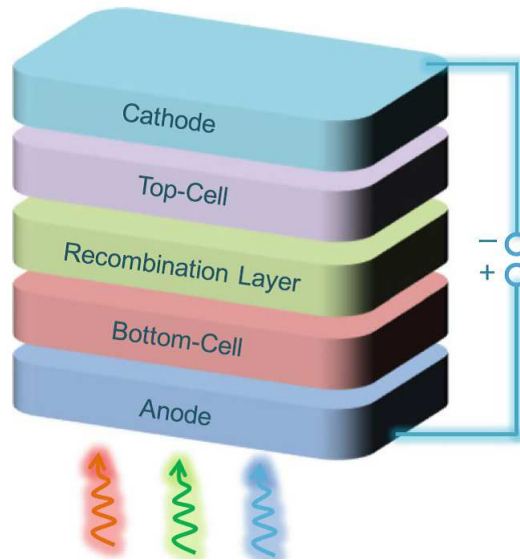


Fig. 2.4: Structure of tandem solar cell[11].

Subcells in tandem solar cells can be connected in series to produce a high  $V_{oc}$  or in parallel to enhance the  $J_{sc}$  through summation of the photocurrent outputs from the individual subcells. The main challenge is mismatch between the subcells which results in recombination of carriers from top and those from the bottom at the interlayers[10]. Optimum thickness of each layer determines the overall efficiency in tandem solar cells.

#### 2.1.4 Hybrid solar cells

Hybrid solar cells forms part of both third and fourth generation solar cells consisting of a mixture of both inorganic and organic nanoparticles [12]. Hybrid solar cells are fabricated from a combination of nanostructured organic materials with inorganic semiconductors to exploit the distinctive features of each component like high electron mobility of inorganic semiconductors and solution processability of organic counterparts[13]. The inorganic component usually forms the charge transport part while the organic semiconducting part forms photoactive layer. Hybrid solar cells possess good optoelectronic properties such as high optical absorption over a wide spectral range, suitable bandgap with appropriate HOMO/LUMO alignment bipolar charge carrier and transport efficiency[14]. The efficiency of hybrid solar cells is still low compared to those fabricated from inorganic materials due to low exciton dissociation coupled with poor charge carrier transport.

### 2.1.5 Perovskite based solar cells

Perovskite solar cell was developed from DSSC. Photovoltaic cells based on perovskites came into limelight and gained prominence in 2009 when Kojima et al. employed hybrid (organic-inorganic) perovskites as photoactive layer [15]. Perovskite is a ambipolar charge transport semiconductor and can be employed as a p-type, n-type or photoactive layer. In addition it has direct tunable band gap, high absorption and extinction coefficients, high carrier mobility and stability[11, 15]. The general chemical structure of organolead halide perovskite follows the formula  $ABX_3$ , where A is the organic molecule ( $CH_3NH_3^+$  or  $NH_2CHNH_2^+$ ), B is a divalent metal (Pb or Sn), and X is a halide (Cl, Br, or I). The bandgap of organometal halide perovskites can be adjusted by tuning their geometry by varying temperature and substituting A, B, and X components of perovskite. If the A site in perovskites is too small a distortion occurs in octahedral phase systems leading to instability and consequently a change in electronic properties. However, when the site B of the perovskite is higher in the periodic table, the bandgap of the organometal halide perovskite is raised[16]. Perovskite solar cell films undergo irreversible degradation at humidity above 55%. Also oxygen, UV light, temperature and solution processing are reported to accelerate degradation. Perovskite based solar cells unlike conventional solar cells exhibit abnormal J-V hysteresis behaviour when scanned from forward bias to reverse bias voltage and vice versa. Its origin is a subject for debate but ferroelectricity has been suggested as the main cause. An in-depth review on perovskite based solar cell is given in chapter 3

## 2.2 Nanomaterials in organic photovoltaics

Over the past few years researchers, scientists and industrialists have engaged themselves in the development of new p-type and n-type photoactive organic semiconductors which are fundamental materials for the advancement of thin film based solar cells. This has also witnessed transition from micro to nanoscale in the design and fabrication of new device structures. Nanomaterials refers to structures of dimensions 100 nm and less. Nanotechnology has been employed to develop new devices and materials with a wide range of applications from consumer based to

electronics products. Most nanostructured materials have physical and chemical properties which are quite different from their bulk counterparts. Nanomaterials combine materials with a variety of different physical and chemical characteristics to produce novel hybrid systems with tunable optoelectronic properties. For example unique optoelectronic properties are exhibited by metals, semiconductors, and insulator on the nanoscale. Their characteristics depend on their physical dimensions, such as shape, size, surface features, doping levels, surrounding medium and presence of other nanostructures. Metal nanoparticles properties can be used to tune the resonant frequency from the UV through to the infra-red part of the spectrum. Nanostructured solar cells include; dye-sensitized solar cells, organic solar cells (and polymer solar cells), perovskite solar cells and quantum dot solar cells. All except DSSCs utilize a thin organic/inorganic molecules of thickness between 50–300 nm as photoactive layer. Nanostructures can contain single component or multiple components. Multiple components nanostructures can be in form of core-shell or metal/polymer nanocomposites. Core-shell nanocomposites form in various shapes and sizes ranging from tubular to spherical[17–20]. Metallic nanoparticles have potential to improve the optical absorption due to the localized surface plasmon resonance (LSPR) effect. It is the collective oscillation of electrons on the nanoparticle surface or at the interface between an insulator and the metal nanoparticle which occurs when the frequency of incident light photons is equal to that of the frequency of surface electrons. This enables the metal nanoparticles to couple with incident light from excitation of their surface plasmon resonances which eventually leads to enhancement of the electromagnetic field at the nanometer scale surrounding the metal nanoparticles[21]. The bimetallic nanoparticle components in semiconductor–metal nanocomposites enhance light-harvesting in semiconductors by improving the charge separation and by increasing the optical absorption. The performance of organic photovoltaic solar cells can be enhanced through extension of the absorption range to longer wavelength by varying the size of the nanoparticles to modify the bandgap. Hybrid photovoltaic solar cells incorporating more than one different semiconductor plasmonic nanostructures have been developed. This has resulted in enhancement of device performance in organic solar cells through improved charge generation and charge transport collection [22]. The main disadvantage of nanomaterials is that resonances takes place at specific wavelengths only and when the nanoparticles are used in the direction of sunlight depending on the

device structure may block part of the incident light[23].

## 2.3 Solar cell Parameters

The important parameter to evaluate the solar cell performance is the electrical power output that can be extracted from the absorbed solar radiation. The J-V characteristic of an illuminated solar cell that works like an ideal diode behaviour of the Shockley solar cell is given by;

$$J = J_s \left( \exp\left(\frac{q(V - JAR_s)}{nk_B T}\right) \right) + \frac{V - JAR_s}{AR_{sh}} - J_{ph} \quad (2.1)$$

where  $J_{ph}$  is photo-generated current,  $J_s$  is reverse supersaturation current,  $n$  is ideality factor;  $R_s$  and  $R_{sh}$  are series and shunt resistances, respectively. Equation (2.1) reduces to a simple diode equation which is often used for the characterization of a single diode solar cell

$$J = J_s \left( \exp\left(\frac{q(V - JAR_s)}{nk_B T}\right) \right) - J_{ph} \quad (2.2)$$

The first term describes thermally generated currents and current injection from the electrodes while the second term stands for photo-generated current. All the solar cell parameters can be derived from the current-voltage equations. The maximum power given by the rectangle shown in Figure 2.5 is the maximum output power of the device and the power conversion efficiency is given by:

$$\eta = \frac{P_{out}}{P_{in}} = \frac{FF \times V_{oc} J_{sc}}{P_{in}} \quad (2.3)$$

The overall photovoltaic performance of a solar cell is determined by short-circuit current density ( $J_{sc}$ ), open-circuit voltage ( $V_{oc}$ ) and fill factor (FF). The short circuit current density, is the photocurrent generated at the contacts without externally applied field while the highest potential developed by the device is the open-circuit voltage. The quality of the device which is given by the squareness of the current density voltage curve is the fill factor (FF)(see figure 2.5).

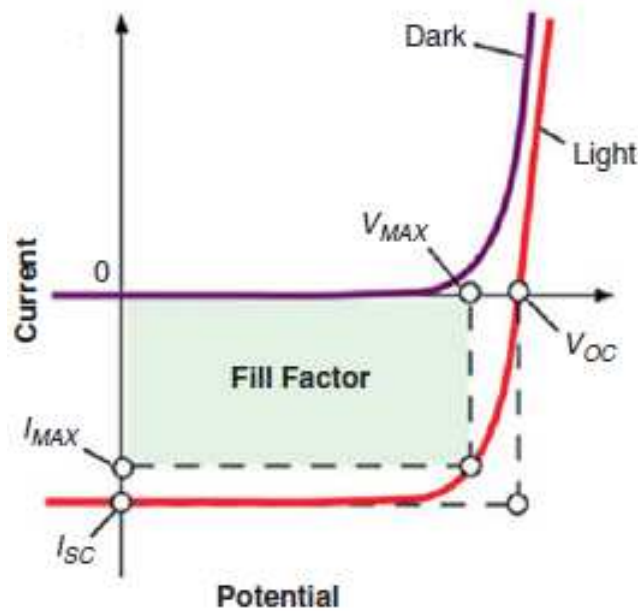


Fig. 2.5: Current–voltage characteristics of an OPV cell in the dark and under illumination.[24]

It is the ratio of maximum power produced to the product of  $J_{sc}$  and  $V_{oc}$ . Both the  $J_{sc}$  and  $V_{oc}$  depends on the bandgap of the photoactive material and only photons with energies higher than the bandgap are absorbed to generate excitons. The  $V_{oc}$  on the other hand is determined by the energy difference between HOMO of the donor and LUMO of acceptor. A narrow bandgap is needed to maximize optical absorption and a high energy difference between HOMO and LUMO to obtain a high  $V_{oc}$ [25, 26]. Current density is also affected by charge mobility; a high charge mobility leads to higher current densities. Maximizing thickness gives more excitons however, minimizing thickness leads to higher photocurrents. The thickness of the photoactive layer must be smaller than the exciton diffusion length to avoid bulk recombination. As a result, the thin-film organic solar cell has poor photon absorption and harvesting[5, 27].The fill factor will also affect both the  $J_{sc}$  and  $V_{oc}$  which in turn are directly related to internal series and parallel resistance in a device. FF depends on a number of factors such as, the nanoscale structure of the photoactive layer such as; (hole mobility of the photoactive layer, crystallinity, the quality of the interfaces between the photoactive material and the electrodes), charge extraction layer, materials design, morphology control, and interfacial engineering. The success of organic photovoltaic solar cells for commercialization will be determined by improvement in efficiency, stability, lifetime, and a reduction in production costs. Although the PCE has been gradually improving, temperature, humidity, oxygen,

moisture, U-V light and solution processing are the main causes of degradation in organic and perovskite solar cells. Stability and lifetime must be guaranteed before upscaling and commercialization.

## References

- [1] Guo, X.; Zhou, N.; Lou, S. J.; Smith, J.; Tice, D. B.; Hennek, J. W.; Ortiz, R. P.; Navarrete, J. T. L.; Li, S.; Strzalka, J., Polymer solar cells with enhanced fill factors. *Nature Photonics* 2013, 7 (10), 825.
- [2] Hoppe, H.; Sariciftci, N. S., Organic solar cells: An overview. *Journal of Materials Research* 2004, 19 (07), 1924-1945.
- [3] Kumavat, P. P.; Sonar, P.; Dalal, D. S., An overview on basics of organic and dye sensitized solar cells, their mechanism and recent improvements. *Renewable and Sustainable Energy Reviews* 2017, 78, 1262-1287.
- [4] Hatton, R. A., Organic Photovoltaics. In *A Comprehensive Guide to Solar Energy Systems*, Elsevier: 2018; pp 255-277.
- [5] Janssen, R. A.; Hummelen, J. C.; Sariciftci, N. S., Polymer–fullerene bulk hetero-junction solar cells. *MRS bulletin* 2005, 30 (1), 33-36.
- [6] Sha, W.; Choy, W.; Chew, W. In *Plasmonic Effects in Organic Solar Cells*, Progress in Electromagnetics Research Symposium, Electromagnetics Academy. The Journal's web site is located at <http://www.piers.org/piersproceedings/>: 2012.
- [7] Tiwari, S.; Tiwari, T.; Carter, S. A.; Scott, J. C.; Yakhmi, J., Advances in Polymer-Based Photovoltaic Cells: Review of Pioneering Materials, Design, and Device Physics. In *Handbook of Ecomaterials*, Springer: 2018; pp 1-48.
- [8] Brabec, C.; Scherf, U.; Dyakonov, V., *Organic Photovoltaics: Materials, Device Physics, and Manufacturing Technologies*. John Wiley & Sons: 2014.
- [9] Rafique, S.; Abdullah, S. M.; Sulaiman, K.; Iwamoto, M., Fundamentals of bulk heterojunction organic solar cells: An overview of stability/degradation issues and strategies for improvement. *Renewable and Sustainable Energy Reviews* 2018, 84, 43-53.

- [10] Choy, W. C., Organic solar cells: materials and device physics. Springer: 2012.
- [11] Wu, B.; Mathews, N.; Sum, T.-C., Plasmonic Organic Solar Cells: Charge Generation and Recombination. Springer: 2016.
- [12] Fara, L., Advanced solar cell materials, technology, modeling, and simulation. IGI Global: 2012.
- [13] Huang, H.; Huang, J., Organic and Hybrid Solar Cells. Springer: 2014.
- [14] Malik, M. A.; Skabara, P., Nanostructured Materials for Type III Photovoltaics. Royal Society of Chemistry: 2017; Vol. 45.
- [15] Al-Dainy, G. A.; Bourdo, S. E.; Saini, V.; Berry, B. C.; Biris, A. S., Hybrid perovskite photovoltaic devices: properties, architecture, and fabrication methods. Energy Technology 2017, 5 (3), 373-401.
- [16] Banerjee, D.; Chattopadhyay, K. K., Hybrid Inorganic Organic Perovskites: A Low-Cost-Efficient Optoelectronic Material. In Perovskite Photovoltaics, Elsevier: 2018; pp 123-162.
- [17] Zhong, Z. J., Optical properties and spectroscopy of nanomaterials. World Scientific: 2009.
- [18] Gupta, R. K.; Misra, M., Metal Semiconductor Core-shell Nanostructures for Energy and Environmental Applications. Elsevier: 2017.
- [19] Pareek, V.; Bhargava, A.; Gupta, R.; Jain, N.; Panwar, J., Synthesis and applications of noble metal nanoparticles: a review. Advanced Science, Engineering and Medicine 2017, 9 (7), 527-544.
- [20] Frohlich, E., Nanoparticles in Biology and Medicine: Methods and Protocols. Edited by Mikhail Soloviev. ChemMedChem 2013, 8 (1), 167-167.
- [21] Lim, E. L.; Yap, C. C.; Teridi, M. A. M.; Teh, C. H.; bin Mohd Yusoff, A. R.; Jumali, M. H. H., A review of recent plasmonic nanoparticles incorporated P3HT: PCBM organic thin film solar cells. Organic Electronics 2016, 36, 12-28.
- [22] Lee, J. M.; Kim, S. O., Enhancing organic solar cells with plasmonic nanomaterials. ChemNanoMat 2016, 2 (1), 19-27.

- 
- [23] Huang, Q.; Hu, X.; Fu, Z.; Lu, Y., Plasmonic Thin Film Solar Cells. In *Nanos-structured Solar Cells*, InTech: 2017.
- [24] Chiechi, R. C.; Havenith, R. W.; Hummelen, J. C.; Koster, L. J. A.; Loi, M. A., Modern plastic solar cells: materials, mechanisms and modeling. *Materials Today* 2013, 16 (7), 281-289.
- [25] Guo, X.; Zhou, N.; Lou, S. J.; Smith, J.; Tice, D. B.; Hennek, J. W.; Ortiz, R. P.; Navarrete, J. T. L.; Li, S.; Strzalka, J., Polymer solar cells with enhanced fill factors. *Nature Photonics* 2013, 7 (10), 825.
- [26] Brabec, C. J.; Cravino, A.; Meissner, D.; Sariciftci, N. S.; Fromherz, T.; Rispen, M. T.; Sanchez, L.; Hummelen, J. C., Origin of the open circuit voltage of plastic solar cells. *Advanced Functional Materials* 2001, 11 (5), 374-380.
- [27] Mayer, A. C.; Scully, S. R.; Hardin, B. E.; Rowell, M. W.; McGehee, M. D., Polymer-based solar cells. *Materials today* 2007, 10 (11), 28-33.

### 3. PEROVSKITES PHOTOVOLTAIC SOLAR CELLS: OVERVIEW OF CURRENT STATUS

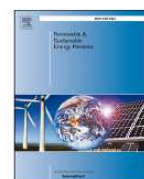
Renewable and Sustainable Energy Reviews 91 (2018) 1025–1044



Contents lists available at ScienceDirect

Renewable and Sustainable Energy Reviews

journal homepage: [www.elsevier.com/locate/rser](http://www.elsevier.com/locate/rser)



#### Perovskites photovoltaic solar cells: An overview of current status

Patrick Tonui<sup>a</sup>, Saheed O. Oseni<sup>a</sup>, Gaurav Sharma<sup>b,d</sup>, Qingfenq Yan<sup>c</sup>, Genene Tessema Mola<sup>a,\*</sup>



<sup>a</sup> School of Chemistry & Physics, University of KwaZulu-Natal, Pietermaritzburg Campus, Private Bag X01, Scottsville 3209, South Africa

<sup>b</sup> School of Chemistry, Shoolini University, Solan 173229, Himachal Pradesh, India

<sup>c</sup> Department of Chemistry, Tsinghua University, Beijing 100084, China

<sup>d</sup> College of Materials Science and Engineering, Shenzhen Key Laboratory of Polymer Science and Technology, Nanshan District, Shenzhen University, Shenzhen 518060, PR China

#### ARTICLE INFO

##### Keywords:

Perovskite solar cell  
Hole and electron buffer layers  
Thin film  
Solvent additives  
Optical properties

#### ABSTRACT

Perovskite based solar cells have recently emerged as one of the possible solutions in the photovoltaic industry for availing cheap solution processable solar cells. Hybrid perovskites display special combination of low bulk-trap densities, ambipolar charge transport properties, good broadband absorption properties and long charge carrier diffusion lengths, which make them suitable for photovoltaic applications. The year 2015 witnessed an upsurge in the published research articles on perovskite solar cells (PSC) which is indicative of the potential of this material. Since the introduction of PSC the power conversion efficiency has reached above 22% in a relatively short period of time. However, the poor reproducibility in device fabrication and lack of uniformity of the PSCs performances is a major challenge in obtaining highly efficient large scale PSC devices. The aim of this paper is to present a brief review on the current status of perovskites based solar cell due to the use of different device architectures, fabrication techniques as well as on the use of various electron and hole interfacial layers (HTMs and ETMs). The review also discusses the basic mechanisms for device operation which provides better understanding on the properties of the various layers of device structures.

## 3.1 Introduction

One of the most important challenges facing our society today is searching for clean and renewable energy sources in order to mitigate the rapidly increasing energy demand due to population growth and industrialization [1–10]. The overreliance on fossil fuels such as oil, coal and gas have caused enormous challenges on the Earth's atmosphere due to the green house effect that resulted in continuous rise of atmospheric temperature which in turn caused the recurrence of drought, flooding,

severe winter in different parts of the globe. It is imperative to search for alternative sources of renewable energy to save ourselves from increasingly dangerous path of using fossil fuel. A lot of efforts have been invested to harness solar energy to ease the problem. In fact, a number of alternative photovoltaic technologies are available at present to harvest solar energy into useful electricity. The major challenges in the photovoltaic technologies have always been converting and storing solar energy in an efficient, cost-effective and environmentally friendly manner. For over six decades the number of photovoltaic technologies have evolved in the search for efficient and low cost solar cells. There are four phases of photovoltaic technological evolution known today; the first generation of solar cells are fabricated based on crystalline silicon which have dominated the photovoltaic (PV) market for the past half a century. However, the processing cost of crystalline silicon based solar cells is relatively high, making it unaffordable for many around the globe. Besides, the residuals from processing the silicon wafer is also environmentally unfriendly. The second generation of photovoltaic technology uses thin film inorganic compounds including a-Si:H, CdTe, and CIGS technology which have often required vacuum vapour deposition in the preparation of thin film that consumes high energy. Third generation of PV technologies are solution processable thin film solar cells which are designed to generate high power conversion efficiency at low device fabrication cost; these include light condensed cells, organic photovoltaic cell (OPV), dye-sensitized solar cells (DSSCs) [2, 3]. Last but not least, perovskite based solar cells recently emerged as fourth generation of photovoltaic technology which exceeded expectations in terms of producing high power conversion efficiency in very short period of time (see Fig. 3.1 and Fig. 3.2 (a))[3–6].

Despite lots of research on perovskite based solar cells (PSCs), a very small fraction of the total research in the PSC have reported power conversion efficiency greater than 22% [8–12]. This is partly due to the instability of the perovskite medium and problems associated with the reproducibility of the devices. The structural imperfections and limited range of light absorption of the perovskite photoactive layer are some of the factors that determine the power conversion efficiency in PSC. However, the instability of the perovskite in ambient environment is a major challenge to the realization of upscaling and commercialization. A number of research efforts are still in progress to address the issue of stability by way of interface engineering and new device architectures. As of November 03, 2017, a simple search on the

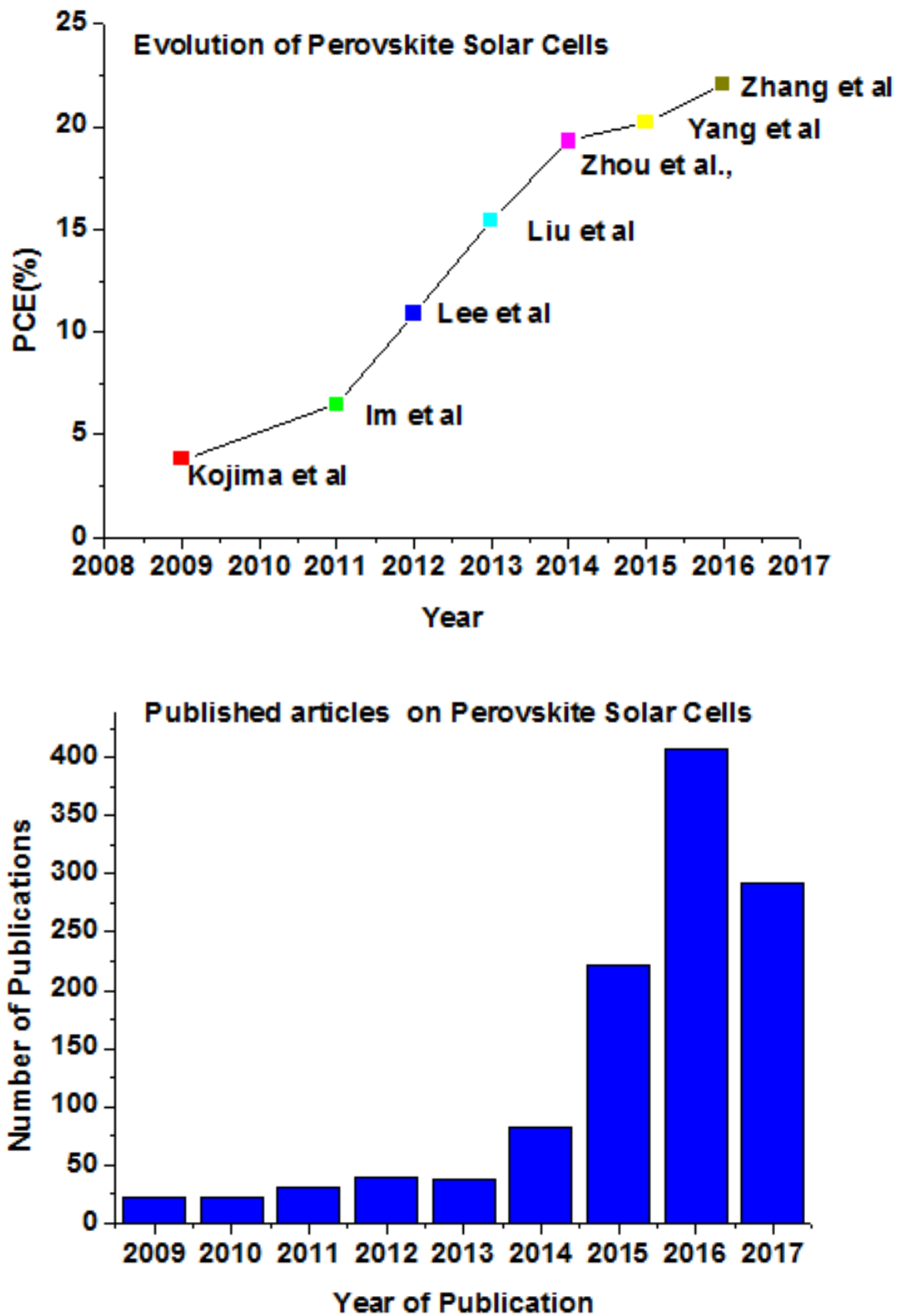


Fig. 3.1: Steady growth of power conversion efficiency of perovskite based solar cell

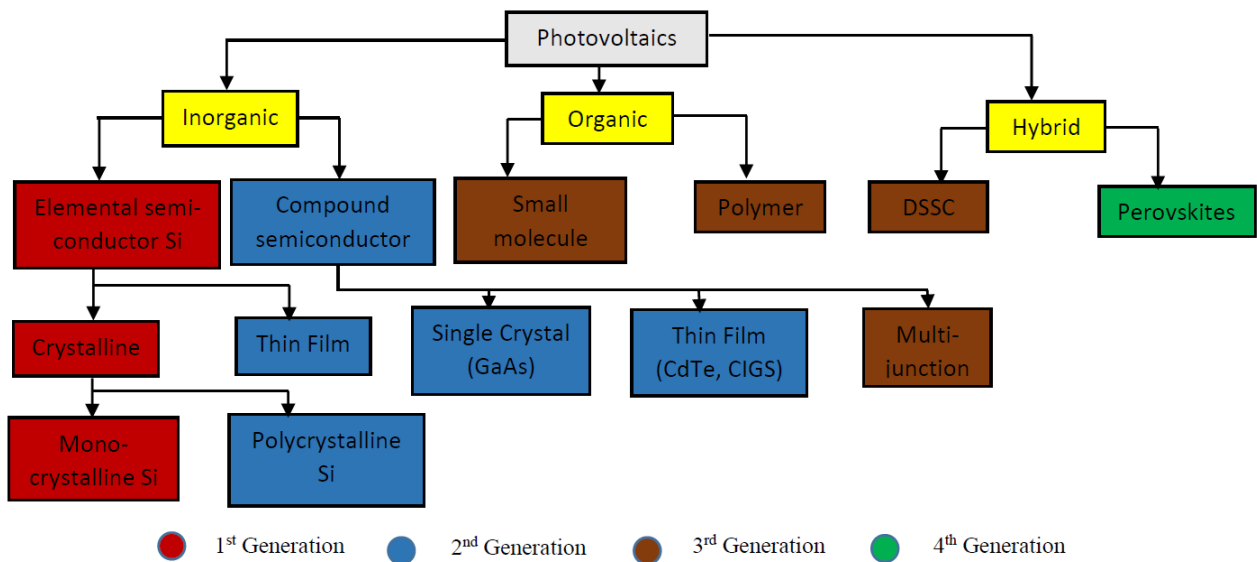


Fig. 3.2: Evolution of photovoltaic solar cells[7]

Science direct using as key words "Fabrication and Characterization of perovskite solar cells" gives 1606 papers which is an indication of the high emphasis given to the research field (see Fig 2 (b)). The first sections of this review discusses the evolution and working principles of perovskite based solar cells. This is then followed by discussion on topics such as; film preparation and characterization methods, nature of various types of perovskites, device architectures, Lead-free Perovskite, charge transport materials (both organic and inorganic) and effect of solvent additives and conclusions. The purpose of this review work is to provide a detailed account of the broad range of issues in the processing of perovskite based solar cells instead of focusing on selected topics. This is however by no means claimed as exhaustive but differs from other reviews as it covers a range of topics, recent development and addresses a relatively new area of interest such as crystalline perovskite.

### 3.1.1 Perovskite based solar cells evolution

Some authors dated back to the early 1990 laid the foundation for the beginning of concerted efforts in the investigations of perovskite as solar absorber. Green et. al. have recently published an article on the series of events that lead to the current state of solid perovskite solar cell [13]. The year 2006 regarded by many as a landmark towards achieving perovskite based solar cell when 2.2% power conversion efficiency was reported from dye-sensitized solar cell using MAPbBr<sub>3</sub> as sensitizer by a researcher Japan [8]. The first perovskite-sensitized TiO<sub>2</sub> solar cell were fabricated

using liquid electrolytes based on iodide or bromide solutions. Kojima et al reported, in 2009, the first organic lead halide compounds  $\text{CH}_3\text{NH}_3\text{PbBr}_3$  and  $\text{CH}_3\text{NH}_3\text{PbI}_3$  as sensitizers in photoelectrochemical cells. They measured an improved PCE of 3.81% for the  $\text{CH}_3\text{NH}_3\text{PbBr}_3$ -based device and 3.13 % for the  $\text{CH}_3\text{NH}_3\text{PbI}_3$ -based device, respectively [15]. In 2011, the same group reported a PCE of 6.5% still using the  $\text{CH}_3\text{NH}_3\text{PbI}_3$ -based iodide liquid electrolyte contact, but with improved preparation conditions. However, the perovskite nanocrystals decomposed in the iodide liquid electrolyte which lead to rapid device degradation which lasted only for about 10 minutes [16]. The need for solid contact was necessary to improve device stability of the device because the adverse effect that polar iodine has on the perovskite structure emanating from iodine liquid electrolyte. By mid-2012, a solid state DSSCs was fabricated with exceptionally high PCE of 9.7% using spiroOMeTAD as a HTM and perovskite solar absorber ( $\text{CH}_3\text{NH}_3\text{PbI}_3$ ). The use of a solid-state HTM dramatically improved the devices stability compared to liquid electrolyte, however, the stability issue still remains the main challenge for mass production and commercialization of perovskite solar cell[17, 18]. On the other hand the power conversion efficiency of PSCs was growing to a new level which was reported in 2013 using sequential deposition method for the formation of the perovskite pigment within the porous metal oxide film that resulted in improved film morphology and power conversion efficiency as high as 15 % [19, 20]. In March 2013, Sang II Seok and his coworkers reported in Nano Letters promising results from using mixed halide perovskite solar cell through optimization of ratio of halides in  $\text{CH}_3\text{NH}_3\text{Pb}(\text{I}_{1-x}\text{Br}_x)_3$  compound [20]. This paved the way for unprecedented growth in PCE over the years, with a highly efficient solid-state solar cells produced with PCE of 12.3 % [21], 15% in 2013, 19.3 % at first half of 2014 [22]. A PCE of 20.1 % was reported by Korean Research Institute of Chemical Technology (KRICT), by W. S. Yang and co-workers using Formamidinium lead iodide ( $\text{FAPbI}_3$ ) as active layer which was later certified by National Renewable Energy Laboratory (NREL) in late 2014 [5, 13, 23]. Another break through was reported in early 2016 jointly by (KRICT)/ Ulsan National Institute of Science and Technology (UNIST) with PCE 22.1% [25]. Methods of device preparations and the PSCs performances achieved by various research groups through varying material optimization approaches, device architectural design, interfacial engineering and improved fabrication conditions have been duly reported and highlighted in able 1, 2 and 4. [8–14, 19, 24–60].

### 3.1.2 Working of perovskite solar cells

The processes of charge generation to collection in perovskite solar cell are not well understood because of the complex nature of the medium. The principles of p-n junction used to describe silicon based solar cells are still applicable to characterize the properties of perovskite solar cells. A number of authors treated perovskite solar cells as p-n, p-i-n and n-i-p junctions solar cell. However, there are still a lot of ambiguity on how to translate the operating mechanisms of PSC in terms of already existing knowledge because of the various layers of materials involved in PSC fabrication. Several studies on the charge transport dynamics in PSC suggest that the electron-hole pairs are generated immediately after photoexcitations in perovskite medium and then dissociated into free charge carriers in less than 2 ps [6, 61, 62] by the built-in electric field caused by the work function difference between the anode and the cathode. The success of perovskite as a good solar absorber is largely dependent on the long charge diffusion length and high carrier mobilities in the medium. The electron and hole diffusion length in perovskite medium can reach as high as 1  $\mu\text{m}$  which is large enough for the photo-generated charges to reach the interfacial layers and electrodes without geminate and non-geminate recombination depending on the morphology of the perovskite medium[62]. The carrier mobilities

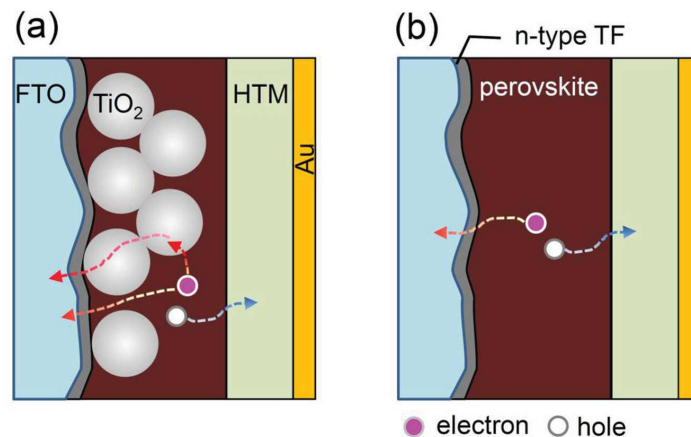


Fig. 3.3: Charge transport channels in perovskite solar cells (a) using mesoporous medium (b) planar perovskite structure [5].

are reported to be as high as  $25 \text{ cm}^2/(\text{V}\cdot\text{s})$ [12, 61] which is three order of magnitude greater than the mobilities in bulk-heterojunction organic solar cells. The two main device architectures known today in the preparation of perovskite solar cell are mesoporous-PSC and planar-PSC structures. Hence, the charge transport chan-

nels in PSC are often discussed in terms of the nature of these two device structures. In mesoporous structure, the perovskite layers are formed on porous semiconductor metal-oxide ( $\text{TiO}_2$ ) medium which create inter-penetrating network between the two phases, and therefore, the photo-generated electrons can be transported along the titanium oxide domain to the cathode while the holes are transported along the perovskite domain to the anode (see Fig. 3.3).

In the case of planar structure, the devices are fabricated using interfacial buffer layers of hole and electron transport material (ETM and HTM) through which the photo-generated charges created in the photo-active medium can be driven to the electrodes by the influence of either built in potential or external applied field. In both cases, the power conversion efficiency of the devices is strongly dependent on the the quality of the morphology of the perovskite film. Bad morphology of the solar absorber film will result in charge accumulation in the medium which enhances charge recombination that significantly reduces the performance of the devices. Moreover, the formation of Ohmic contact between the active and ETM/HTM layers is a critical factor for the successful collection of charges from the devices. It is generally to be noted that the effective conversion of solar energy heavily relies on the optical absorption of a photoactive medium of a solar cell which ideally needs to overlap with visible and near infrared regions of the solar spectrum because of the high intense emission of the radiation in the region. If the band gap of a solar absorber is too small  $< 1$  eV, the device will be able to collect extra current from infrared emission but the open-circuit voltage will be too small. If the band gap is too wide ( $> 2$  eV), only a small fraction of solar radiation can be harvested. Hence, a semiconductor with a band gap of approximately 1.2 - 1.6 eV is ideal material for solar cells fabrication in the form of single junction. Hybrid perovskite films are direct band gap semiconductors with low bulk trap densities which have demonstrated significant luminous properties. The band gap of the hybrid perovskites can be tuned by molecular engineering, i.e. by tuning the composition of the compounds.

### 3.1.3 Solar cell characterization

The capacity of a solar cell to convert solar energy into useful electricity mainly depends on the nature of the photoactive medium and the effectiveness of the device architecture to collect photo-generated current. According to Shockley and

Queisser (SQ) calculations the upper limit for solar energy conversion efficiency using single-junction solar cell is close to 33% at 1.4 eV absorber energy band gap. However, many of single-junction solar cells have recorded efficiencies well below this upper limit because of the various factors involving in the functions of real solar cells which includes defects, unavoidable impurities, interfacial potential barriers etc [6, 7, 63–65]. The maximum limit of power conversion efficiency decreases as the absorber band gap shifts away to from the ideal energy band gap 1.4 eV. Fig. 3.4 shows the dependence of the maximum power conversion efficiency limit for various energy band gap absorber materials and experimentally recorded efficiencies. The

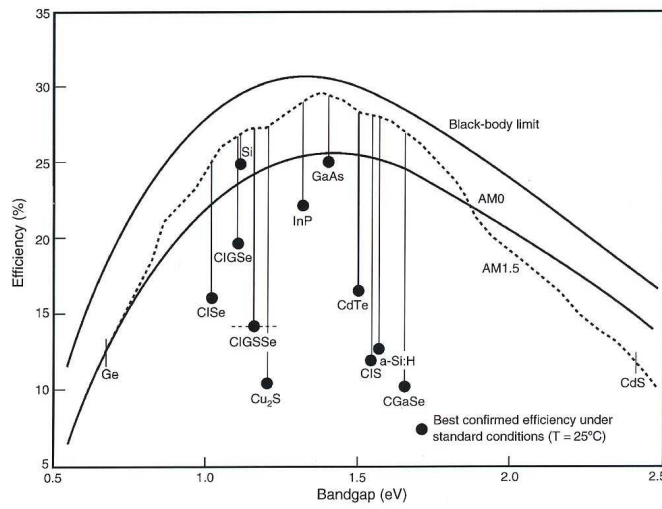


Fig. 3.4: Dependence of the maximum efficiency limit on energy band gap of the solar absorber [63].

SQ limits were calculated by assuming all losses are avoided and all photons with energy  $E > E_g$  are absorbed, all non-radiative recombination pathways are eliminated and the device radiates like a black body with chemical potential  $\mu > 0$ . It is also assumed that each absorbed photon leads to the creation of one electron in external circuit and hence the internal quantum efficiency (IQE) is unity. Shockley and Queisser regards the solar cell as a body, emitting blackbody radiation,  $\phi_{bb}$ , and absorbing solar radiation  $\phi_{sun}$ . Both absorbed and emitted photon flux only depend on the absorbance,  $a(E)$ , which determines the short circuit current density [66].

$$J_{SC}(SQ) = q \int_0^{\infty} a(E) \phi_{sun} dE \quad (3.1)$$

where  $E$  is the photon energy,  $q$  is the elementary charge,  $a(E) = 1$  (for  $E > E_G$ ) and  $a(E) = 0$  (for  $E < E_G$ ) gives efficiency limits as;

$$J_{SC}(SQ) = q \int_{E_g}^{\infty} a(E) \phi_{sun} dE \quad (3.2)$$

The ratio of the generated Frenkel excitons to the total incident photons, in terms of energy, is defined as the absorption efficiency ( $\eta_A$ ). The absorption efficiency is expressed as;

$$\eta_A = \frac{J_{sc}^A}{J_{sc}^{max}} \quad (3.3)$$

$J_{sc}^{max}$  is the maximum current density that could be extracted from a device, due to its dependence on wavelength,

$$J_{sc}^{max} = \frac{q}{hc} \int_{\lambda_1}^{\lambda_2} P_{AM1.5G}(\lambda) \lambda d\lambda \quad (3.4)$$

where,  $P_{AM1.5G}$  is the AM1.5G solar irradiance,  $h$  is Planck's constant and  $c$  the speed of light in vacuum.  $J_{sc}^A$  is the current density that the device would generate at short circuit, assuming that all the photons absorbed within the active layer contribute to the photocurrent hence,

$$J_{sc}^A = \frac{q}{hc} \int_{\lambda_1}^{\lambda_2} A^{act} P_{AM1.5G}(\lambda) \lambda d\lambda \quad (3.5)$$

where  $A^{act}$  is the active layer absorption.

In real solar cells, however, part of the collected solar energy is dissipated in a number of channels from the device. The main mechanisms of energy losses are due to the presence of various forms of resistances against the flow of charges. A solar cell is therefore modelled by equivalent circuit which takes into consideration the resistances in real devices (see Fig. 3.5). The series resistance arises from the bulk properties of the active layer, electrodes as well as the contact resistances between the active layer and electrodes. The shunt resistance originated mainly from carrier

recombinations and leakage current from the edge of the device. The necessary information in the characterization of a solar cell are contained in the current-voltage plots from the devices. For a single-junction type solar cell as depicted in Fig. 5 can be described by the current-voltage relationship expressed as:

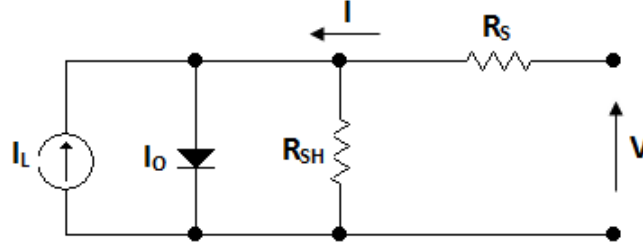


Fig. 3.5: Equivalent electrical circuit for single-junction solar cell.

$$J = J_s \left( \exp\left(\frac{q(V - JAR_s)}{nk_B T}\right) \right) + \frac{V - JAR_s}{AR_{sh}} - J_{ph} \quad (3.6)$$

where  $J_{ph}$  is photo-generated current,  $J_s$  is reverse supersaturation current,  $n$  is ideality factor;  $R_s$  and  $R_{sh}$  are series and shunt resistances, respectively. For the solar cells with minimal leakage current (i.e.  $R_{sh} \ll R_s$ ) the current equation reduces to a simple diode equation which is often used for the characterization of a single diode solar cell.

$$J = J_s \left( \exp\left(\frac{q(V - JAR_s)}{nk_B T}\right) \right) - J_{ph} \quad (3.7)$$

The first term describes thermally generated currents and current injection from the electrodes while the second term stands for photo-generated current. All the solar cell parameters can be derived from the current-voltage equations (7)[67–69]. The open circuit voltage of a solar cell is often defined as:

$$V_{OC} = \frac{nk_B T}{q} \ln\left(\frac{J_{ph}}{J_0} + 1\right) \quad (3.8)$$

where  $n$  is the ideality factor which determines the quality of the devices. When  $n = 1$ , the carrier recombination in the depletion region is negligible and diffusion current is prevailing in the device. On the other hand, when  $n = 2$  the recombination process in the device is high. In reality, the device exhibits both recombination

current and diffusion current, hence, the value of  $n$  normally varies between 1 and 2. The diode quality becomes poor when  $n > 2$ .

### 3.2 Methods of perovskite film Preparation

The two major mechanisms in the preparation of perovskite films are vacuum deposition and solution processing. Solution processing methods has preferential advantage over vacuum deposition because of the low-cost and compatibility with roll-to-roll device production. In both cases, researchers used various steps or procedures in the preparation of the films that resulted in difference in the quality of the film as well as in the reported power conversion efficiencies. The most common procedures in vacuum deposition are one-step precursor deposition, sequential vapour deposition, dual source vacuum deposition processes. While in the solution processing approach, one-step spin-coating, two-step spin-coating, vapour-assisted solution processing and spray-coating are some of the most common deposition methods (see Fig. 3.6)[32, 70, 71]. A brief account of each of the deposition method will be discussed in the following subsection.

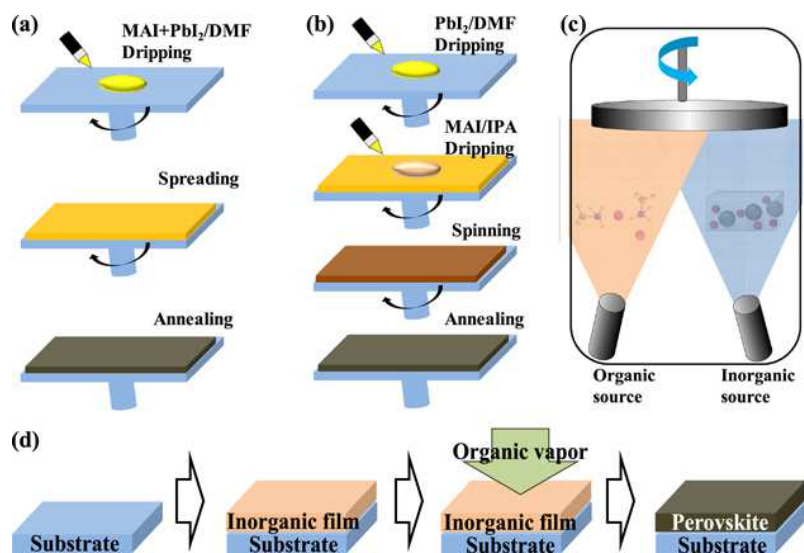


Fig. 3.6: Various types of perovskite film preparation (a) One-step precursor deposition, (b) two-step sequential deposition method, (c) DSVD and (d) VASP [72]

- **One step spin-coating deposition:** It is solution based method which involves the precipitation from solution where the precursor metal halide and organic halide molecules are dissolved to produce perovskite crystals. In one-step spin-

coating, a precursor solution is prepared by mixing  $\text{CH}_3\text{NH}_3\text{I}$  (MAI) (or  $\text{CH}_3\text{NH}_3\text{Cl}$  (MACl) and  $\text{PbI}_2$  in polar aprotic solvents such as N, N-dimethylformamide (DMF), dimethylsulfoxide (DMSO) or gamma-butyrolactone (GBL). The precursor solution is then spin-coated on the substrates followed by annealing the samples at  $90^\circ\text{C}$  (see Fig. 6 (a)) which produces perovskite crystals [72, 73]. It is, however, difficult to control film properties such as film uniformity and morphology using this methods[74]. Therefore, perovskite crystals prepared by a single-step spin-coating method is characterized by the formation of larger grain sizes, rough and uncontrollable film morphologies which may suppress the charge carrier extraction processes that leads to poor device PCE.

- **Two step spin-coating deposition:** In the two-step process, first a metal halide ( $\text{PbI}_2$ ) is spin coated on the the substrate followed by coating of  $\text{CH}_3\text{NH}_3\text{I}$  (MAI) from a solution on dried  $\text{PbI}_2$  film. The colour of the film turns from yellowish to dark brown. Then the film is annealed at  $90^\circ$  for 10 minutes to improve the film morphology. In some cases, the second step can be replaced by dipping the  $\text{PbI}_2$  film into the organic salt solution which produces perovskite formed by a chemical reaction. The two-step solution process was developed in order to gain better control over the film morphology of  $\text{CH}_3\text{NH}_3\text{PbI}_3$  deposition. This approach involve diffusion of the  $\text{CH}_3\text{NH}_3^+$  cations into the lead-halide matrix to form perovskite film. However, the challenge with this method is the formation of a compact  $\text{MAPbI}_3$  film on the top layer of  $\text{PbI}_2$  which prevent further formation of perovskite deep into  $\text{PbI}_2$  layer. Therefore, larger thickness and sufficient time would be required to fully convert the  $\text{PbI}_2$  into perovskite [75].

- **Vapour-assisted solution process (VASP):** This procedure involves the deposition of  $\text{PbI}_2$  film from a solution first (via spin coating) followed by anealling the film in a chamber filled with  $\text{CH}_3\text{NH}_3\text{I}$  vapour at  $150^\circ$  for two hours. Devices based on VASP have outstanding short-circuit current densities and show no sign of current leakage through the absorber film. It has exhibited improved grain sizes of the perovskite films which help reduce the presence of grain-boundary, traps and reduce charge-carrier scattering that lead to lower charge recombination and enhanced device performance. Some of the most important advantages of vapour assisted solution processed perovskite solar cells is the high reproducibility of high-quality

Tab. 3.1: Optimal device performance reported with different perovskite deposition methods[71].

VASP = Vapour assisted solution process; SVD = Sequential vapour deposition; DSVD = Dual source vacuum deposition; SCD = Spray coating deposition

Deposition process	$J_{SC}$ (mA cm <sup>-2</sup> )	$V_{OC}$ (v)	FF	PCE%	Ref
Two-step Spin coating	23.69	1.113	77.3	20.4	12
direct intra-molecular exchange	24.7	1.06	77.5	20.2	60
One step deposition	23.83	1.086	76.2	19.71	10
sequential solution deposition	22.75	1.13	75.01	19.3	11
sequential solution deposition	22.19	1.01	72	16.1	8
Two-step Spin coating	21.5	1.02	71	15.9	59
Two-step Spin coating	21	1.02	71	15.8	47
sequential solution deposition	20.4	1.03	75	15.7	58
sequential solution deposition	20.3	1.02	76.6	15.7	29
sequential solution deposition	21.9	1.04	73	15.6	31

films, including high purity, compatibility with large areas and fine control over film thickness and morphology as well as high PCE. A PCE of over 10.6 % has been achieved using VASP method[76].

- **Vacuum deposition methods:** Vacuum deposition method allows the depositions of precursors in vacuum atmosphere. It is possible to use this method to deposit one precursor at a time (single step) or two or more precursors deposition simultaneously (co-deposition). The advantage of this method is that the deposition takes place in a clean environment and reduce contamination from solvents. It allows control over the film thickness and offers better film uniformity. In addition, the low fabrication temperature makes vacuum deposition compatible with a wide range of substrates, including flexible substrates and textiles. One of the advantages of dual-source vapour deposition is the possibility of preparing highly crystalline perovskite films of arbitrary thickness and the ability to monitor material growth in real-time. It is noteworthy, however, annealing perovskite layer in air has proven to be an efficient method for the formation of high quality perovskite film compared to annealing in nitrogen atmosphere.

Table 3.1 compares the performance of the solar cells produced by various film deposition techniques. According to the device performance summarized in table 3.1 the sequential solution deposition involving two-step Spin coating have produced the highest PCE as reported in the literatures. Generally, two-step film deposition is the most successful and reliable solution processing methods with better reproducibility of the devices compared to one step. According to Hariz et al[81] vapour deposition creates better uniformity in the deposition of perovskite film compared

to solution processing method. The films produced by spin coating are less uniform and form pin holes which causes leakage currents that reduces device performance. Fig. 3.7 shows significant difference in the performance of devices fabricated by vapour deposition compared to solution processed films. Enhanced photocurrent and open circuit voltage is recorded using vapour deposition. This is due to the fact that, in addition to the uniformity of the films in vapour deposition, it is solvents free and hence contains less impurities than the film produced by solution processing. However, in terms of device production cost and large scale roll-to-roll compatibility, solution based sequential deposition is preferable [51].

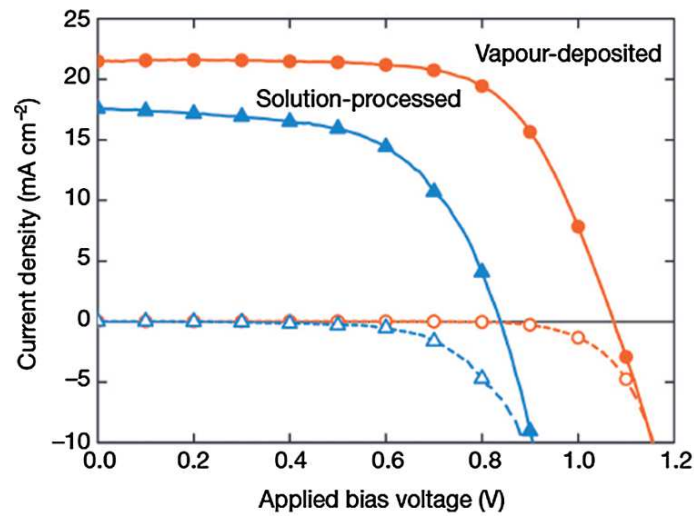


Fig. 3.7: Current-voltage characteristics of perovskite solar cell produced by vapour deposition and solution processing. The device performance of dual vapour deposition was found to be 15.5 % while 8.6 % was recorded for solution processing[51].

### 3.3 Organometal halide perovskites

#### 3.3.1 Composition and properties of perovskites

The general chemical structure of organolead halide perovskite follows the formula  $ABX_3$ , where A is the organic molecule ( $CH_3NH_3^+$  or  $NH_2CHNH_2^+$ ), B is a divalent metal (Pb or Sn), and X is a halide (Cl, Br, or I) [82]. The two most commonly used organic molecules in the formation of organic-inorganic hybrid halide perovskites are Methylammonium (MA) and Formamidinium (FA). Fig. 3.8 shows the chemical

structures of these basic and important organic molecules in a perovskite. Of these two compounds, methylammonium is the most commonly used organic component of the perovskite structure. However, FA has favourable energy band gap close to

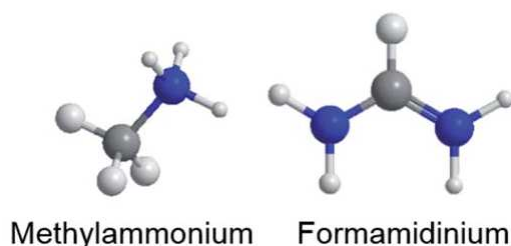


Fig. 3.8: Chemical structure of (a) Methyl ammonium and (b) Formamidinium [83].

1.47 eV and broader absorption band compared to methylammonium cation. It is also known to have a slightly larger ionic radius than the methylammonium group, which leads to an increase in perovskite tolerance factor. The difference of these molecules is evident when they both form perovskite with lead tri-iodide molecule. The Formamidinium lead iodide (FAPbI<sub>3</sub>) perovskites has better optical absorption width compared to conventional methylammonium lead iodide (MAPbI<sub>3</sub>). This is due to the lower energy band-gap of FAPbI<sub>3</sub> has close to 1.47 eV compared to 1.57 eV of MAPbI<sub>3</sub>. The main advantages FAPbI<sub>3</sub> over MAPbI<sub>3</sub> and MAPbBr<sub>3</sub> is that it forms uniform and continuous thin film with less concentrations of pinholes or defects. FAPbI<sub>3</sub> is also more stable as it does not undergo a structural phase transition within the operation temperature-range of the solar cell.

Organometallic lead halide perovskite was first introduced as a sensitizers in dye-sensitized solar cells (DSSCs) in 2006, and further development was achieved by using CH<sub>3</sub>NH<sub>3</sub>PbI<sub>3</sub> as a sensitizer in 2009 [84]. These perovskite materials have outstanding properties such as high absorption coefficient and broad absorption band covering almost the entire visible spectrum from 300 to 800 nm. Mixed halide perovskite such as CH<sub>3</sub>NH<sub>3</sub>PbX<sub>x</sub>I<sub>3-x</sub> (X = Br, Cl) exhibited slight blue-shift while NH<sub>2</sub>CHNH<sub>2</sub>PbI<sub>3</sub> exhibited red-shift. Significant red shift of optical absorption was reported from CH<sub>3</sub>NH<sub>3</sub>SnI<sub>3</sub> or CH<sub>3</sub>NH<sub>3</sub>Sn<sub>x</sub>Pb<sub>1-x</sub>I<sub>3</sub> well beyond 1000 nm. Organo lead halide perovskite possesses ambipolar charge-transport properties with high electron and hole mobility as high as (2-10)cm<sup>2</sup> V<sup>-1</sup> s<sup>-1</sup> and (5-12) cm<sup>2</sup> V<sup>-1</sup> s<sup>-1</sup>, respectively (for CH<sub>3</sub>NH<sub>3</sub>PbI<sub>3</sub>). The medium offers relatively balanced

electron and hole transport with long diffusion lengths in the range of micrometre for  $\text{CH}_3\text{NH}_3\text{PbI}_3$  and  $\text{CH}_3\text{NH}_3\text{PbCl}_x\text{I}_{3-x}$ . The most widely investigated organolead halide perovskites are  $\text{CH}_3\text{NH}_3\text{PbI}_3$  and  $\text{CH}_3\text{NH}_3\text{PbI}_{3-x}\text{Cl}_x$  because of their long carrier diffusion length in the order of 100 nm and over  $1\ \mu\text{m}$ , respectively. They have high carrier mobility of about  $66\ \text{cm}^2/\text{V}\cdot\text{s}$  which significantly reduces carriers recombination.

### 3.3.2 Methylammonium lead triiodide ( $\text{CH}_3\text{NH}_3\text{PbI}_3$ )

Methylammonium lead iodide perovskite ( $\text{CH}_3\text{NH}_3\text{PbI}_3$ ) forms cubic structure as depicted in Fig. 3.9 has interesting optical and electrical properties which are suitable to be used as a solar absorber. It has become one of the leading compound for the preparation of organic-inorganic hybrid perovskite solar cells. It has high optical absorption coefficient, good electrical transport properties, favourable band gap ( $\sim 1.55\ \text{eV}$ ), which is close to the optimum value for a single junction solar cell. Moreover, the long-range electron-hole diffusion lengths of at least in the range of

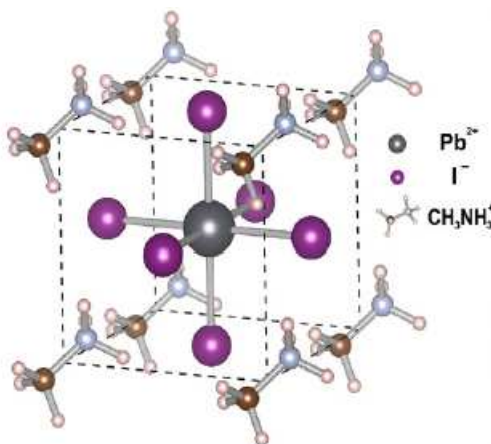


Fig. 3.9: General crystal structure of  $\text{CH}_3\text{NH}_3\text{PbX}_3$  perovskite[85].

100 nm is responsible for the success of  $\text{MAPbI}_3$  perovskite in the fabrication of mesostructured solar cells using solution processing. The challenges have been the formation of uniform, pinhole-free  $\text{CH}_3\text{NH}_3\text{PbI}_3$  films on planar substrate by conventional solution process discussed in section II as well as short life time of the perovskite film under exposure to humidity and elevated temperatures.

3.3.3 Methylammonium lead tribromide ( $\text{CH}_3\text{NH}_3\text{PbBr}_3$ )

Bromide is one of the halide group that can substitute the role of iodine in the formation perovskite. Methylammonium lead tribromide possesses high energy bandgap (2.3 eV) compared to iodine based perovskite but offers unique properties as a solar absorber. Although  $\text{MAPbBr}_3$  has less optical absorption in the infrared region where the emission intensity is high but it offers higher  $V_{OC}$  compared to triiodide counterparts( see Fig. 3.10).

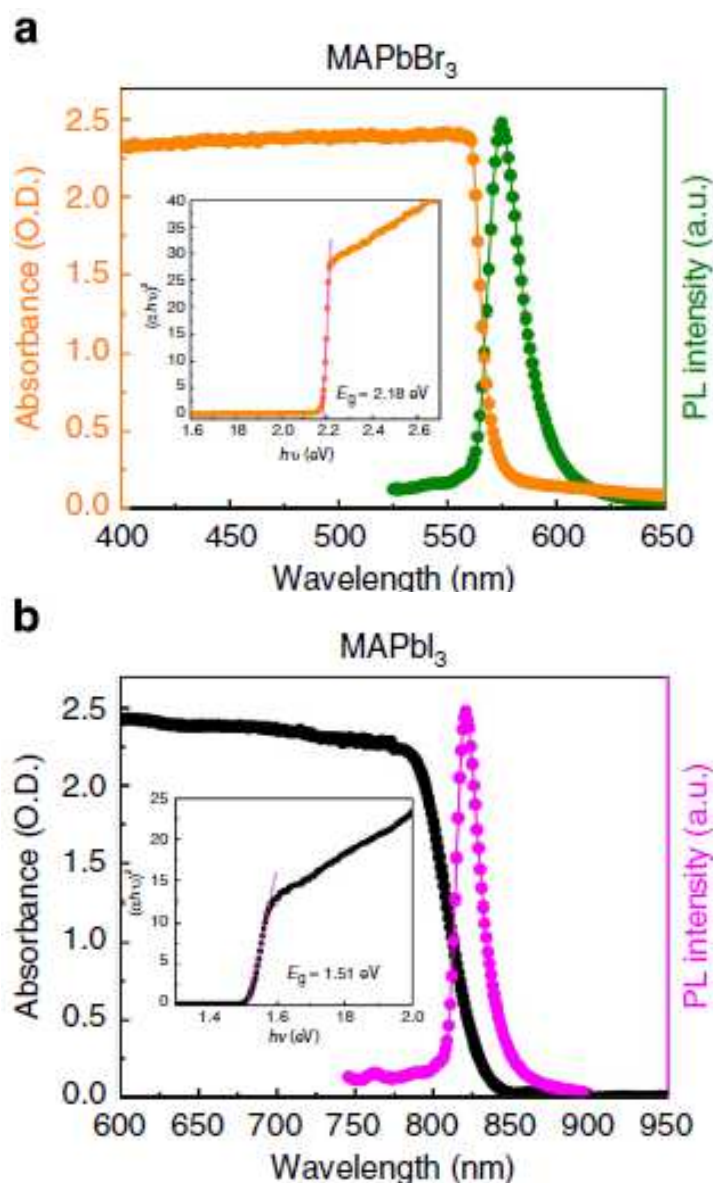


Fig. 3.10: Steady-state absorption and photoluminescence. (a)  $\text{MAPbBr}_3$  single crystal. (b)  $\text{MAPbI}_3$  single crystal. Insets: corresponding Tauc plots displaying the extrapolated optical band gaps[84].

Cai et al. and Noh et al.,[20] using conjugated polymers PCBTDP or PTAA respectively as the HTM, in a  $\text{CH}_3\text{NH}_3\text{PbBr}_3$  based perovskite solar cell, obtained solar cells with high  $V_{OC}$  of 1.16 V while Edri and co-workers reported later a  $V_{OC}$  up to 1.3V[91]. Bromide based perovskite forms good quality film solar absorber as confirmed by Sheng et al.,[6] who reported through XRD measurements that there is no remnants of  $\text{CH}_3\text{NH}_3\text{Br}$  and  $\text{PbBr}_2$  in the synthesized  $\text{CH}_3\text{NH}_3\text{PbBr}_3$  which is indicating that all of the  $\text{PbBr}_2$  is converted into  $\text{CH}_3\text{NH}_3\text{PbBr}_3$  and the  $\text{CH}_3\text{NH}_3$  has been completely used up [84].

### 3.3.4 Mixed halide perovskite $\text{CH}_3\text{NH}_3\text{PbI}_{3-x}\text{Cl}_x$

The properties of halide perovskite can be fine tuned by introducing additional halide element in the basic structure. This leads to changes in the energy band gap as well as the optical absorption band width as shown in Fig. 3.11. The mixed halide perovskite consists of  $\text{CH}_3\text{NH}_3\text{PbI}_{3-x}\text{Cl}_x$  and  $\text{CH}_3\text{NH}_3\text{PbI}_{3-x}\text{Br}_x$ . However, both  $\text{MAPbI}_3$  and  $\text{CH}_3\text{NH}_3\text{PbI}_{3-x}\text{Cl}_x$  are direct band gap semiconductors with high absorption coefficient and a favourable band gap of 1.5-1.65 eV as well as a high electron-hole diffusion length ranging from  $\sim 100\text{nm}$  to  $\sim 1\mu\text{m}$ . In 2012, Snaith and co-workers used the mixed-halide  $\text{CH}_3\text{NH}_3\text{PbI}_{3-x}\text{Cl}_x$ , which exhibited better stability and carrier transport compared to its pure iodide equivalent. The carrier diffusion length improved by about ten times greater than that of the pure iodide ( $\sim 100\text{nm}$ ) resulting in good carrier collection[62].  $\text{MAPbI}_{3-x}\text{Cl}_x$  has been found to have a long charge diffusion length and improved stability in air compared to  $\text{MAPbI}_3$  [86]. The electron-hole diffusion length is greater than 1 micron for  $\text{CH}_3\text{NH}_3\text{PbI}_{3-x}\text{Cl}_x$ , whereas in the case of  $\text{CH}_3\text{NH}_3\text{PbI}_3$ , it is only 100 nm [87]. Li et al reported that  $\text{MAPbI}_{3-x}\text{Cl}_x$  and  $\text{MAPbI}_3$  having similar absorption and photoluminescence decay-lifetimes, bandgaps and Fermi levels. Though devices with a  $\text{MAPbI}_{3-x}\text{Cl}_x$  photoactive layer generally result in higher efficiency PSCs [88]. The  $\text{CH}_3\text{NH}_3\text{PbI}_{3-x}\text{Cl}_x$  has been reported to be used in fabricating efficient planar devices by evaporation. It is to be noted that the properties of mixed halides depends on the stoichiometric ratio of the halide in the medium (see Fig 11). In general, mixing halides in perovskites increases stability, enhances carrier transport and bandgap tuning [89].

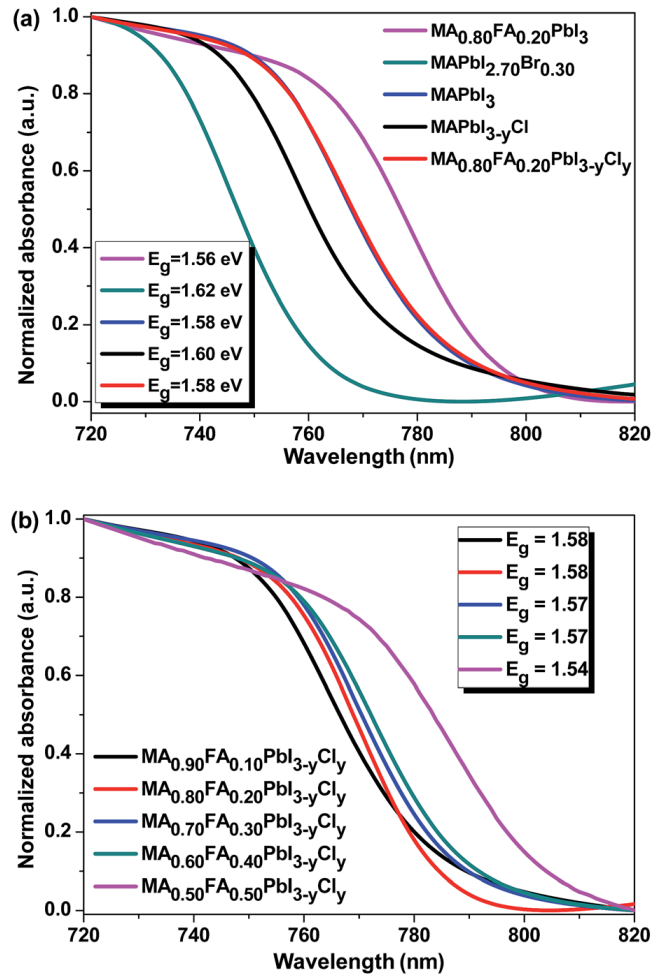


Fig. 3.11: The effect of stoichiometric ratio of halides in the synthesis of organic lead perovskite.

The onset of absorption changes by the amount both organic and inorganic component of the compounds [90, 91].

### 3.3.5 Crystalline perovskite

In addition to polycrystalline perovskite solar cells, which have been under intense investigation since 2006, a single crystal perovskite solar cell has recently attracted a lot of research attention. Due to the low trap density and absence of grain boundaries of single crystals, they possess much better optoelectrical properties than their polycrystalline counterpart. In 2016, Bakr's group first reported perovskite monocrystalline solar cells with two different device structures: ITO/MAPbBr<sub>3</sub> (4 μm)/Au and FTO/TiO<sub>2</sub>/MAPbBr<sub>3</sub> (1 μm)/Au [92]. The first HTM-free PSC resulted a power conversion efficiency > 5%. By utilizing a p-n junction in the second PSC, the efficiency was enhanced to 6.5%, which was higher than that of the best HTM-free PSCs. At the same time, Dong et al. fabricated PSCs with millimeter sized bulk single crystal. The device was with a lateral structure and the PCE was up to 5.36 %

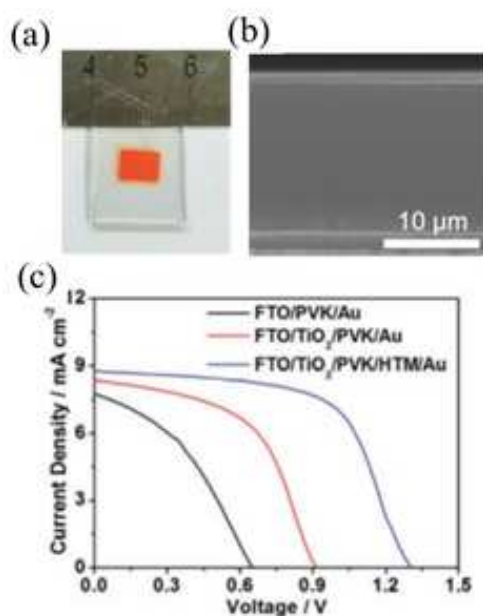


Fig. 3.12: (a) The photograph of MAPbBr<sub>3</sub> single crystal film (b) cross sectional SEM of solar cell structure (c) the J-V curves of cells [95].

via piezoelectric poling [93]. Chen et al. developed a solvent engineering strategy to adjust the orientation of polycrystalline film [94]. By preparing amorphous PbBr<sub>2</sub> precursor and adding non-polar CYHEX to the solvent, crystal orientation could be significantly adjusted to the [001] direction with an even surface. The PCE of the HTM-free PSC was up to 8.09 % (V<sub>oc</sub> = 1.35 V), which was the highest in MAPbBr<sub>3</sub>-based HTM-free PSCs. Recently, perovskite single crystal films have been fabricated by a space-limited crystallization method. The thicknesses of the as-grown single crystal film could be adjusted from nanometers to several tens of micrometers, with lateral dimension ranging from hundreds of microns to millimeters [96–98]. Based on such a technology, Rao et al. prepared a laminar MAPbBr<sub>3</sub> single crystal solar cell. The MAPbBr<sub>3</sub> single crystal film had a thickness of 16 μm and a size of 6 × 8 mm<sup>2</sup>, as shown in Fig. 12. The PCE of single crystal PSC achieved a remarkable growth 7.11 %. Furthermore, the PCE preserved 93 % of its initial value after aging for 1000 h, showing a high stability [95].

### 3.4 Phase transitions in perovskites

Perovskite is the result of the reaction between metal and organo halide molecules with the general formula given by:



Where A represents a protonated amino group like MA<sup>+</sup> or FA, B stands for Pb<sup>2+</sup> or Sn<sup>2+</sup> and X stands for halide such as I<sup>-</sup>, Br<sup>-</sup>, or Cl<sup>-</sup>. The reaction kinetics of perovskite phase formation are really fast. Moreover, it has been reported that perovskite phase undergoes structural transition depending on the temperature of the environment. Generally, in a temperature range between 300 K and 400 K, CH<sub>3</sub>NH<sub>3</sub>PbX<sub>3</sub> undergoes reversible phase transition between tetragonal and cubic symmetry which is in the range of solar cell operating temperatures. The phase transition is in fact confirmed by XRD measurements as depicted in Fig 3.13(b). Such structural transitions in the perovskite film could affect the photovoltaic properties as structural phase transition is usually accompanied by changes in band structure [90, 99, 100]. The cubic phase is transformed into the tetragonal phase at temperature close to 300 K, this is often attributed to the ordering iodine ions which results in lower symmetry of tetragonal from the cubic system. The larger unit cell volume of the cubic structure is favourable for the transition than that of the tetragonal structure. This is due to both thermal expansion of the unit cell and atomic disordering of I and Pb atoms in the cubic phase.

Tab. 3.2: Crystal systems and transition temperatures (K) of CH<sub>3</sub>NH<sub>3</sub>PbX<sub>3</sub> (X = Cl, Br, or I).

Material	CH <sub>3</sub> NH <sub>3</sub> PbCl <sub>3</sub>	CH <sub>3</sub> NH <sub>3</sub> PbBr <sub>3</sub>	CH <sub>3</sub> NH <sub>3</sub> PbI <sub>3</sub>
Crystal system	cubic	cubic	cubic
Transition temp.	177	236	330
Crystal system	Tetragonal	Tetragonal	Tetragonal
Transition temp.	172	149 ≈ 154	161
Crystal system	Orthorhombic	Orthorhombic	Orthorhombic

According to the information provided in Fig. 3.13(a) and table 3.2 at very low temperature below 200 K, the tetragonal perovskite phase is transformed into the orthorhombic systems because of the ordering of CH<sub>3</sub>NH<sub>3</sub> ions in the unit cell [100]. The XRD study results, by Oku et al, found that phase transformation of the CH<sub>3</sub>NH<sub>3</sub>PbI<sub>3</sub> perovskite structure from tetragonal to cubic system is due to partial separation of PbI<sub>2</sub> from CH<sub>3</sub>NH<sub>3</sub>PbI<sub>3</sub> phase which is attributed to the decrease

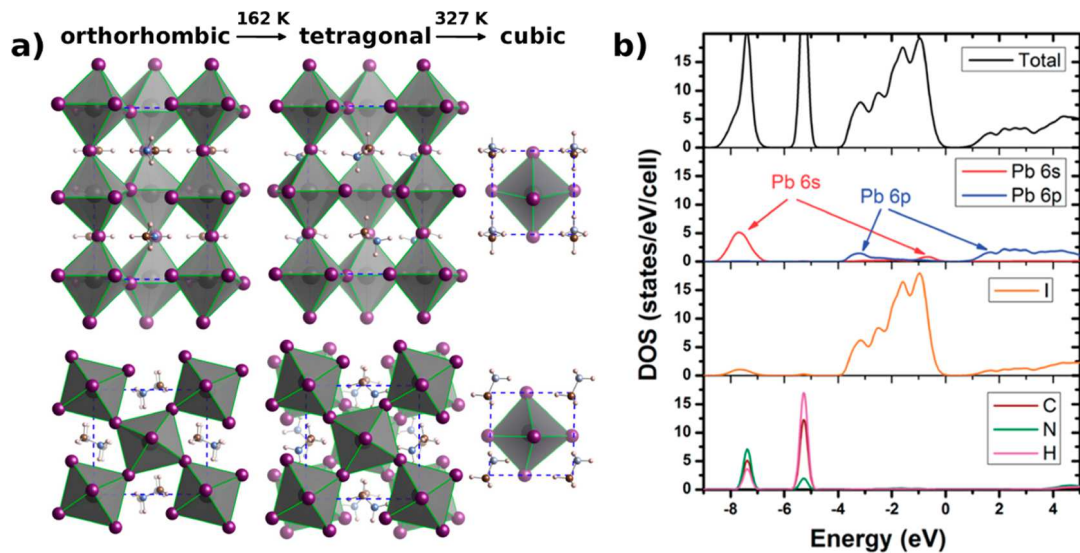


Fig. 3.13: Structure models of (a) during the phase transition from cubic, tetragonal and orthorhombic structures (b) the XRD results of the various phases of the perovskite film [90].

of the unit cell volume of the cubic perovskite [101, 102]. Reports indicate that no change in the photovoltaic parameters have been observed in a transition from tetragonal to cubic structure. However, Significant loss in PCE is observed in the transition from tetragonal to orthorhombic structures.

### 3.5 Perovskite solar cell architectures

Perovskite solar cell comprises of basically the perovskite photoactive film sandwiched between two electrodes. Interfacial buffer layers are often employed between the active layer and the electrodes to facilitate the charge transport processes (see Fig. 3.14). There are two types of interfacial layers in the device structures namely electron transport materials (ETM) and hole transport materials (HTM) which are either organic or inorganic materials. In principle, one of the electrodes must be a transparent conducting oxide (TCO) such as indium or fluorine-doped tin oxide (ITO or FTO), in some cases, aluminium doped zinc oxide (AZO) is also used. The device structure culminated by deposition of metal(top)electrode from either aluminium, silver or gold [14, 103]. Nonetheless, in terms of charge collection strategy from PSC there are two distinct structures namely, the conventional (n-i-p) and inverted (p-i-n) structures (see Fig. 3.14), where p, n and i are p-type, n-type and in-

trinsic layers of materials. The main difference between n-i-p and p-i-n architectures is the currents flows in the opposite directions [104, 105]. Furthermore, depend-

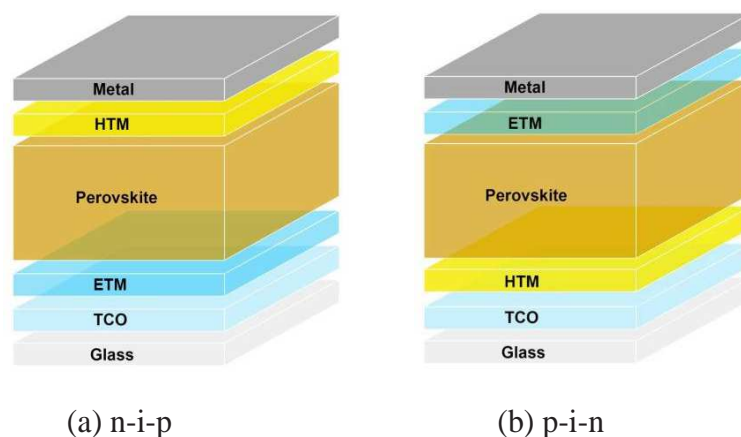


Fig. 3.14: The device structure of PSC (a) Conventional (b) inverted structures [70, 106–108].

ing on whether the device contains mesoporous medium or not the perovskite solar cell can be classified as mesoporous and planar structure. Mesoporous uses n-i-p type design because of the need for the deposition of porous TCO electrode. Metal oxides such as  $\text{TiO}_2$ ,  $\text{Al}_2\text{O}_3$  or  $\text{ZrO}_2$  are the most common materials for the preparation of mesoporous medium in PSC. The purpose of these mesoporous media in PSC are not only to serve as a scaffold compact thin films but also as selective charge transport(blocking)materials. For example  $\text{TiO}_2$  scaffolds extends well into the optical path of the photoactive layer which assist in the effective collection of electrons from the medium by preventing or reducing charge recombination. However,  $\text{TiO}_2$  as cathode buffer layer in the n-i-p structure requires high temperature sintering at  $(450\text{-}500)^\circ\text{C}$  and hence the solar cells suffer from anomalous current-voltage (I-V) hysteresis. Nonetheless, Perovskite solar cell with mesostructured  $\text{TiO}_2$  or  $\text{Al}_2\text{O}_3$  scaffold have typically shown higher efficiency and stability on glass substrates upon annealing at high temperatures [109–113]. Planar perovskite solar cells commonly uses p-i-n design with  $\text{C}_{60}$  and its derivatives (e.g.,  $\text{PC}_{61}\text{BM}$ ,  $\text{PC}_{71}\text{BM}$ , ICBA) as organic electron transporting materials (ETMs). Planar PSC employs both HTM and ETM in its structure which significantly enhances the collection of photogenerated holes and electrons. As a consequence p-i-n structure currently recorded the highest power conversion efficiency to date. Most p-i-n configuration devices can be fabricated at temperatures below  $150^\circ\text{C}$  which makes them suitable for device fabrication on flexible substrates. The following subsection discuss the prons and cons

of both mesoporous and planar structures in terms of device performance.

### 3.5.1 Mesoporous/mesoscopic structures

Mesoscopic n-i-p structure was the first design for the preparation of the perovskite based solar cell which is still widely used in the fabrication of high performance solar cells. It consists of a TCO cathode from either FTO or ITO with range of thickness between 50 and 70 nm. It has thick mesoporous oxide layer (150 to 300 nm) from (mp-TiO<sub>2</sub> or mp-Al<sub>2</sub>O<sub>3</sub> or ZnO) which is eventually filled with perovskites photoactive layer up to 300 nm thick. This is followed by spiro-OMeTAD layer deposition of about 150 nm to 200 nm thick on top of the active layer which acts as a hole transport buffer material (HTM). Finally, metal anode electrode (Au or Ag) between 50 to 100 nm thick will be deposited to complete the device fabrication. The mesoscopic layer enhances charge collection by decreasing the carrier transport distance, preventing direct current leakage between the two selective contacts and increasing photon absorption due to light scattering in the medium. To date, the best planar n-i-p device achieved power conversion efficiency reached of 19.3 % through careful optimization of the electron selective ITO-TiO<sub>2</sub> interfaces. It also exhibits higher  $V_{OC}$  and  $J_{SC}$  relative to a comparative mesoscopic device processed with the same materials and approach. However, the planar device usually exhibits more severe J-V hysteresis [114]. The PCEs of the mesoporous perovskite devices have been higher than those of the planar devices due to a large diffusion length in planar devices which causes recombination of charge carriers.

### 3.5.2 Planar structures

In a planar configuration, upto hundreds of nanometer thick solar absorber layer can be fabricated which is sandwiched between ETM and HTM without a mesoporous scaffold. Planar architecture offers several advantages over mesoporous structure such as the ease and low temperature device processing, no requirement for vacuum deposition and compatible to roll to roll device fabrication. The inverted p-i-n type PSCs uses (PEDOT: PSS) as a hole transport layer and PCBM with its derivatives as n-type electron transport layers. Leijtens et al. found that the planar perovskite films were superior in terms of charge carrier mobility which showed greater

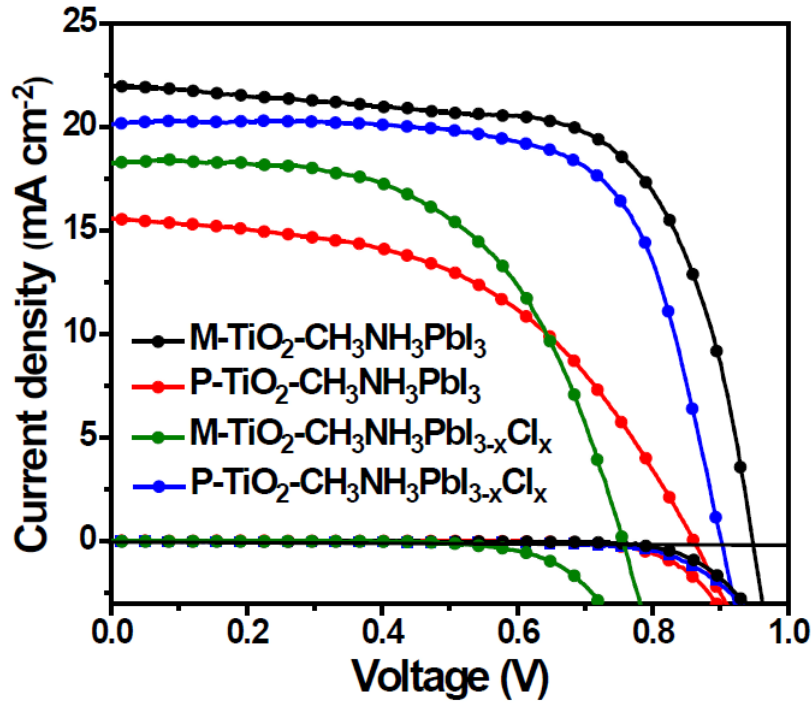


Fig. 3.15: Current-voltage(J-V) curves of the champion PSCs for mesoporous and planar configuration[87].

than  $20 \text{ cm}^2\text{V}^{-1}\text{s}^{-1}$ [70, 107, 108, 115]. Figure 3.15 compares the performance of devices produced using planar and mesoporous configuration. According to the result presented in Fig. 15 [87], planar structure out performed those produced using mesoporous structure for mixed halide perovskite while the mesoporous were better with halide perovskite. Jeon and co-workers fabricated and reported PSCs based on  $\text{CH}_3\text{NH}_3\text{PbI}_3$  combined with mesoscopic m- $\text{TiO}_2$  architecture with PCE as high as 16.7%[87]. However, solar cells prepared with planar configuration suffered from open circuit voltage loss which could be attributed to the high density of traps resulting in non-radiative electron-hole recombination [115]. Inverted planar (p-i-n structure) structure was designed to avoid the use of mesoporous  $\text{TiO}_2$  layer which requires high-temperature sintering and therefore substituted with cheap HTMs and ETMs. Unlike mesoscopic structure, the planar-type perovskite solar cells are facing numerous device imperfections associated with the formation of non-uniform perovskite films which has often contributed to lower device performance [26](Table 3.3).

Tab. 3.3: Summary of the device lead free perovskite solar cells

Active material	Deposition Method	ETM	HTM	$J_{SC}$ $mAcm^{-2}$	$V_{oc}$ V	FF %	PCE %	Year	Ref
$CH_3NH_3SnI_3$	Spin coating	c-TiO <sub>2</sub> /m-TiO <sub>2</sub>	Spiro-OMeTAD	16.8	0.88	42	6.4	2014	[122]
$CH_3NH_3SnI_3$	Spin coating	c-TiO <sub>2</sub>	Spiro-OMeTAD	19.9	0.32	37	4.18	2017	[123]
$FASnI_3$	Spin coating	m-TiO <sub>2</sub>	Spiro-OMeTAD	22.07	0.47	61	6.22	2017	[128]
$CH_3NH_3SnI_{3-x}Br_x$	Spin coating	c-TiO <sub>2</sub>	Spiro-OMeTAD	8.26	0.88	59	5.73	2014	[129]
$FAMASnI_3$	Spin coating	C <sub>60</sub> /Bathocuproine (BCP)	PEDOT: PSS	21.2	0.61	63	8.12	2017	[130]
$Cs_2SnI_6$	vapor deposition	c-TiO <sub>2</sub>	P3HT	5.41	0.51	35	0.96	2016	[131]
$CH_3NH_3SnCl_3$	Spin coating	c-TiO <sub>2</sub> /m-TiO <sub>2</sub>	PEO/ KI/ I <sub>2</sub>	1.5	0.6	59	0.55	2017	[132]

### Lead-free perovskite solar cells

Perovskite solar cells and all-solid-state perovskite solar cells still suffer from toxicity and long-term chemical instability of Lead under ambient conditions, specifically in the presence of air, humidity and light. Most research efforts are now geared towards identifying lead-free perovskite absorber materials for incorporation in the device manufacturing which could still lead to significant improvement in PCE [116–121]. Some of the promising alternative elements for lead include tin (Sn), caesium (Cs), germanium (Ge), copper (Cu), antimony (Sb) or bismuth (Bi) with tin-based perovskites being currently most promising with a PCE of 6.4%.  $HC(NH_2)_2SnI_3$  and inorganic perovskite  $CsSnI_3$  when used as solar energy harvesting material both achieve a PCE of 2% [122]. Alkaline-earth metals such as magnesium (Mg), calcium (Ca), strontium (Sr), and barium are also favourable materials with ionic radii close to that of lead. Tin-based perovskite materials are more susceptible to be oxidized than organic lead halide perovskite hence architectural and interface engineering is needed to further improve stability and enhance the performance of Sn-based PSCs [123, 124].

## 3.6 Charge transport buffer layers

The charge transport processes in perovskite based solar cell are influenced by the energy level alignment between the workfunction of the electrode and the active layer as well as the crystallinity of the photoactive medium. The energy levels alignment can be fine tuned by introducing ultrathin charge transport materials between the active layer and the electrodes [73]. Semiconductor metal oxides are the most popular choice of interfacial layers in organic-inorganic hybrid perovskite solar cells. Metal oxides such as TiO<sub>2</sub>, ZnO, Ta<sub>2</sub>O<sub>5</sub>, Al<sub>2</sub>O<sub>3</sub> and ZrO<sub>2</sub> have low work functions and are suitable for electron transport materials (ETM). On the other

hand, high workfunction metal oxides such as  $\text{MoO}_3$ ,  $\text{NiO}$ ,  $\text{CuO}$ , and  $\text{V}_2\text{O}_5$  are used as anode buffer layers known as hole transport materials (HTM). These metal oxides are chosen because of their ease of processability and low cost compared to pure metals. Some common salts and organic molecules are also used as interfacial layers in the preparation of organic solar cells, these includes polychlorinated biphenyl(BCP), Poly [(9,9-bis(3'-(N,N-dimethylamino)propyl)-2,7-fluorene)-alt-2,7-(9,9-dioctylfluorene)]PFN[125–127], Lithium Fluoride (LiF) and self-assembled  $\text{C}_{60}$  derivatives. The crystallinity of the photoactive medium is one of the critical factor for efficient generation and collection of photon induced charges. In recent years the use of solvent additives has become a popular practice to improve the crystallinity, film uniformity as well as device performance as presented in (Table 3.4) which will be discussed in details later. The role of buffer layers in the preparation of thin film solar cells are often aimed at preventing the active layers from adverse effect of humidity and oxygen, to align energy levels mismatch between active layers and electrodes, to assist charge transport process and serve as scaffold in the device structure. A detailed insight into some of the frequently used buffer layers in terms of performance enhancement is given in the following sections Table 4.5.

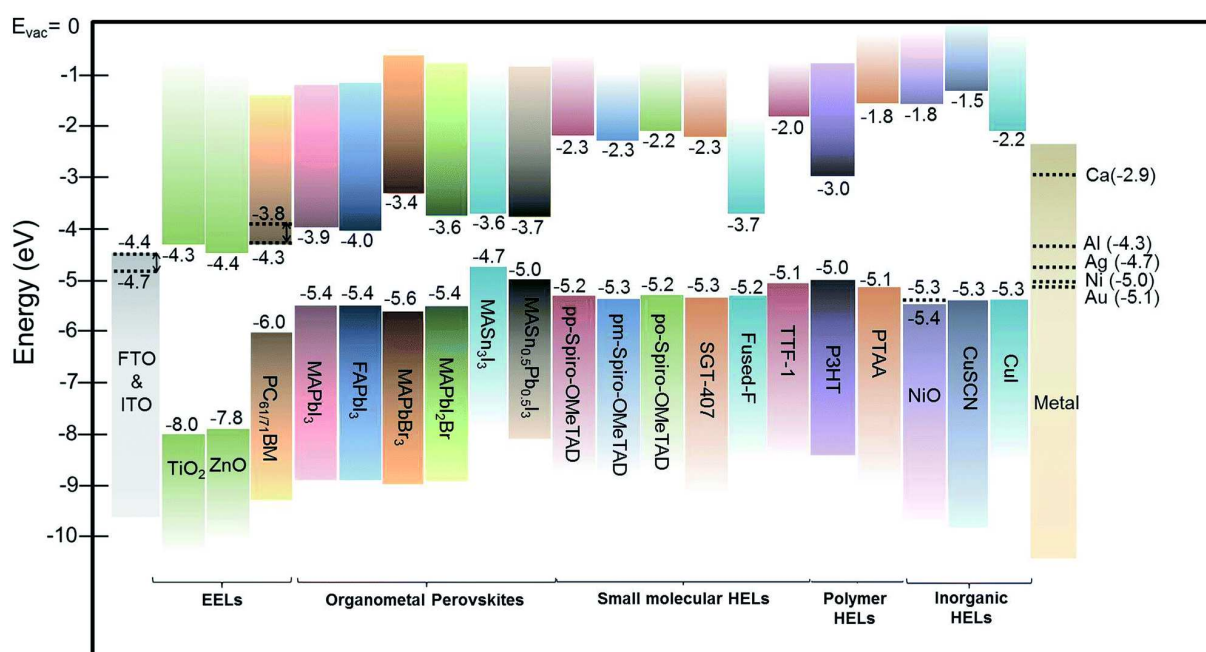


Fig. 3.16: Energy levels of the the various materials used as the electron selective contact material (ETM)(left), absorbers (middle) and hole selective contact materials (HTMs) (right) in the preparation perovskite based solar cells [25].

Tab. 3.4: Summary of the device evolution and performance of perovskite solar cells

Active material	Deposition Method	ETM	HTM	$J_{SC}$ mAc $m^{-2}$	$V_{oc}$ V	FF %	PCE %	Year	Ref
CH <sub>3</sub> NH <sub>3</sub> PbI <sub>3</sub>	Spin coating	WO <sub>3</sub>	Spiro-OMeTAD	17.0	0.87	0.76	11.24	2015	[8]
CH <sub>3</sub> NH <sub>3</sub> PbI <sub>3-x</sub> Cl <sub>x</sub>	Spin coating	PC <sub>61</sub> BM	PEDOT:PSS	17.4	0.92	0.73	11.62	2015	[26]
CH <sub>3</sub> NH <sub>3</sub> PbI <sub>3</sub>	Spin coating	PC <sub>61</sub> BM	PEDOT:PSS	13.09	0.9	0.83	9.46	2015	[27]
CH <sub>3</sub> NH <sub>3</sub> PbI <sub>3-x</sub> Cl <sub>x</sub>	Spin coating	PCBM	NiO	15.62	1.07	0.64	10.68	2015	[28]
CH <sub>3</sub> NH <sub>3</sub> I	Spin coating	TiO <sub>2</sub> /TiAc <sub>2</sub>	Spiro-OMeTAD	20.3	1.02	0.766	15.7	2015	[29]
CH <sub>3</sub> NH <sub>3</sub> I	Spin coating	C <sub>60</sub> Bphen	PEDOT:PSS	20.9	1.02	0.72	15.4	2014	[30]
CH <sub>3</sub> NH <sub>3</sub> PbI <sub>3-x</sub> Cl <sub>x</sub>	Spin coating	TiO <sub>2</sub> /Graphene	Spiro-OMeTAD	21.9	1.04	0.73	15.6	2014	[31]
CH <sub>3</sub> NH <sub>3</sub> PbI <sub>3-x</sub> Cl <sub>x</sub>	Hybrid ev. method	-	-	17.0	1.09	0.535	9.9	2014	[32]
CH <sub>3</sub> NH <sub>3</sub> PbI <sub>3</sub>	Spin coating	TiO <sub>2</sub>	Spiro-OMeTAD	13.14	1.029	0.426	5.77	2014	[33]
CH <sub>3</sub> NH <sub>3</sub> PbI <sub>3-x</sub> Cl <sub>x</sub>	Spin coating	c-TiO <sub>2</sub>	PTB7	20.2	0.94	0.70	13.29	2015	[34]
CH <sub>3</sub> NH <sub>3</sub> PbI <sub>3-x</sub> Cl <sub>x</sub>	Spin coating	TiO <sub>2</sub>	Spiro-OMeTAD	18.26	1.09	0.607	12.1	2015	[35]
CH <sub>3</sub> NH <sub>3</sub> PbI <sub>3</sub>	Spin coating	PC <sub>61</sub> BM	PEDOT:PSS	21.55	0.86	0.75	13.85	2015	[36]
CH <sub>3</sub> NH <sub>3</sub> PbI <sub>3-x</sub> Cl <sub>x</sub>	C3-SAM	PC <sub>61</sub> BM	PEDOT:PSS	18.9	0.89	0.691	11.6	2015	[37]
CH <sub>3</sub> NH <sub>3</sub> PbI <sub>3-x</sub> Cl <sub>x</sub>	Spin coating	TiO <sub>2</sub>	Spiro-OMeTAD	18.9	0.972	0.616	12.7	2015	[38]
CH <sub>3</sub> NH <sub>3</sub> PbI <sub>3</sub>	Spin coating	TiO <sub>2</sub>	Spiro-OMeTAD	17.6	0.995	0.70	12.3	2014	[39]
CH <sub>3</sub> NH <sub>3</sub> PbI <sub>3-x</sub> Cl <sub>x</sub>	Spin coating	TiO <sub>2</sub>	Spiro-OMeTAD	18	0.97	0.64	11.2	2015	[40]
CH <sub>3</sub> NH <sub>3</sub> PbI <sub>3</sub>	Spin coating	TiO <sub>2</sub>	Spiro-OMeTAD	15.9	0.95	0.61	9.2	2015	[40]
CH <sub>3</sub> NH <sub>3</sub> PbBr <sub>3</sub>	Spin coating	c-TiO <sub>2</sub>	Spiro-OMeTAD	7.55	1.42	0.77	8.29	2015	[41]
CH <sub>3</sub> NH <sub>3</sub> PbI <sub>3</sub>	Elec.deposition	c-TiO <sub>2</sub>	Spiro-OMeTAD	20.97	0.98	0.71	14.59	2015	[42]
CH <sub>3</sub> NH <sub>3</sub> PbI <sub>3-x</sub> Cl <sub>x</sub>	Spin coating	PCBM/ZnO	PEDOT:PSS	19.6	0.98	0.74	14.2	2015	[43]
CH <sub>3</sub> NH <sub>3</sub> PbI <sub>3-x</sub> Cl <sub>x</sub>	Spin coating	CuAlO <sub>2</sub>	PEDOT:PSS	21.98	0.88	0.75	14.52	2016	[44]
CH <sub>3</sub> NH <sub>3</sub> PbI <sub>3</sub>	Spin coating	PC <sub>61</sub> BM/BCB	Red. GPO	15.4	0.98	0.716	10.8	2014	[45]
CH <sub>3</sub> NH <sub>3</sub> PbI <sub>3</sub>	Spin coating	c-TiO <sub>2</sub>	Spiro-OMeTAD	17.6	1.0	0.734	13.0	2014	[46]
CH <sub>3</sub> NH <sub>3</sub> PbI <sub>3</sub>	Spin coating	C <sub>60</sub> /PCB	PPP	21	1.02	0.71	15.8	2015	[47]
CH <sub>3</sub> NH <sub>3</sub> PbI <sub>3</sub>	Spin coating	c-TiO <sub>2</sub>	Spiro-OMeTAD	22.19	1.01	0.72	16.1	2015	[8]
CH <sub>3</sub> NH <sub>3</sub> PbI <sub>3</sub>	Spin coating	WO <sub>3</sub> -NP,NR NS	Spiro-OMeTAD	17	0.87	0.76	11.24	2015	[26]
CH <sub>3</sub> NH <sub>3</sub> PbI <sub>3</sub>	Spin coating	PC <sub>61</sub> BM	PEDOT:PSS	18.95	0.94	0.72	12.88	2015	[26]
CH <sub>3</sub> NH <sub>3</sub> PbI <sub>3</sub>	Spin coating	TiO <sub>2</sub>	Without HTM	18.9	0.77	0.65	9.4	2014	[48]
CH <sub>3</sub> NH <sub>3</sub> PbI <sub>3</sub>	Spin coating	TiO <sub>2</sub>	Remnant PbI <sub>2</sub>	15.1	1.036	0.62	9.7	2014	[49]
CH <sub>3</sub> NH <sub>3</sub> PbI <sub>3</sub>	Spin coating	TiO <sub>2</sub>	Spiro-OMeTAD	22.3	0.96	0.67	14.3	2014	[9]
CH <sub>3</sub> NH <sub>3</sub> PbI <sub>3</sub>	Spin coating	TiO <sub>2</sub>	P3HT	21.76	0.96	0.653	13.7	2015	[50]
CH <sub>3</sub> NH <sub>3</sub> PbI <sub>3-x</sub> Cl <sub>x</sub>	Spin coating	c-TiO <sub>2</sub>	Spiro-OMeTAD	21.5	1.07	0.67	15.4	2013	[51]
CH <sub>3</sub> NH <sub>3</sub> PbI <sub>3</sub>	Spin coating	m-TiO <sub>2</sub>	Spiro-OMeTAD	17.6	0.888	0.62	9.7	2012	[52]
CH <sub>3</sub> NH <sub>3</sub> PbBr <sub>3</sub>	Spin coating	TiO <sub>2</sub>	-	5.57	0.96	0.59	3.13	2009	[15]
CH <sub>3</sub> NH <sub>3</sub> PbI <sub>3</sub>	Spin coating	TiO <sub>2</sub>	-	11	0.61	0.61	3.81	2009	[15]
CH <sub>3</sub> NH <sub>3</sub> PbI <sub>3-x</sub> Cl <sub>x</sub>	Spin coating	PCBM	PEDOT:PSS	17.5	0.88	0.676	10.4	2014	[53]
CH <sub>3</sub> NH <sub>3</sub> PbI <sub>3</sub>	Spin coating	m-TiO <sub>2</sub>	Spiro-OMeTAD	20.3	0.91	0.71	12.8	2016	[54]
CH <sub>3</sub> NH <sub>3</sub> PbI <sub>3</sub>	Spin coating	m-TiO <sub>2</sub>	Without HTM	12.10	0.82	0.562	5.60	2015	[55]
CH <sub>3</sub> NH <sub>3</sub> PbI <sub>3</sub>	Spin coating	m-TiO <sub>2</sub>	with HTM	12.45	0.95	0.595	7.04	2015	[55]
CH <sub>3</sub> NH <sub>3</sub> PbI <sub>3</sub>	Spin coating	PC <sub>61</sub> BM	PEDOT:PSS	21.58	0.84	0.614	11.12	2015	[56]
CH <sub>3</sub> NH <sub>3</sub> PbI <sub>2</sub> Cl	Spin coating	TiO <sub>2</sub>	Spiro-OMeTAD	17.8	0.98	0.63	10.9	2012	[57]
CH <sub>3</sub> NH <sub>3</sub> PbI <sub>3</sub>	Spin coating	ZnO	Spiro-OMeTAD	20.4	1.03	0.75	15.7	2013	[58]
CH <sub>3</sub> NH <sub>3</sub> PbI <sub>3</sub>	Spin coating	m-TiO <sub>2</sub>	Spiro-OMeTAD	20.0	0.993	0.73	15.0	2013	[20]
CH <sub>3</sub> NH <sub>3</sub> PbI <sub>3</sub>	Spin coating	m-TiO <sub>2</sub>	Spiro-OMeTAD	21.3	1.0	0.66	14.1	2013	[20]
CH <sub>3</sub> NH <sub>3</sub> PbI <sub>3-x</sub> Cl <sub>x</sub>	Spin coating	m-TiO <sub>2</sub> /Al <sub>2</sub> O <sub>3</sub>	Spiro-OMeTAD	21.5	1.02	0.71	15.9	2014	[59]
CH <sub>3</sub> NH <sub>3</sub> PbI <sub>3</sub>	Spin coating	m-TiO <sub>2</sub> /Al <sub>2</sub> O <sub>3</sub>	Spiro-OMeTAD	23.83	1.086	0.762	19.71	2015	[10]
CH <sub>3</sub> NH <sub>3</sub> PbI <sub>3-x</sub> Cl <sub>x</sub>	Spin coating	Y-TiO <sub>2</sub>	Spiro-OMeTAD	22.75	1.13	75.01	19.3	2014	[11]
FAPbI <sub>3</sub>	direct intra-molecular exchange	m-TiO <sub>2</sub>	PTAA	24.7	1.06	77.5	20.2	2015	[60]
CH <sub>3</sub> NH <sub>3</sub> PbI <sub>3</sub>	Spin coating	m-TiO <sub>2</sub>	Spiro-OMeTAD	23.69	1.113	77.3	20.4	2016	[12]

### 3.6.1 Hole transport materials (HTMs)

The hole transport materials (HTMs) in the device structure of organic and perovskite based solar cell does not only improve the power conversion efficiency but also enhances the device stability. HTMs currently form an integral part of perovskite solar cells. The ideal characteristics of HTMs are a high hole mobility, a good thermal and UV stability, and a well matched HOMO energy to the perovskites. HTMs are the necessary interface modification layer between perovskite and anode in inverted planar PSCs (see Fig. 3.16). They function as hole selective contact which significantly enhances hole collection ability, reduces charge recombination and increases built-in voltage. A number of materials both from organic and inorganic source have been used as HTMs in the fabrication of PSCs. However, the inorganic HTMs are hindered by the limited choice of materials and results relatively lower PCE solar cells. Organolead halide perovskites are more conductive than the HTMs currently used hence there is need for a capping layer of HTM to prevent contact between the perovskite and metal cathode. However, this increases the series resistance and decreases the FF of the resulting cells. They are composed of organic and inorganic hole-conductors. Organic hole-conductors can be further divided into three categories namely: small molecule hole-conductors like Triphenylamine (TPA)-based compounds such as spiro-MeOTAD, conducting polymers like Polythiophene-based conducting polymer poly(3-hexylthiophene-2,5-diyl) (P3HT) and organometallic compounds such as Copper phthalocyanine (CuPc). Depositing the HTM within an insulating mesoporous buffer layer comprising of  $\text{Al}_2\text{O}_3$  nanoparticles, prevents the metal electrode migration while at the same time allow for precise control of the HTM thickness. PEDOT:PSS, P3HT: PCBM and metal oxides NiO,  $\text{V}_2\text{O}_5$ ,  $\text{MoO}_3$  and  $\text{WO}_3$  have also been widely used as HTM [133–135]. Hole extraction takes place at the HTM/perovskite layer interface. Hence it is necessary to achieve meaningful electron blocking and efficient hole extraction through interface engineering between the HTM and the perovskite film. HTM layer above the perovskite film protect the perovskite from atmospheric moisture. Interfacial engineering through the use of ultrathin compact and non-conductive aluminium oxide layer either below or above the HTM has also been reported to enhance the stability of PSCs. Little attention has been paid to the development of inorganic HTMs with favourable energy levels like CuI and  $\text{NiO}_x$ . However, due to their high

mobility, stability, the ease of synthesis and low cost, lots of attention has been devoted to the development of suitable organic charge transport materials in order to improve the device performance. Good HTMs should have appropriate HOMO for efficient electron blocking and hole collection, high hole mobility, stable thermal and optical properties, along with the ability to be doped. A high conductive HTM, reduces the series resistance and improves the fill factor of the cell. Metal oxide semiconductors such as molybdenum oxide, tungsten oxide, and vanadium oxide are commonly used p-type semiconductors for HTMs. The properties of the most popular HTMs in the preparation of perovskite solar cells are discussed as follows.

### *Inorganic HTMs*

Inorganic p-type semiconductors, such as cuprous iodide (CuI), cuprous bromide (CuBr), cuprous thiocyanate (CuSCN) and nickel oxide (NiO) were first introduced as the hole transporters for DSSCs which resulted in PCEs around 3 % [136]. However, such inorganic hole conductors suffer from the easy crystallization, poor solubility and inadequate pore filling problems which are unfavourable for fabrication of high performance perovskite solar cell. Nonetheless, they exhibit considerable conductivity which increases the FF of the fabricated devices. However, there are a number of easy processable inorganic semiconductor metal oxides which are often used in the device fabrication process. These are Nickel oxide (NiO<sub>x</sub>), Vanadium pentoxide (V<sub>2</sub>O<sub>5</sub>), Molybdenum oxide (MoO<sub>3</sub>) etc. We discuss here the properties of some of the popular inorganic HTM:

**Copper iodide (CuI):** Copper iodide (CuI) is highly conductive and wide band-gap (3.1 eV) semiconductor with a work function of -5.1 eV. It is a chemically stable, low cost and solution processable inorganic hole conductor. CuI is p-type conductor and is compatible with the solution deposition methods with the organo-lead halide perovskite. Impedance spectroscopy revealed that CuI exhibits two orders of magnitude higher electrical conductivity than spiro-OMeTAD which allows for significantly higher fill factors [137]. CuI exhibits higher recombination and lower  $V_{oc}$  (0.6 V) compared to spiro-OMeTAD. The energy level of CuI is not favourably matched with the perovskite crystals which resulted in low open circuit voltage in the device.

**Copper thiocyanate (CuSCN):** Copper thiocyanate (CuSCN) is also a wide bandgap (3.6 eV) semiconductor and has a work function of about -5.3 eV. The conductivity ranges between  $10^{-2}$ - $10^{-3}$  S cm<sup>-1</sup>), good stability, shows good transparency throughout the visible and near infrared spectrum. CuSCN has a high hole mobility of 0.01 cm<sup>2</sup>V<sup>-1</sup>s<sup>-1</sup> (in comparison with with  $4 \times 10^{-5}$  cm<sup>2</sup>V<sup>-1</sup>s<sup>-1</sup> for spiro-OMeTAD). It has good chemical stability. It can be deposited through a solution processing approach at low temperature, making it compatible with flexible substrates [138]. By using copper thiocyanate (CuSCN) instead of P3HT as the HTL, a higher device PCE was achieved. The quality and hole transfer ability of CuSCN can be improved by producing the HTM film using various deposition methods. Electro-deposited CuSCN was used as the HTM for p-i-n perovskite solar cells and a 16.6 % PCE was obtained [139]. However, compared to spiro-OMeTAD, CuSCN has a lower  $V_{OC}$  leading to a lower PCE .

**Nickel oxide (NiO<sub>x</sub>):** NiO<sub>x</sub> is a cubic p-type semiconductor and usually hybrid with Ni (III) or Ni (IV) oxide which exhibits wide energy band gap (3.5 - 4.0) eV range which offers sufficient optical transparency in the visible spectral region that allow solar radiation access to the active layer. It has high transmittance and deep work function of about -5.3 eV. Zhu et al, obtained power conversion efficiency of 9.11 %, which is by far the highest reported for planar perovskite solar cells based on an inorganic hole-extracting layer.[140]. Figure 3.17 shows a typical example of the role of various HTMs on the performance of the solar cell devices. The use of NiO appeared to have significant influence in this particular investigation. However, the addition of thin layer of meso-Al<sub>2</sub>O<sub>3</sub> have contributed to stability of the device and resulted a power conversion efficiency of over 11 % [141].

**Vanadium pentoxide (V<sub>2</sub>O<sub>5</sub>):** Vanadium pentoxide is a p-type material that can be used for efficient hole-injection into materials with absorption band partly covering the absorption band of PC<sub>71</sub>BM, a narrow band-gap of 2.8 eV and work function of 7.0 eV which provides a good Ohmic contact to the HOMO of organic materials and has electron affinity of 9.5 eV. However, it is highly sensitive to the ambient environment [143, 144].

**Molybdenum oxide (MoO<sub>3</sub>):** Molybdenum oxide is a wide band gap p-type semi-

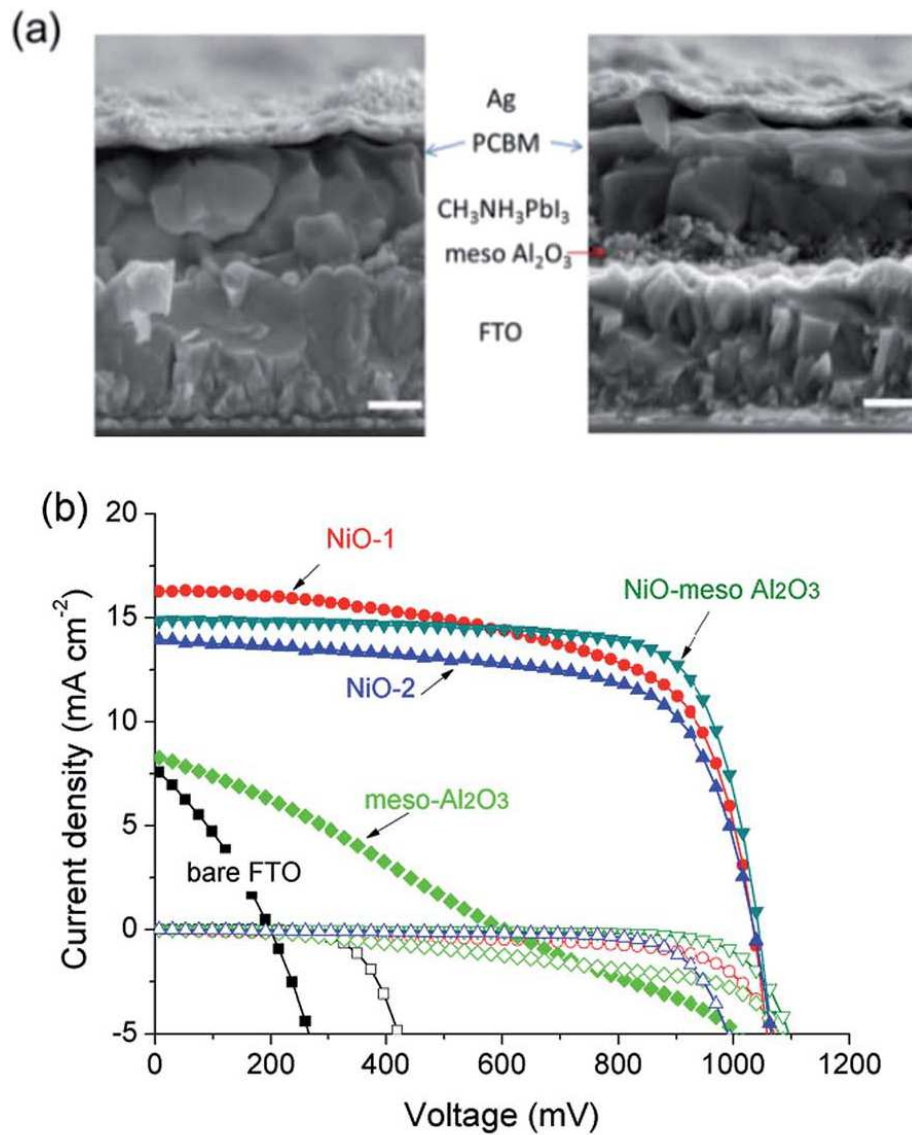


Fig. 3.17: (a) The SEM cross sectional view of the perovskite film morphology (b) J-V characteristics of the solar cells prepared with different hole transport materials [142].

conductor with energy band gap  $E_g = 3$  eV. The MoO<sub>3</sub> HTL reduces the charge recombination by suppressing the exciton quenching as well as the resistance at the photoactive layer/anode interface. It serves as an optical spacer for improving light absorption, thereby enhancing the photocurrent. MoO<sub>3</sub> has the advantage of precise thickness control in the nanoscale range of about 1–2 nm through vacuum-deposition/thermal evaporation however, MoO<sub>3</sub> is highly sensitive to oxygen and moisture; even the trace amounts of oxygen in the nitrogen filled glove box during device fabrication are shown to have negative effects on its electronic levels, resulting in adverse consequences in the device stability.[134]

**Tungsten trioxide (WO<sub>3</sub>):** WO<sub>3</sub> is a low-cost, nontoxic and volatile HTM with high work function of (-4.8 eV) which greatly enhances the hole transport and collection at the WO<sub>3</sub>/electrode (anode) interface. It suppresses the contact resistance remarkably and reduce series resistance[135]. The s-WO<sub>3</sub> layer shows a high hole mobility of  $9.4 \times 10^{-3} \text{cm}^2/\text{V}^{-\text{s}}$  and high light transmittance. PSCs with the s-WO<sub>3</sub> anode buffer layer show enhanced photovoltaic performance in comparison with the devices with PEDOT:PSS as the anode buffer layer[136].

### *Organic HTMs*

**Spiro-MeOTAD:** Spiro-OMeTAD is an excellent small molecule HTM. It has both large solubility and does not require any post-annealing treatment. It is also nonreactive to perovskite and is less volatile. The matched band gap with perovskite, amorphous nature, good conductivity with dopants, and high melting point of Spiro-OMeTAD make it one of the best HTMs in PSCs. Its suitable affinity with the perovskite layer, associated with a favourable energy configuration, also reduces charge recombination. Spiro-MeOTAD however, suffers from low hole mobility of  $10^{-4} \text{cm}^2 \text{V}^{-1} \text{s}^{-1}$  which results in high interfacial recombination losses, and conductivity, owing to its pristine, unique structure. Spiro-MeOTAD is expensive and needs extra treatments such as doping. Additives, such as, Li-bis(trifluoromethanesulfonyl) imide (Li-TFSI), perfluoro-tetracyanoquinodimethane (F4TCNQ) and tris(2-(1H-pyrazol-1-yl) pyridine) cobalt(III) (FK102 Co(III)) are necessary to dope and improve conductivity of spiro-MeOTAD however, the use of dopants/additives induces device instability, and the oxidized form of the Spiro-OMeTAD acts as a filter around 520 nm owing to an increased absorption in this region. Spiro-OMeTAD is smaller than P3HT, which leads to better pore filling and sensitizer regeneration but the the low electrical conductivity and extensive synthetic process for spiro-OMeTAD limits its use in large-scale operations and Pristine Spiro-OMeTAD is essentially a poorly conducting insulator, causing devices to suffer from high series resistance ( $R_s$ ) owing to poor hole transport through the device[145].

However, currently, spiro-OMeTAD is the best solid-state hole transporting material used in most high-efficiency hybrid perovskite solar cells due its ionisation potential which well matched to a number of active solar absorbers like perovskite, sensitizer

or the electron-transport layers. It has smaller molecular size which leads to better pore filling and sensitizer regeneration leading to the highest value reported to date for perovskite-based solar cells with spiro-OMeTAD as hole transport material (See Fig. 3.20). **Poly(3-hexylthiophene-2,5-diyl)(P3HT)**: Poly (3-hexylthiophene-2, 5-diyl) (P3HT), has also been reported to be cost-effective and has high mobility compared to spiro-OMeTAD in solar cells. Figure 18 below shows the J-V curve of spiro-OMeTAD, P3HT MEH-PPV and based devices [122, 146]. Spiro-OMeTAD

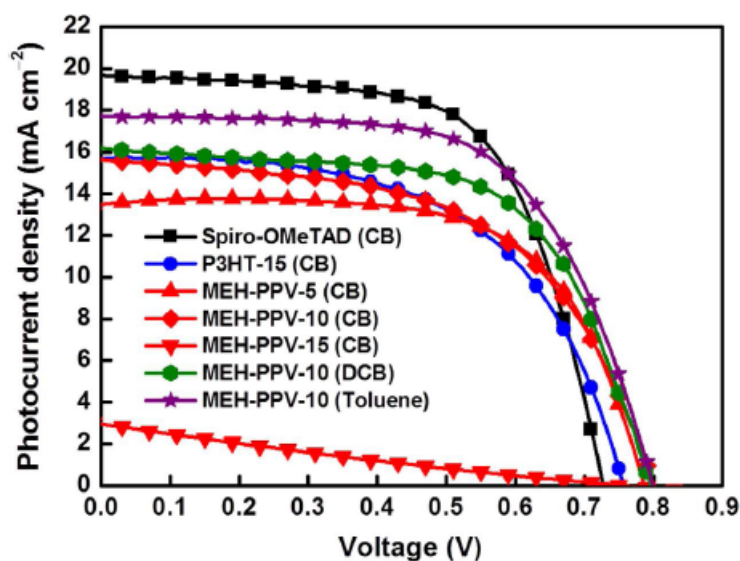


Fig. 3.18: J-V curves of spiro-MeOTAD-based (black curve) and P3HT based devices (blue curve) devices[4].

requires an additive, like 4-tert-butylpyridine (TBP) or bis(trifluoromethane) sulfonimidelithiumsalt (Li-TFSI), to improve the conductivity but these additives break-down the perovskite layer, reducing the stability of the device [147, 148].

**Poly[bis(4-phenyl)(2,4,6-trimethylphenyl)amine](PTAA)**: poly[bis(4-phenyl)(2,4,6-trimethylphenyl)amine](PTAA) has favourable hole mobility and suitable HOMO level required of a perovskite interlayer. A certified PCE of 16.2 % has been achieved by using PTAA as the HTM via a solvent engineering method. PTAA as the HTL, incorporation of  $MAPbBr_3$  into  $FAPbI_3$  stabilizes the perovskite phase of  $FAPbI_3$  and improves the open-circuit voltage ( $V_{OC}$ ) fill factor (FF) and the power conversion efficiency of the solar cell to more than 18 % [139, 149].

**4-Diethylamino)benzaldehyde diphenylhydrazone(DEH)**: The size of DEH is smaller than that of spiro-OMeTAD, and therefore has better pore filling ability .

UV/Vis spectra show that P3HT absorbs light in the visible region, whereas DEH and spiro-OMeTAD do not [150].

The active layer PSC device is composed of a blend film of conjugated poly-

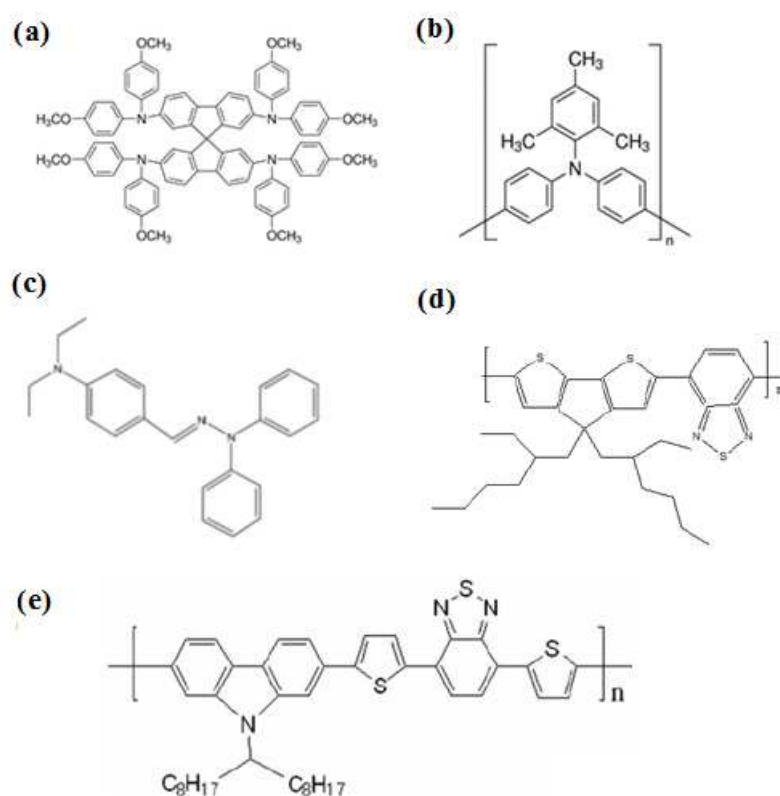


Fig. 3.19: Examples of most commonly used HTL (a) Spiro-OMeTAD (b) PTAA and (c) DEH (d) PCPDTBT (e) PCDTBT

mer (as electron donor) and a small molecular acceptor.[151]. Jeon et al, used a mixed solvent of GBL and DMSO followed by toluene drop-casting which led to extremely uniform and dense perovskite layers via a  $\text{CH}_3\text{NH}_3\text{IPbI}_2$ -DMSO intermediate phase, and enables the fabrication of improved solar cells with a certified power-conversion efficiency of 16.2 % and no hysteresis. The three most common HTLs, which have yielded the highest efficiency results, are 2,2,-7,7-tetrakis-(N,N di-p-methoxyphenylamine)-9,9-spirobifluorene(Spiro-OMeTAD), poly(3-hexyl-thiophene), (P3HT), and poly[bis(4-phenyl)(2,4,6-trimethylphenyl)amine],(PTAA) (Fig. 3.18 and Fig. 19)[152].

### 3.6.2 Electron transport materials (ETMs)

Titanium oxide ( $\text{TiO}_2$ ) and zinc oxide ( $\text{ZnO}$ ) are the most frequently used inorganic electron transport materials (ETMs) in conjunction with HTMs such as CuI, CuSCN

and NiO in the preparation of organic-inorganic hybrid perovskite solar cells. Transition metal oxides like molybdenum trioxide ( $\text{MoO}_3$ ), tungsten trioxide ( $\text{WO}_3$ ), nickel oxide or vanadium pentoxide ( $\text{V}_2\text{O}_5$ ) can also effectively replace the water soluble organic HTMs known as PEDOT:PSS. Moreover, these metal oxide materials are not vulnerable to the acidity of  $\text{CH}_3\text{NH}_3\text{I}$ . Fig. 16 shows the energy levels of the most common electron transport materials in the preparation perovskite based solar cells[153]. Brief review of the frequently used ETMs are thus, given below:

**Titanium oxide ( $\text{TiO}_2$ ):** it is a large band gap semiconductor with a band gap of 3.02 eV and 3.20 eV for rutile phase and anatase phases respectively. The conduction band edge lying at 4.1 eV slightly lower than that of  $\text{CH}_3\text{NH}_3\text{PbI}_3$  (Fig 16) which is ensuring direct electron injection from perovskite absorber to ETM. It is also a very good hole blocking layer due to its low lying valence band edge [154].  $\text{TiO}_2$  can be produced as mesoporous films or rod and tube-shaped nanostructures. Currently,  $\text{TiO}_2$  ETLs have been used in most commonly reported PSCs due to its suitable energy level, good optical transparency, relatively high electron mobility and environmental stability. The ease of  $\text{TiO}_2$  film preparation, long electron lifetimes and favourable electron injection rates from the perovskite absorber to  $\text{TiO}_2$  makes it an ideal ETMs for thin film solar cells. Unfortunately, perovskite solar cells based on  $\text{TiO}_2$  interlayer usually displays lower performance due to poor conductivity of the film and light soaking problems.

**Zinc oxide ( $\text{ZnO}$ ):** High electron mobility, high thermal conductivity, wide and direct band gap and large exciton binding energy make  $\text{ZnO}$  suitable for a wide range of devices.  $\text{ZnO}$  is low cost material, with 4.2 eV of conduction band minimal (CBM), 3.3 eV of direct band gap and 60 meV of exciton binding energy at room temperature. It is easily synthesized, non-toxic with relatively high electron mobility, environmental stability, and high transparency, and unique optoelectronic properties. Due to its large band gap energy, the ionization potential of  $\text{ZnO}$  is large enough to make it act as a hole blocker and thus increases the shunt resistance of a PV solar cell. Optically,  $\text{ZnO}$  absorbs in the UV part of the spectrum and therefore it functions as a low-pass filter for  $\text{PC}_{71}\text{BM}$ . It also has a low work function of  $\approx 4.30\text{eV}$ , which offers a suitable energy level to reduce work function of ITO or metal electrodes, and to match with LUMO levels of various fullerene-based acceptors such as [6,6]-phenyl-C61-butyric acid methyl ester (PCBM),  $\text{PC}_{71}\text{BM}$ , and indene- $\text{C}_{60}$  bis-adduct (ICBA).  $\text{ZnO}$  has better electron mobility than  $\text{TiO}_2$

and ZnO nanorods and nanoparticles have both been used often in the PSCs as ETLs yielding higher PCEs. The conductivity of ZnO is several orders of magnitude higher than that of TiO<sub>2</sub> hence loss through recombination will be minimized due to higher electron mobility. Also, high temperature sintering process is not needed for the fabrication of ZnO however, ZnO based devices suffer from serious interfacial recombination, which can be attributed to defect-induced recombination at the interface between metal oxide and active layer and also from chemical instability[155].

**Tin oxide (SnO<sub>2</sub>)** SnO<sub>2</sub> has a wide band-gap, high transparency and higher intrinsic electron mobility compared to other n-type oxides, which offers it an advantages of being an efficient carrier transport material. However, SnO<sub>2</sub> based devices are affected by serious hysteresis behaviour.

In conventional structure (n-i-p), the most common ETM and HTM materials reported in the literature are TiO<sub>2</sub> and 2,2',7,7'-tetrakis-(N,Ni-p-methoxyphenylamine)-9,9'-spirobifluorene (spiro-OMeTAD), respectively while, mesostructured TiO<sub>2</sub> or Al<sub>2</sub>O<sub>3</sub> planar electrodes have been widely used in these cells as a hole blocking electrodes (ETL). Currently, there has not been much investigation into the improvement of the electron transport material (ETM) in perovskite solar cells and TiO<sub>2</sub> is currently the most useful ETM in high performing cells. TiO<sub>2</sub> degradation under UV irradiation and the high temperature needed for the sintering process makes it unsuitable for low-cost production and for the fabrication of flexible substrates. However the HTL-free perovskite solar cell is more stable than the device using PEDOT: PSS.

### 3.7 The effect of solvent additives

Solvent additives have been used in the preparation of organic photovoltaic device processing to optimize the active layer film morphology which impacted positively on the performance of the devices. The use of solvent additives have become a common practice in recent years to improve the crystallinity of the photoactive medium. Integration of small amounts of solvent additives in perovskite precursor solutions have been reported to improve crystallinity, film uniformity and the resulting device performance[156] (Table 3.4). Before addressing the issue of solvent additives

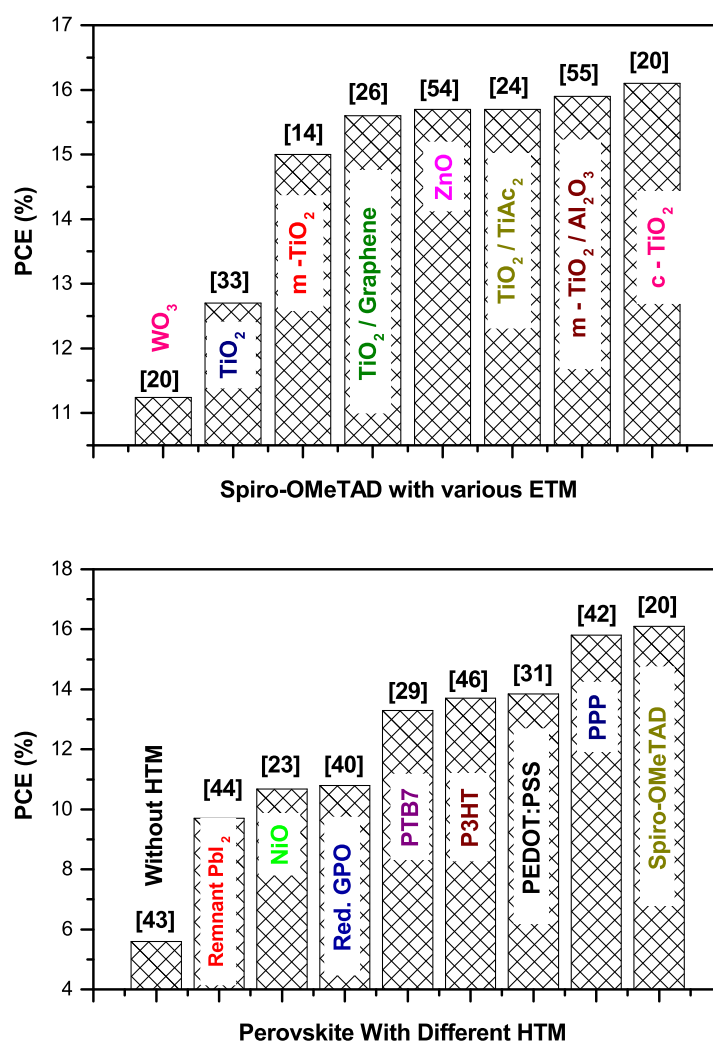


Fig. 3.20: Best ETM and HTM used in the preparation of high performance perovskite solar cell.

it is noteworthy to discuss the role of host solvents themselves. The most common types of host solvent in the preparation lead halides and MAI solutions are DMF, DMSO, GBL, and N-methyl-2-pyrrolidone (NMP). The organic solvents such as chlorobenzene, benzene, xylene, toluene, 2-propanol and chloroform are poor solvents to make a solutions from lead halides and MAI compounds but they suited best for organic conducting polymers and buffer layer materials. Perovskite films casted using DMF solvent are reported to cause pinholes and voids at the surface of the film as well as in the bulk of the active layer due to the formation of intermediate compounds, such as MAPbI<sub>3</sub>:DMSO, MAPbI<sub>3</sub>:DMF or MAPbI<sub>3</sub>:H<sub>2</sub>O. The perovskite film produced using DMF with a boiling point of 153°C do not allow an easy control over the crystal structure of the film. However, DMSO or GBL with higher boiling

Tab. 3.5: Table of Additives and power conversion efficiencies

Perovskite	deposition method	Additive	PCE% without	PCE% with	J <sub>SC</sub> mA/cm <sup>2</sup>	V <sub>OC</sub> volts	Year	Ref
1	CH <sub>3</sub> NH <sub>3</sub> PbI <sub>3</sub>	two-step solution	-	19.68	22.69	1.15	2016	[160]
2	CH <sub>3</sub> NH <sub>3</sub> PbI <sub>3</sub>	Spin-coating	3.67	9.74	15.97	1.05	2016	[161]
3	HC(NH <sub>2</sub> ) <sub>2</sub> PbI <sub>3</sub>	One-step solution	14.33	16.53	23.84	1.04	2016	[162]
4	CH <sub>3</sub> NH <sub>3</sub> PbI <sub>3</sub>	two-step solution	11.4	12.77	17.59	0.96	2016	[159]
4a	CH <sub>3</sub> NH <sub>3</sub> PbI <sub>3</sub>	two-step solution	11.4	15.08	19.42	1.04	2016	[159]
4b	CH <sub>3</sub> NH <sub>3</sub> PbI <sub>3</sub>	two-step solution	11.4	9.98	15.97	0.90	2016	[159]
5	CH <sub>3</sub> NH <sub>3</sub> PbI <sub>3</sub>	One-step solution	8.8	16.7	15.6	0.86	2015	[163]
6	CH <sub>3</sub> NH <sub>3</sub> PbI <sub>3</sub>	Two-step spin-coating	6.71	10.62	17.12	0.92	2015	[164]
6	CH <sub>3</sub> NH <sub>3</sub> PbI <sub>3-x</sub> Cl <sub>x</sub>	One-step spin-coating	11.11	15.01	22.47	0.82	2015	[164]
7	CH <sub>3</sub> NH <sub>3</sub> PbI <sub>3-x</sub> Cl <sub>x</sub>	spin-coating	9.4	10.2	16.8	0.86	2015	[165]
8	CH <sub>3</sub> NH <sub>3</sub> PbI <sub>3</sub>	pyrolysis/spin-coating	5.7	13.7	20.1	0.92	2014	[166]
9	CH <sub>3</sub> NH <sub>3</sub> PbI <sub>3</sub>	spin-coating	10.58	14.42	20.7	1.04	2015	[167]
10	CH <sub>3</sub> NH <sub>3</sub> PbI <sub>3</sub>	spin-coating	7.2	15	0.95	0.97	2015	[168]
11	CH <sub>3</sub> NH <sub>3</sub> PbI <sub>3-x</sub> Cl <sub>x</sub>	spin-coating	12.13	16.06	20.78	0.95	2015	[169]
12	CH <sub>3</sub> NH <sub>3</sub> PbI <sub>3-x</sub> Cl <sub>x</sub>	spin-coating	5.1	9.7	21.8	0.86	2015	[170]
13	CH <sub>3</sub> NH <sub>3</sub> PbI <sub>3</sub>	spin-coating	9.5	12	20.02	0.83	2017	[171]
14	CH <sub>3</sub> NH <sub>3</sub> PbI <sub>3</sub>	simple solution based	16.5	18.1-19	23.7	1.05	2017	[172]
15	CH <sub>3</sub> NH <sub>3</sub> PbI <sub>3-x</sub> Cl <sub>x</sub>	spin-coating	7.7	11.9	12.8	0.73	2017	[173]
15	CH <sub>3</sub> NH <sub>3</sub> PbI <sub>3-x</sub> Cl <sub>x</sub>	Spray cast	6.1	10	19.3	0.91	2017	[173]
16	CH <sub>3</sub> NH <sub>3</sub> PbI <sub>3</sub>	two-step solution	7.3	20.1	23.51	1.03	2017	[174]
17	CH <sub>3</sub> NH <sub>3</sub> PbI <sub>3</sub>	spin-coating	16.2	17.3	22.51	1.04	2017	[175]
18	CH <sub>3</sub> NH <sub>3</sub> PbI <sub>3</sub>	spin-coating	8.9	12.3	18.1	0.88	2017	[176]
19	CH <sub>3</sub> NH <sub>3</sub> PbI <sub>3</sub>	screen printing	9.1	14.35	19.31	1.02	2017	[177]
20	CH <sub>3</sub> NH <sub>3</sub> PbI <sub>3-x</sub> Cl <sub>x</sub>	spin-coating	9.3	14	21.8	0.99	2016	[178]
21	CH <sub>3</sub> NH <sub>3</sub> PbI <sub>3-x</sub> Cl <sub>x</sub>	spin-coating	11.17	14.07	22.63	0.97	2016	[179]
22	CH <sub>3</sub> NH <sub>3</sub> PbI <sub>3</sub>	spin-coating	13.61	15.25	23.54	1.03	2016	[180]
23	CH <sub>3</sub> NH <sub>3</sub> PbI <sub>3</sub>	spin-coating	5.9	10.4	14.34	0.96	2016	[181]
24	(Pb(Ac) <sub>2</sub> )	spin-coating	12.05	17.6	20.7	1.00	2016	[182]
25	CH <sub>3</sub> NH <sub>3</sub> PbI <sub>3</sub>	one-step solution	14.26	18.32	22.34	1.00	2016	[183]
26	CH <sub>3</sub> NH <sub>3</sub> PbI <sub>3</sub>	-	15.6	17.4	22.76	1.02	2017	[184]
27	CH <sub>3</sub> NH <sub>3</sub> PbI <sub>3</sub>	Two-step interdiffusion	13.6	14.2	19.2	0.96	2016	[185]
28	CH <sub>3</sub> NH <sub>3</sub> PbI <sub>3-x</sub> Cl <sub>x</sub>	spin-coating	11.09	12.73	18.79	0.98	2015	[158]
29	CH <sub>3</sub> NH <sub>3</sub> PbI <sub>3</sub>	spin-coating	11.18	14.85	23.52	1.07	2016	[186]
30	CH <sub>3</sub> NH <sub>3</sub> PbI <sub>3-x</sub> Cl <sub>x</sub>	spin-coating	6.8	12.6	22.4	0.92	2016	[187]
31	CH <sub>3</sub> NH <sub>3</sub> PbI <sub>3</sub>	one-step spin coating	11.13	13.37	18.58	1.046	2015	[188]

point solvents are usually able to create more uniform crystal domains and smoother film surfaces due to slow solvent evaporation from the film allowed sufficient time for subsequent reaction of PbI<sub>2</sub> with MAI (TBP) to create crystalline perovskite. DMSO has also been reported to work well in a two-step processing method for the formation of improved morphology and crystallinity of the perovskite films. MAPbI<sub>3</sub> films in which the initial PbI<sub>2</sub> layer was deposited from DMSO rather than DMF were found to be comparatively smoother and contained more uniform sized grains with reduced PbI<sub>2</sub> residue than those prepared using DMF. The following paragraphs discuss the nature and effect of most common solvent additive in preparation of perovskite film.

**1-chloronaphthalene(CN):** Song et al, reported through UV-vis absorption spectra measurement that the absorbance of the CH<sub>3</sub>NH<sub>3</sub>PbI<sub>3-x</sub>Cl<sub>x</sub> film with CN additive is significantly higher than the pristine film and the absorption peak is red shifted by 30 nm, indicating the perovskite film with additive possess better crystal structures while SEM images of the films with additive showed the films were more smooth and homogenous with fewer pin-holes and voids as well as better surface coverage

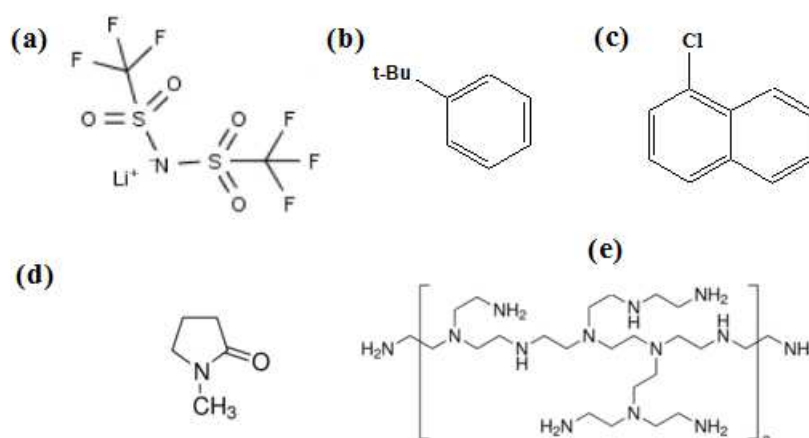


Fig. 3.21: Chemical structures of (a) (Li-TFSI), (b) TBP and (c) CN (d) Polyvinyl alcohol (e) polyethylenimine

than the pristine films[157]

**bis (trifluoromethane)sulfonimidelithiumsalt(Li-TFSI):** Spiro-MeOTAD alone in HTM is inadequate for attaining high PCEs because of its low conductivity and other problems. Lithium or cobalt salts are often used for p-doping to increase its hole concentration. Li-TFSI is normally used as a p-dopant to enhance the conductivity and hole mobility of the Spiro-OMeTAD for perovskite solar cells. Perovskite solar cells fabricated with spiro(TFSI)<sub>2</sub> showed improved operating stability in an inert atmosphere [157].

**4-tert-butylpyridine(TBP):** 4-tert-butylpyridine (TBP) is usually added into HTM to suppress charge recombination. It is also used to oxidize spiro-OMETAD. However, the oxidation process may have a negative effect on the stability of PSC.

Additives like LiTFSI and TBP functioned as p-dopant and morphology controller for the HTL. Y. Guo et al, reported that Li-TFSI and D-TBP could improve the short-circuit current density ( $J_{sc}$ ) and open-circuit voltage ( $V_{OC}$ ), respectively [136] They also improve the uniformity and conductivity of the HTL. The solvent for the inorganic HTM may also partly dissolve the perovskite, which may influence the stability of the cell. A typical example of the effect of additive solvent on the performance of perovskite solar cell has been demonstrated using DIO which enhances significantly, the device performance (Fig. 3.22) [158].

A detailed account of the effect of various additives and deposition methods on the overall performance of PSCs is given in Table 4.4.

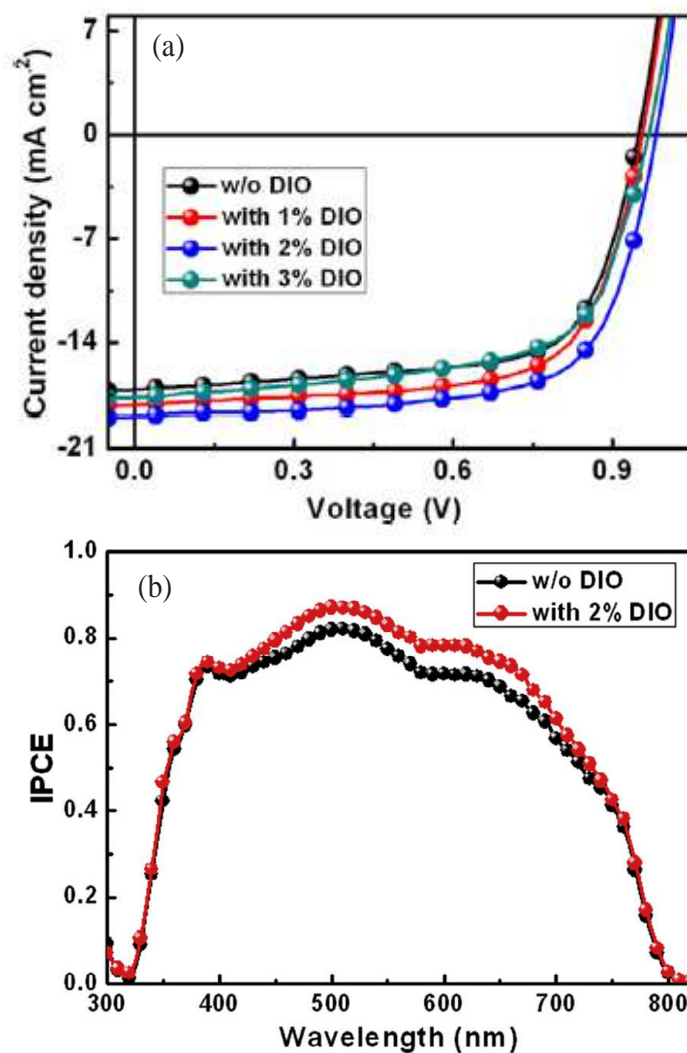


Fig. 3.22: The effect of DIO additive on the preparation of perovskite films (a) J-V curve taken from perovskite based solar cell at various concentration of DIO (b) External Quantum Efficiency (EQE) of the film with and with out DIO [159].

### 3.8 Conclusion

This review article provides a detailed account on the current status of perovskites based solar cells research and the progress made so far. It discusses on the existing new approaches in the synthesis of the perovskite and various methods of device preparations together with the changes observed in device performances. The review also highlighted the challenges facing the perovskite research as a solar absorbers to create better understanding that would assist in shaping new approaches. Organolead halide perovskite has attracted tremendous attention in recent years to serve as a solar absorber in the fabrication of thin film solar cells. Despite the rapid progress in attaining high power conversion efficiency in perovskite based solar cells

there are still numerous challenges in device stability, reproducibility of device fabrication, environmental friendliness, mass production of the devices amongst others [191, 192]. Perovskites solar absorbers suffer from intrinsic instability that resulted in fast degradation when exposed to water, oxygen, UV-light irradiation and high temperatures. It is a critical importance to protect the perovskite film from degrading agents to prolong its life time and make it feasible for large scale device fabrication. Capping the environmentally unstable perovskite film with ultra-thin layer of  $\text{Al}_2\text{O}_3$  has brought some success in increasing the life time of the devices. However, alternative charge transport layers and electrodes, interface engineering and encapsulation technologies need to be sought to address the problem. Iodide perovskite ( $\text{CH}_3\text{NH}_3\text{PbI}_3$ ) and bromide perovskite ( $\text{CH}_3\text{NH}_3\text{PbBr}_3$ ) are found to be the best photons harvesting medium in perovskite solar cells due to their high extinction coefficient and very good incident-photon-to-current conversion efficiency (IPCE). The energy bandgap of  $\text{CH}_3\text{NH}_3\text{PbI}_3$  is 1.55 eV which is close to the optimum bandgap (1.5 eV) for high PV performance [152]. Mixed halide perovskite such as  $\text{CH}_3\text{NH}_3\text{PbI}_{3-x}\text{Cl}_x$  are the most successful photoactive medium in the preparation of solar cells. Mixed halide offers the possibility to fine tune the energy band gap of the solar absorber as well as to improve the stability of the film. In addition to the standard  $\text{MAPbI}_3$  perovskite composition, researchers should seek interest in perovskites based on  $\text{HC}(\text{NH}_2)_2$  (or FA) or the mixture of FA and MAI. The use of solvent additives in the preparation of perovskite solar absorber received the necessary attention in order to bring about changes in device performances. The quality of the perovskite film is determined by its morphology and crystallinity which are a crucial factors in obtaining a high PCE. Additives integration in the perovskite solution process does not only improve the film morphology and crystallinity in terms surface coverage and roughness but also tune the optical and electrical properties of the perovskite photoactive layer. This results in lowering trap states and defect density in the perovskite film that would contribute to a longer carrier lifetime. Good crystallization and higher surface coverage increases the charge transport and inhibit charge recombination. A number of additives, such  $\text{NH}_4\text{Cl}$ , 1, 8-diiodooctane, 1-chloronaphthalene, polyvinylpyrrolidone, hydroiodic acid (HI) and hydrochloric acid have been reported to enhance charge carrier extraction at the interfaces between the perovskite and charge collection layers through high carrier mobility, improved light absorption, high charge generation and collection [164, 191]. Another

critical aspect of PSC research is the choice of suitable interfacial layers. Researchers have reported several results on the selection of various interfacial layers, but, there is often discrepancies in the reported values of PCE because of the device reproducibility problem. In general, both organic and inorganic materials have been used as interfacial buffer layers to facilitate the collection of charges from the photoactive medium to the corresponding electrodes. Among others, spiro-OMeTAD is the most successful HTM in the preparation of perovskite based solar cell. However, the high cost of the chemical and uncontrollable doping by O<sub>2</sub> calls for alternative materials as HTM [114, 146]. In general, there is a need to put concerted efforts towards alleviating environmental stability problem in the formation perovskite to achieve cost effective and flexible solar cells in the energy market. Therefore, device engineering and material development must be tailored towards roll-to-roll compatibility without sacrificing the device performance and stability.

## References

- [1] Cao, W. and J. Xue, Recent progress in organic photovoltaics: device architecture and optical design. *Energy & Environmental Science*, 2014. 7(7): p. 2123-2144.
- [2] Cui, J.; Yuan, H.; Li, J.; Xu, X.; Shen, Y.; Lin, H.; Wang, M., Recent progress in efficient hybrid lead halide perovskite solar cells. *Science and Technology of Advanced Materials*, 2016.
- [3] Kazim, S.; Nazeeruddin, M. K.; Gratzel, M.; Ahmad, S., Perovskite as light harvester: a game changer in photovoltaics. *Angewandte Chemie International Edition*, 2014. 53(11): p. 2812-2824.
- [4] Tong, X.; Lin, F.; Wu, J.; Wang, Z. M., High Performance Perovskite Solar Cells. *Advanced Science*, 2015
- [5] Jung, H.S. and N.G. Park, Perovskite solar cells: from materials to devices. *Small*, 2015. 11(1): p. 10-25.
- [6] Park, N.-G., Organometal perovskite light absorbers toward a 20 % efficiency low-cost solid-state mesoscopic solar cell. *The Journal of Physical Chemistry Letters*, 2013. 4(15): p. 2423-2429.
- [7] Chilvery, A. K.; Batra, A. K.; Yang, B.; Xiao, K.; Guggilla, P.; Aggarwal, M. D.; Surabhi, R.; Lal, R. B.; Currie, J. R.; Penn, B. G., Perovskites: transforming photovoltaics, a mini-review. *Journal of Photonics for Energy* 2015, 5 (1), 057402-057402.
- [8] Mahmood, K.; Swain, B. S.; Kirmani, A. R.; Amassian, A., Highly efficient perovskite solar cells based on a nanostructured WO<sub>3</sub>-TiO<sub>2</sub> core-shell electron transporting material. *Journal of Materials Chemistry A* 2015, 3 (17), 9051-9057.

- [9] Docampo, P.; Hanusch, F. C.; Giesbrecht, N.; Angloher, P.; Ivanova, A.; Bein, T., Influence of the orientation of methylammonium lead iodide perovskite crystals on solar cell performance. *APL Materials* 2014, 2 (8), 081508.
- [10] Ahn, N.; Son, D.-Y.; Jang, I.-H.; Kang, S. M.; Choi, M.; Park, N.-G., Highly reproducible perovskite solar cells with average efficiency of 18.3% and best efficiency of 19.7% fabricated via Lewis base adduct of lead (II) iodide. *Journal of the American Chemical Society* 2015, 137 (27), 8696-8699.
- [11] Zhou, H.; Chen, Q.; Li, G.; Luo, S.; Song, T.-b.; Duan, H.-S.; Hong, Z.; You, J.; Liu, Y.; Yang, Y., Interface engineering of highly efficient perovskite solar cells. *Science* 2014, 345 (6196), 542-546.
- [12] Son, D.-Y.; Lee, J.-W.; Choi, Y. J.; Jang, I.-H.; Lee, S.; Yoo, P. J.; Shin, H.; Ahn, N.; Choi, M.; Kim, D., Self-formed grain boundary healing layer for highly efficient CH<sub>3</sub>NH<sub>3</sub>PbI<sub>3</sub> perovskite solar cells. *Nature Energy* 2016, 1, 16081.
- [13] Green, M. A. and Ho-Baillie, A., Perovskite solar cells: The Birth of a New Era in Photovoltaics. *ACS Energy Letters* 2017, 2, 822-830.
- [14] Kojima, A.; Teshima, K.; Shirai, Y.; Miyasaka, T., Organometal halide perovskites as visible-light sensitizers for photovoltaic cells. *Journal of the American Chemical Society* 2009, 131 (17), 6050-6051.
- [15] Im, J.-H.; Lee, C.-R.; Lee, J.-W.; Park, S.-W.; Park, N.-G., 6.5% efficient perovskite quantum-dot-sensitized solar cell. *Nanoscale* 2011, 3 (10), 4088-4093.
- [16] Niu, G., X. Guo, and L. Wang, Review of recent progress in chemical stability of perovskite solar cells. *Journal of Materials Chemistry A*, 2015. 3(17): p. 8970-8980.
- [17] Campina, J.M., Perovskite Solar Cells: Rising, Last Advances, and Future Perspectives.
- [18] Fan, J., B. Jia, and M. Gu, Perovskite-based low-cost and high-efficiency hybrid halide solar cells. *Photonics Research*, 2014. 2(5): p. 111-120.
- [19] Burschka, J.; Pellet, N.; Moon, S.-J.; Humphry-Baker, R.; Gao, P.; Nazeeruddin, M. K.; Gratzel, M., Sequential deposition as a route to high-performance perovskite-sensitized solar cells. *Nature* 2013, 499 (7458), 316-319.

- [20] Noh, J. H.; Im, S. H.; Heo, J. H.; Mandal, T. N.; Seok, S. I., Chemical management for colorful, efficient, and stable inorganic/organic hybrid nanostructured solar cells. *Nano letters* 2013, 13 (4), 1764-1769.
- [21] Assadi, M. K.; Bakhoda, S.; Saidur, R.; Hanaei, H., Recent progress in perovskite solar cells. *Renewable and Sustainable Energy Reviews* 2017.
- [22] Tong, X.; Lin, F.; Wu, J.; Wang, Z. M., High performance perovskite solar cells. *Advanced Science* 2016, 3 (5).
- [23] Bhatt, M. D.; Lee, J. S., Current progress and scientific challenges in the advancement of organic-inorganic lead halide perovskite solar cells. *New Journal of Chemistry* 2017, 41 (19), 10508-10527.
- [24] Mehmood, U.; Al-Ahmed, A.; Afzaal, M.; Al-Sulaiman, F. A.; Daud, M., Recent progress and remaining challenges in organometallic halides based perovskite solar cells. *Renewable and Sustainable Energy Reviews* 2017, 78, 1-14.
- [25] NREL <https://www.nrel.gov/pv/>. (accessed 30/10/2017).
- [26] Chueh, C.-C.; Liao, C.-Y.; Zuo, F.; Williams, S. T.; Liang, P.-W.; Jen, A. K.-Y., The roles of alkyl halide additives in enhancing perovskite solar cell performance. *Journal of Materials Chemistry A* 2015, 3 (17), 9058-9062.
- [27] Zuo, C.; Ding, L., Bulk heterojunctions push the photoresponse of perovskite solar cells to 970 nm. *Journal of Materials Chemistry A* 2015, 3 (17), 9063-9066.
- [28] Bai, Y.; Yu, H.; Zhu, Z.; Jiang, K.; Zhang, T.; Zhao, N.; Yang, S.; Yan, H., High performance inverted structure perovskite solar cells based on a PCBM: polystyrene blend electron transport layer. *Journal of Materials Chemistry A* 2015, 3 (17), 9098-9102.
- [29] Wang, H.-H.; Chen, Q.; Zhou, H.; Song, L.; St Louis, Z.; De Marco, N.; Fang, Y.; Sun, P.; Song, T.-B.; Chen, H., Improving the TiO<sub>2</sub> electron transport layer in perovskite solar cells using acetylacetonate-based additives. *Journal of Materials Chemistry A* 2015, 3 (17), 9108-9115.

- [30] Chen, C. W.; Kang, H. W.; Hsiao, S. Y.; Yang, P. F.; Chiang, K. M.; Lin, H. W., Efficient and uniform planar-type perovskite solar cells by simple sequential vacuum deposition. *Advanced Materials* 2014, 26 (38), 6647-6652.
- [31] Wang, J. T.-W.; Ball, J. M.; Barea, E. M.; Abate, A.; Alexander-Webber, J. A.; Huang, J.; Saliba, M.; Mora-Sero, I. n.; Bisquert, J.; Snaith, H. J., Low-temperature processed electron collection layers of graphene/TiO<sub>2</sub> nanocomposites in thin film perovskite solar cells. *Nano letters* 2013, 14 (2), 724-730.
- [32] Ono, L. K.; Wang, S.; Kato, Y.; Raga, S. R.; Qi, Y., Fabrication of semi-transparent perovskite films with centimeter-scale superior uniformity by the hybrid deposition method. *Energy & Environmental Science* 2014, 7 (12), 3989-3993.
- [33] Wang, S.; Ono, L. K.; Leyden, M. R.; Kato, Y.; Raga, S. R.; Lee, M. V.; Qi, Y., Smooth perovskite thin films and efficient perovskite solar cells prepared by the hybrid deposition method. *Journal of Materials Chemistry A* 2015, 3 (28), 14631-14641.
- [34] Petrus, M.; Bein, T.; Dingemans, T.; Docampo, P., A low cost azomethine-based hole transporting material for perovskite photovoltaics. *J. Mater. Chem. A* 2015, 3 (23), 12159-12162.
- [35] He, J.; Chen, T., Additive regulated crystallization and film formation of CH<sub>3</sub>NH<sub>3</sub>PbI<sub>3-x</sub>Br<sub>x</sub> for highly efficient planar-heterojunction solar cells. *Journal of Materials Chemistry A* 2015, 3 (36), 18514-18520.
- [36] Bae, S.; Han, S. J.; Shin, T. J.; Jo, W. H., Two different mechanisms of CH<sub>3</sub>NH<sub>3</sub>PbI<sub>3</sub> film formation in one-step deposition and its effect on photovoltaic properties of OPV-type perovskite solar cells. *Journal of Materials Chemistry A* 2015, 3 (47), 23964-23972.
- [37] Gu, Z.; Zuo, L.; Larsen-Olsen, T. T.; Ye, T.; Wu, G.; Krebs, F. C.; Chen, H., Interfacial engineering of self-assembled monolayer modified semi-roll-to-roll planar heterojunction perovskite solar cells on flexible substrates. *Journal of Materials Chemistry A* 2015, 3 (48), 24254-24260.

- [38] Raga, S. R.; Jung, M.-C.; Lee, M. V.; Leyden, M. R.; Kato, Y.; Qi, Y., Influence of air annealing on high efficiency planar structure perovskite solar cells. *Chemistry of Materials* 2015, 27 (5), 1597-1603.
- [39] Dkhissi, Y.; Weerasinghe, H.; Meyer, S.; Benesperi, I.; Bach, U.; Spiccia, L.; Caruso, R. A.; Cheng, Y.-B., Parameters responsible for the degradation of CH<sub>3</sub>NH<sub>3</sub>PbI<sub>3</sub>-based solar cells on polymer substrates. *Nano Energy* 2016, 22, 211-222.
- [40] Tavakoli, M. M.; Gu, L.; Gao, Y.; Reckmeier, C.; He, J.; Rogach, A. L.; Yao, Y.; Fan, Z., Fabrication of efficient planar perovskite solar cells using a one-step chemical vapor deposition method. *Scientific reports* 2015, 5.
- [41] Zheng, X.; Chen, B.; Wu, C.; Priya, S., Room temperature fabrication of CH<sub>3</sub>NH<sub>3</sub>PbBr<sub>3</sub> by anti-solvent assisted crystallization approach for perovskite solar cells with fast response and small J-V hysteresis. *Nano Energy* 2015, 17, 269-278.
- [42] Huang, J.-h.; Jiang, K.-j.; Cui, X.-p.; Zhang, Q.-q.; Gao, M.; Su, M.-j.; Yang, L.-m.; Song, Y., Direct Conversion of CH<sub>3</sub>NH<sub>3</sub>PbI<sub>3</sub> from Electrodeposited PbO for Highly Efficient Planar Perovskite Solar Cells. *Scientific reports* 2015, 5.
- [43] Qiu, W.; Buffière, M.; Brammertz, G.; Paetzold, U. W.; Froyen, L.; Heremans, P.; Cheyns, D., High efficiency perovskite solar cells using a PCBM/ZnO double electron transport layer and a short air-aging step. *Organic Electronics* 2015, 26, 30-35.
- [44] Igbari, F.; Li, M.; Hu, Y.; Wang, Z.-K.; Liao, L.-S., A room-temperature CuAlO<sub>2</sub> hole interfacial layer for efficient and stable planar perovskite solar cells. *Journal of Materials Chemistry A* 2016, 4 (4), 1326-1335.
- [45] Yeo, J.-S.; Kang, R.; Lee, S.; Jeon, Y.-J.; Myoung, N.; Lee, C.-L.; Kim, D.-Y.; Yun, J.-M.; Seo, Y.-H.; Kim, S.-S., Highly efficient and stable planar perovskite solar cells with reduced graphene oxide nanosheets as electrode interlayer. *Nano Energy* 2015, 12, 96-104.
- [46] Razza, S.; Di Giacomo, F.; Matteocci, F.; Cinà, L.; Palma, A. L.; Casaluci, S.; Cameron, P.; D'epifanio, A.; Licocchia, S.; Reale, A., Perovskite solar cells and

- large area modules (100 cm<sup>2</sup>) based on an air flow-assisted PbI<sub>2</sub> blade coating deposition process. *Journal of Power Sources* 2015, 277, 286-291.
- [47] Zhang, H.; Qiao, X.; Shen, Y.; Moehl, T.; Zakeeruddin, S. M.; Grätzel, M.; Wang, M., Photovoltaic behaviour of lead methylammonium triiodide perovskite solar cells down to 80 K. *Journal of Materials Chemistry A* 2015, 3 (22), 11762-11767.
- [48] Cohen, B.-E.; Gamliel, S.; Etgar, L., Parameters influencing the deposition of methylammonium lead halide iodide in hole conductor free perovskite-based solar cells. *APL Materials* 2014, 2 (8), 081502.
- [49] Cao, D. H.; Stoumpos, C. C.; Malliakas, C. D.; Katz, M. J.; Farha, O. K.; Hupp, J. T.; Kanatzidis, M. G., Remnant PbI<sub>2</sub>, an unforeseen necessity in high-efficiency hybrid perovskite-based solar cells? a). *Apl Materials* 2014, 2 (9), 091101.
- [50] Abbas, H. A.; Kottokkaran, R.; Ganapathy, B.; Samiee, M.; Zhang, L.; Kitahara, A.; Noack, M.; Dalal, V. L., High efficiency sequentially vapor grown nip CH<sub>3</sub>NH<sub>3</sub>PbI<sub>3</sub> perovskite solar cells with undoped P3HT as p-type heterojunction layer. *APL Materials* 2015, 3 (1), 016105.
- [51] Liu, M.; Johnston, M. B.; Snaith, H. J., Efficient planar heterojunction perovskite solar cells by vapour deposition. *Nature* 2013, 501 (7467), 395-398.
- [52] Kim, H.-S.; Lee, C.-R.; Im, J.-H.; Lee, K.-B.; Moehl, T.; Marchioro, A.; Moon, S.-J.; Humphry-Baker, R.; Yum, J.-H.; Moser, J. E., Lead iodide perovskite sensitized all-solid-state submicron thin film mesoscopic solar cell with efficiency exceeding 9%. *Scientific reports* 2012, 2.
- [53] You, J.; Hong, Z.; Yang, Y. M.; Chen, Q.; Cai, M.; Song, T.-B.; Chen, C.-C.; Lu, S.; Liu, Y.; Zhou, H., Low-temperature solution-processed perovskite solar cells with high efficiency and flexibility. 2014.
- [54] Duan, J.; Wu, J.; Zhang, J.; Xu, Y.; Wang, H.; Gao, D.; Lund, P. D., TiO<sub>2</sub>/ZnO/TiO<sub>2</sub> sandwich multi-layer films as a hole-blocking layer for efficient perovskite solar cells. *International Journal of Energy Research* 2016.

- [55] Yadav, P.; Pandey, K.; Bhatt, P.; Raval, D.; Tripathi, B.; Pandey, M. K.; Kumar, M., Exploring the performance limiting parameters of perovskite solar cell through experimental analysis and device simulation. *Solar Energy* 2015, 122, 773-782.
- [56] Chen, L.-C.; Chen, C.-C.; Chen, J.-C.; Wu, C.-G., Annealing effects on high-performance CH<sub>3</sub>NH<sub>3</sub>PbI<sub>3</sub> perovskite solar cells prepared by solution-process. *Solar Energy* 2015, 122, 1047-1051.
- [57] Lee, M. M.; Teuscher, J.; Miyasaka, T.; Murakami, T. N.; Snaith, H. J., Efficient hybrid solar cells based on meso-superstructured organometal halide perovskites. *Science* 2012, 338 (6107), 643-647.
- [58] Liu, D.; Kelly, T. L., Perovskite solar cells with a planar heterojunction structure prepared using room-temperature solution processing techniques. *Nature photonics* 2014, 8 (2), 133-138.
- [59] Sum, T. C.; Mathews, N., Advancements in perovskite solar cells: photo-physics behind the photovoltaics. *Energy & Environmental Science* 2014, 7 (8), 2518-2534.
- [60] Yang, W. S.; Noh, J. H.; Jeon, N. J.; Kim, Y. C.; Ryu, S.; Seo, J.; Seok, S. I., High-performance photovoltaic perovskite layers fabricated through intramolecular exchange. *Science* 2015, 348 (6240), 1234-1237.
- [61] Ponseca Jr, C. S.; Savenije, T. J.; Abdellah, M.; Zheng, K.; Yartsev, A.; Pascher, T. r.; Harlang, T.; Chabera, P.; Pullerits, T.; Stepanov, A., Organometal halide perovskite solar cell materials rationalized: ultrafast charge generation, high and microsecond-long balanced mobilities, and slow recombination. *Journal of the American Chemical Society* 2014, 136 (14), 5189-5192.
- [62] Snaith, H. J.; Abate, A.; Ball, J. M.; Eperon, G. E.; Leijtens, T.; Noel, N. K.; Stranks, S. D.; Wang, J. T.-W.; Wojciechowski, K.; Zhang, W., Anomalous hysteresis in perovskite solar cells. *The journal of physical chemistry letters* 2014, 5 (9), 1511-1515.
- [63] Kazmerski, L. L., Solar photovoltaics R&D at the tipping point: A 2005 technology overview. *Journal of Electron Spectroscopy and Related Phenomena* 2006, 150 (2), 105-135.

- [64] Gaur, A.; Kumar, P., An improved circuit model for polymer solar cells. *Progress in Photovoltaics: Research and Applications* 2014, 22 (9), 937-948.
- [65] Qi, B.; Wang, J., Fill factor in organic solar cells. *Physical Chemistry Chemical Physics* 2013, 15 (23), 8972-8982.
- [66] Kirchartz, T.; Taretto, K.; Rau, U., Efficiency limits of organic bulk heterojunction solar cells. *The Journal of Physical Chemistry C* 2009, 113 (41), 17958-17966.
- [67] Jain, A.; Kapoor, A., A new approach to study organic solar cell using Lambert W-function. *Solar Energy Materials and Solar Cells* 2005, 86 (2), 197-205.
- [68] Hossain, N.; Das, S.; Alford, T. L., Equivalent Circuit Modification for Organic Solar Cells. *Circuits and Systems* 2015, 6 (06), 153.
- [69] Elumalai, N. K.; Uddin, A., Open circuit voltage of organic solar cells: an in-depth review. *Energy & Environmental Science* 2016.
- [70] Zhou, Z.; Pang, S.; Liu, Z.; Xu, H.; Cui, G., Interface engineering for high-performance perovskite hybrid solar cells. *Journal of Materials Chemistry A* 2015, 3 (38), 19205-19217.
- [71] Shi, S.; Li, Y.; Li, X.; Wang, H., Advancements in all-solid-state hybrid solar cells based on organometal halide perovskites. *Materials Horizons* 2015, 2 (4), 378-405.
- [72] Lee, J.-W.; Park, N.-G., Two-step deposition method for high-efficiency perovskite solar cells. *MRS Bulletin* 2015, 40 (08), 654-659.
- [73] Meng, L.; You, J.; Guo, T.-F.; Yang, Y., Recent Advances in the Inverted Planar Structure of Perovskite Solar Cells. *Accounts of chemical research* 2015.
- [74] Shi, J.; Luo, Y.; Wei, H.; Luo, J.; Dong, J.; Lv, S.; Xiao, J.; Xu, Y.; Zhu, L.; Xu, X., Modified two-step deposition method for high-efficiency TiO<sub>2</sub>/CH<sub>3</sub>NH<sub>3</sub>PbI<sub>3</sub> heterojunction solar cells. *ACS applied materials & interfaces* 2014, 6 (12), 9711-9718.
- [75] Brittman, S.; Adhyaksa, G. W. P.; Garnett, E. C., The expanding world of hybrid perovskites: materials properties and emerging applications. *MRS communications* 2015, 5 (01), 7-26.

- [76] Zhou, H.; Chen, Q.; Yang, Y., Vapor-assisted solution process for perovskite materials and solar cells. *MRS Bulletin* 2015, 40 (08), 667-673.
- [77] Pearson, A. J., Structure formation and evolution in semiconductor films for perovskite and organic photovoltaics. *Journal of Materials Research* 2017, 32 (10), 1798-1824.
- [78] Im, J.-H.; Jang, I.-H.; Pellet, N.; Grätzel, M.; Park, N.-G., Growth of CH<sub>3</sub>NH<sub>3</sub>PbI<sub>3</sub> cuboids with controlled size for high-efficiency perovskite solar cells. *Nature nanotechnology* 2014, 9 (11), 927-932.
- [79] Barrows, A. T.; Pearson, A. J.; Kwak, C. K.; Dunbar, A. D.; Buckley, A. R.; Lidzey, D. G., Efficient planar heterojunction mixed-halide perovskite solar cells deposited via spray-deposition. *Energy & Environmental Science* 2014, 7 (9), 2944-2950.
- [80] Chen, Q.; Zhou, H.; Hong, Z.; Luo, S.; Duan, H.-S.; Wang, H.-H.; Liu, Y.; Li, G.; Yang, Y., Planar heterojunction perovskite solar cells via vapor-assisted solution process. *J. Am. Chem. Soc* 2014, 136 (2), 622-625.
- [81] Hariz, A., Perspectives on organolead halide perovskite photovoltaics. *Journal of Photonics for Energy* 2016, 6 (3), 032001-032001.
- [82] Singh, S. P.; Nagarjuna, P., Organometal halide perovskites as useful materials in sensitized solar cells. *Dalton Transactions* 2014, 43 (14), 5247-5251.
- [83] Eperon, G. E.; Stranks, S. D.; Menelaou, C.; Johnston, M. B.; Herz, L. M.; Snaith, H. J., Formamidinium lead trihalide: a broadly tunable perovskite for efficient planar heterojunction solar cells. *Energy & Environmental Science* 2014, 7 (3), 982-988.
- [84] Saidaminov, M. I.; Abdelhady, A. L.; Murali, B.; Alarousu, E.; Burlakov, V. M.; Peng, W.; Dursun, I.; Wang, L.; He, Y.; Maculan, G., High-quality bulk hybrid perovskite single crystals within minutes by inverse temperature crystallization. *Nature communications* 2015, 6, 7586.
- [85] Song, Z.; Wathage, S. C.; Phillips, A. B.; Heben, M. J., Pathways toward high-performance perovskite solar cells: review of recent advances in organo-metal

- halide perovskites for photovoltaic applications. *Journal of Photonics for Energy* 2016, 6 (2), 022001-022001.
- [86] Green, M. A.; Ho-Baillie, A.; Snaith, H. J., The emergence of perovskite solar cells. *Nature Photonics* 2014, 8 (7), 506-514.
- [87] Shi, Y.; Xing, Y.; Li, Y.; Dong, Q.; Wang, K.; Du, Y.; Bai, X.; Wang, S.; Chen, Z.; Ma, T., CH<sub>3</sub>NH<sub>3</sub>PbI<sub>3</sub> and CH<sub>3</sub>NH<sub>3</sub>PbI<sub>3-x</sub>Cl<sub>x</sub> in Planar or Mesoporous Perovskite Solar Cells: Comprehensive Insight into the Dependence of Performance on Architecture. *The Journal of Physical Chemistry C* 2015, 119 (28), 15868-15873.
- [88] Yang, L.; Barrows, A. T.; Lidzey, D. G.; Wang, T., Recent progress and challenges of organometal halide perovskite solar cells. *Reports on Progress in Physics* 2016, 79 (2), 026501.
- [89] Yin, W.-J.; Yang, J.-H.; Kang, J.; Yan, Y.; Wei, S.-H., Halide perovskite materials for solar cells: a theoretical review. *Journal of Materials Chemistry A* 2015, 3 (17), 8926-8942.
- [90] Oku, T.; Suzuki, K.; Suzuki, A., Effects of chlorine addition to perovskite-type CH<sub>3</sub>NH<sub>3</sub>PbI<sub>3</sub> photovoltaic devices. *Journal of the Ceramic Society of Japan* 2016, 124 (3), 234-238.
- [91] Gao, P.; Grätzel, M.; Nazeeruddin, M. K., Organohalide lead perovskites for photovoltaic applications. *Energy & Environmental Science* 2014, 7 (8), 2448-2463.
- [92] Peng, W.; Wang, L.; Murali, B.; Ho, K. T.; Bera, A.; Cho, N.; Kang, C. F.; Burlakov, V. M.; Pan, J.; Sinatra, L., Solution-Grown Monocrystalline Hybrid Perovskite Films for Hole-Transporter-Free Solar Cells. *Advanced Materials* 2016, 28 (17), 3383-3390.
- [93] Dong, Q.; Song, J.; Fang, Y.; Shao, Y.; Ducharme, S.; Huang, J., Lateral-Structure Single-Crystal Hybrid Perovskite Solar Cells via Piezoelectric Poling. *Advanced Materials* 2016, 28 (14), 2816-2821.
- [94] Chen, H.; Zheng, X.; Li, Q.; Yang, Y.; Xiao, S.; Hu, C.; Bai, Y.; Zhang, T.; Wong, K. S.; Yang, S., An amorphous precursor route to the conformable oriented

- crystallization of  $\text{CH}_3\text{NH}_3\text{PbBr}_3$  in mesoporous scaffolds: toward efficient and thermally stable carbon-based perovskite solar cells. *Journal of Materials Chemistry A* 2016, 4 (33), 12897-12912.
- [95] Rao, H.-S.; Chen, B.-X.; Wang, X.-D.; Kuang, D.-B.; Su, C.-Y., A micron-scale laminar  $\text{MAPbBr}_3$  single crystal for an efficient and stable perovskite solar cell. *Chemical Communications* 2017, 53 (37), 5163-5166.
- [96] Liu, Y.; Zhang, Y.; Yang, Z.; Yang, D.; Ren, X.; Pang, L.; Liu, S. F., Thinness-and Shape-Controlled Growth for Ultrathin Single-Crystalline Perovskite Wafers for Mass Production of Superior Photoelectronic Devices. *Advanced Materials* 2016, 28 (41), 9204-9209.
- [97] Chen, Y.-X.; Ge, Q.-Q.; Shi, Y.; Liu, J.; Xue, D.-J.; Ma, J.-Y.; Ding, J.; Yan, H.-J.; Hu, J.-S.; Wan, L.-J., General space-confined on-substrate fabrication of thickness-adjustable hybrid perovskite single-crystalline thin films. *Journal of the American Chemical Society* 2016, 138 (50), 16196-16199.
- [98] Rao, H. S.; Li, W. G.; Chen, B. X.; Kuang, D. B.; Su, C. Y., In Situ Growth of  $120\text{ cm}^2$   $\text{CH}_3\text{NH}_3\text{PbBr}_3$  Perovskite Crystal Film on FTO Glass for Narrowband-Photodetectors. *Advanced Materials* 2017, 29 (16).
- [99] Baikie, T.; Fang, Y.; Kadro, J. M.; Schreyer, M.; Wei, F.; Mhaisalkar, S. G.; Graetzel, M.; White, T. J., Synthesis and crystal chemistry of the hybrid perovskite  $(\text{CH}_3\text{NH}_3)\text{PbI}_3$  for solid-state sensitised solar cell applications. *Journal of Materials Chemistry A* 2013, 1 (18), 5628-5641.
- [100] Oku, T., Crystal Structures of  $\text{CH}_3\text{NH}_3\text{PbI}_3$  and Related Perovskite Compounds Used for Solar Cells. 2015.
- [101] Quarti, C.; Mosconi, E.; Ball, J. M.; D'Innocenzo, V.; Tao, C.; Pathak, S.; Snaith, H. J.; Petrozza, A.; De Angelis, F., Structural and optical properties of methylammonium lead iodide across the tetragonal to cubic phase transition: implications for perovskite solar cells. *Energy & Environmental Science* 2016, 9 (1), 155-163.
- [102] Oku, T.; Zushi, M.; Imanishi, Y.; Suzuki, A.; Suzuki, K., Microstructures and photovoltaic properties of perovskite-type  $\text{CH}_3\text{NH}_3\text{PbI}_3$  compounds. *Applied Physics Express* 2014, 7 (12), 121601.

- [103] Eperon, G. E.; Burlakov, V. M.; Docampo, P.; Goriely, A.; Snaith, H. J., Morphological Control for High Performance, Solution-Processed Planar Heterojunction Perovskite Solar Cells. *Advanced Functional Materials* 2014, 24 (1), 151-157.
- [104] Song, T.-B.; Chen, Q.; Zhou, H.; Jiang, C.; Wang, H.-H.; Yang, Y. M.; Liu, Y.; You, J.; Yang, Y., Perovskite solar cells: film formation and properties. *Journal of Materials Chemistry A* 2015, 3 (17), 9032-9050.
- [105] Mali, S. S.; Hong, C. K., pin/nip type planar hybrid structure of highly efficient perovskite solar cells towards improved air stability: synthetic strategies and the role of p-type hole transport layer (HTL) and n-type electron transport layer (ETL) metal oxides. *Nanoscale* 2016.
- [106] Sessolo, M.; Momblona, C.; Gil-Escrig, L.; Bolink, H. J., Photovoltaic devices employing vacuum-deposited perovskite layers. *MRS Bulletin* 2015, 40 (08), 660-666.
- [107] Zuo, C.; Bolink, H. J.; Han, H.; Huang, J.; Cahen, D.; Ding, L., Advances in Perovskite Solar Cells. *Advanced Science* 2016.
- [108] Li, M.-H.; Shen, P.-S.; Wang, K.-C.; Guo, T.-F.; Chen, P., Inorganic p-type contact materials for perovskite-based solar cells. *Journal of Materials Chemistry A* 2015, 3 (17), 9011-9019.
- [109] Huang, L.; Hu, Z.; Xu, J.; Sun, X.; Du, Y.; Ni, J.; Cai, H.; Li, J.; Zhang, J., Efficient planar perovskite solar cells without a high temperature processed titanium dioxide electron transport layer. *Solar Energy Materials and Solar Cells* 2016, 149, 1-8.
- [110] Chen, L.-C.; Chen, J.-C.; Chen, C.-C.; Wu, C.-G., Fabrication and Properties of High-Efficiency Perovskite/PCBM Organic Solar Cells. *Nanoscale research letters* 2015, 10 (1), 1-5.
- [111] Yamamoto, K.; Kuwabara, T.; Takahashi, K.; Taima, T., Study of planar heterojunction perovskite photovoltaic cells using compact titanium oxide by chemical bath deposition. *Japanese Journal of Applied Physics* 2015, 54 (8S1), 08KF02.

- [112] Li, Y.; Meng, L.; Yang, Y. M.; Xu, G.; Hong, Z.; Chen, Q.; You, J.; Li, G.; Yang, Y.; Li, Y., High-efficiency robust perovskite solar cells on ultrathin flexible substrates. *Nature communications* 2016, 7.
- [113] Susrutha, B.; Giribabu, L.; Singh, S. P., Recent advances in flexible perovskite solar cells. *Chemical Communications* 2015, 51 (79), 14696-14707.
- [114] Yang, G.; Tao, H.; Qin, P.; Ke, W.; Fang, G., Recent progress in electron transport layers for efficient perovskite solar cells. *Journal of Materials Chemistry A* 2016, 4 (11), 3970-3990.
- [115] Salim, T.; Sun, S.; Abe, Y.; Krishna, A.; Grimsdale, A. C.; Lam, Y. M., Perovskite-based solar cells: impact of morphology and device architecture on device performance. *Journal of Materials Chemistry A* 2015, 3 (17), 8943-8969.
- [116] Aristidou, N.; Sanchez-Molina, I.; Chotchuangchutchaval, T.; Brown, M.; Martinez, L.; Rath, T.; Haque, S. A., The role of oxygen in the degradation of methylammonium lead trihalide perovskite photoactive layers. *Angewandte Chemie International Edition* 2015, 54 (28), 8208-8212.
- [117] Hailegnaw, B.; Kirmayer, S.; Edri, E.; Hodes, G.; Cahen, D., Rain on methylammonium lead iodide based perovskites: possible environmental effects of perovskite solar cells. *The journal of physical chemistry letters* 2015, 6 (9), 1543-1547.
- [118] Hoefler, S. F.; Trimmel, G.; Rath, T., Progress on lead-free metal halide perovskites for photovoltaic applications: a review. *Monatshefte für Chemie-Chemical Monthly* 2017, 1-32.
- [119] Babayigit, A.; Ethirajan, A.; Muller, M.; Conings, B., Toxicity of organometal halide perovskite solar cells. *Nature materials* 2016, 15, 247-251.
- [120] Wei, F.; Deng, Z.; Sun, S.; Xie, F.; Kieslich, G.; Evans, D. M.; Carpenter, M. A.; Bristowe, P. D.; Cheetham, A. K., The synthesis, structure and electronic properties of a lead-free hybrid inorganic-organic double perovskite (MA)<sub>2</sub>KBiCl<sub>6</sub> (MA= methylammonium). *Materials Horizons* 2016, 3 (4), 328-332.

- [121] McClure, E. T.; Ball, M. R.; Windl, W.; Woodward, P. M., Cs<sub>2</sub>AgBiX<sub>6</sub> (X= Br, Cl): new visible light absorbing, lead-free halide perovskite semiconductors. *Chemistry of Materials* 2016, 28 (5), 1348-1354.
- [122] Noel, N. K.; Stranks, S. D.; Abate, A.; Wehrenfennig, C.; Guarnera, S.; Haghighirad, A.-A.; Sadhanala, A.; Eperon, G. E.; Pathak, S. K.; Johnston, M. B., Lead-free organic–inorganic tin halide perovskites for photovoltaic applications. *Energy & Environmental Science* 2014, 7 (9), 3061-3068.
- [123] Li, Q.; Zhang, P.; Yao, L.; Deng, L.; Ren, X.; Li, Y., Recent Research Progress on Lead-free or Less-lead Perovskite Solar Cells. *Int. J. Electrochem. Sci* 2017, 12, 4915-4927.
- [124] Toshniwal, A.; Kheraj, V., Development of organic-inorganic tin halide perovskites: A review. *Solar Energy* 2017, 149, 54-59.
- [125] Mola, G. T.; Abera, N., Correlation between LUMO offset of donor/acceptor molecules to an open circuit voltage in bulk heterojunction solar cell. *Physica B: Condensed Matter* 2014, 445, 56-59.
- [126] Taleatu, B.; Omotoso, E.; Lal, C.; Makinde, W.; Ogundele, K.; Ajenifuja, E.; Lasisi, A.; Eleruja, M.; Mola, G., XPS and some surface characterizations of electrodeposited MgO nanostructure. *Surface and Interface Analysis* 2014, 46 (6), 372-377.
- [127] Oseni, S. O.; Mola, G. T., Properties of functional layers in inverted thin film organic solar cells. *Solar Energy Materials and Solar Cells* 2017, 160, 241-256.
- [128] Shi, Z.; Guo, J.; Chen, Y.; Li, Q.; Pan, Y.; Zhang, H.; Xia, Y.; Huang, W., Lead-free Organic–Inorganic Hybrid Perovskites for Photovoltaic Applications: Recent Advances and Perspectives. *Advanced Materials* 2017.
- [129] Hao, F.; Stoumpos, C. C.; Cao, D. H.; Chang, R. P.; Kanatzidis, M. G., Lead-free solid-state organic-inorganic halide perovskite solar cells. *Nature Photonics* 2014, 8 (6), 489-494.
- [130] Zhao, Z.; Gu, F.; Li, Y.; Sun, W.; Ye, S.; Rao, H.; Liu, Z.; Bian, Z.; Huang, C., Mixed-Organic-Cation Tin Iodide for Lead-Free Perovskite Solar Cells with an Efficiency of 8.12%. *Advanced Science* 2017.

- [131] Qiu, X.; Cao, B.; Yuan, S.; Chen, X.; Qiu, Z.; Jiang, Y.; Ye, Q.; Wang, H.; Zeng, H.; Liu, J., From unstable CsSnI<sub>3</sub> to air-stable Cs<sub>2</sub>SnI<sub>6</sub>: A lead-free perovskite solar cell light absorber with bandgap of 1.48 eV and high absorption coefficient. *Solar Energy Materials and Solar Cells* 2017, 159, 227-234.
- [132] Singh, P. K.; Singh, R.; Singh, V.; Bhattacharya, B.; Khan, Z. H., New class of lead free perovskite material for low-cost solar cell application. *Materials Research Bulletin* 2017.
- [133] Meyer, J.; Hamwi, S.; Kröger, M.; Kowalsky, W.; Riedl, T.; Kahn, A., Transition metal oxides for organic electronics: energetics, device physics and applications. *Advanced Materials* 2012, 24 (40), 5408-5427.
- [134] Elumalai, N. K.; Vijila, C.; Jose, R.; Uddin, A.; Ramakrishna, S., Metal oxide semiconducting interfacial layers for photovoltaic and photocatalytic applications. *Materials for Renewable and Sustainable Energy* 2015, 4 (3), 1-25.
- [135] Tao, C.; Ruan, S.; Xie, G.; Kong, X.; Shen, L.; Meng, F.; Liu, C.; Zhang, X.; Dong, W.; Chen, W., Role of tungsten oxide in inverted polymer solar cells. *Applied Physics Letters* 2009, 94 (4), 043311-1-043311-3.
- [136] Tan, Z. a.; Li, L.; Cui, C.; Ding, Y.; Xu, Q.; Li, S.; Qian, D.; Li, Y., Solution-processed tungsten oxide as an effective anode buffer layer for high-performance polymer solar cells. *The Journal of Physical Chemistry C* 2012, 116 (35), 18626-18632.
- [137] Christians, J. A.; Fung, R. C.; Kamat, P. V., An inorganic hole conductor for organo-lead halide perovskite solar cells. Improved hole conductivity with copper iodide. *Journal of the American Chemical Society* 2013, 136 (2), 758-764.
- [138] Qin, P.; Tanaka, S.; Ito, S.; Tetreault, N.; Manabe, K.; Nishino, H.; Nazeeruddin, M. K.; Grätzel, M., Inorganic hole conductor-based lead halide perovskite solar cells with 12.4% conversion efficiency. *Nature communications* 2014, 5.
- [139] Bakr, Z. H.; Wali, Q.; Fakharuddin, A.; Schmidt-Mende, L.; Brown, T. M.; Jose, R., Advances in hole transport materials engineering for stable and efficient perovskite solar cells. *Nano Energy* 2017, 34, 271-305.

- [140] Zhu, Z.; Bai, Y.; Zhang, T.; Liu, Z.; Long, X.; Wei, Z.; Wang, Z.; Zhang, L.; Wang, J.; Yan, F., High-Performance Hole-Extraction Layer of Sol-Gel-Processed NiO Nanocrystals for Inverted Planar Perovskite Solar Cells. *Angewandte Chemie* 2014, 126 (46), 12779-12783.
- [141] Cao, J.; Yu, H.; Zhou, S.; Qin, M.; Lau, T.-K.; Lu, X.; Zhao, N.; Wong, C.-P., Low-temperature solution-processed NiO x films for air-stable perovskite solar cells. *Journal of Materials Chemistry A* 2017, 5 (22), 11071-11077.
- [142] Chen, W.; Wu, Y.; Liu, J.; Qin, C.; Yang, X.; Islam, A.; Cheng, Y.-B.; Han, L., Hybrid interfacial layer leads to solid performance improvement of inverted perovskite solar cells. *Energy & Environmental Science* 2015, 8 (2), 629-640.
- [143] Meyer, J.; Zilberberg, K.; Riedl, T.; Kahn, A., Electronic structure of Vanadium pentoxide: An efficient hole injector for organic electronic materials. *Journal of Applied Physics* 2011, 110 (3), 033710.
- [144] Boix, P. P.; Larramona, G.; Jacob, A.; Delatouche, B.; Mora-Seró, I.; Bisquert, J., Hole transport and recombination in all-solid Sb2S3-sensitized TiO2 solar cells using CuSCN as hole transporter. *The Journal of Physical Chemistry C* 2011, 116 (1), 1579-1587.
- [145] Ameen, S.; Rub, M. A.; Kosa, S. A.; Alamry, K. A.; Akhtar, M. S.; Shin, H. S.; Seo, H. K.; Asiri, A. M.; Nazeeruddin, M. K., Perovskite solar cells: Influence of hole transporting materials on power conversion efficiency. *ChemSusChem* 2016, 9 (1), 10-27.
- [146] Shahbazi, M.; Wang, H., Progress in research on the stability of organometal perovskite solar cells. *Solar Energy* 2016, 123, 74-87.
- [147] Wang, D.; Wright, M.; Elumalai, N. K.; Uddin, A., Stability of perovskite solar cells. *Solar Energy Materials and Solar Cells* 2016, 147, 255-275.
- [148] Kim, J. H.; Liang, P. W.; Williams, S. T.; Cho, N.; Chueh, C. C.; Glaz, M. S.; Ginger, D. S.; Jen, A. K. Y., High-Performance and Environmentally Stable Planar Heterojunction Perovskite Solar Cells Based on a Solution-Processed Copper-Doped Nickel Oxide Hole-Transporting Layer. *Advanced Materials* 2015, 27 (4), 695-701.

- [149] Jeon, N. J.; Noh, J. H.; Yang, W. S.; Kim, Y. C.; Ryu, S.; Seo, J.; Seok, S. I., Compositional engineering of perovskite materials for high-performance solar cells. *Nature* 2015, 517 (7535), 476-480.
- [150] Dhingra, P.; Singh, P.; Rana, P. J. S.; Garg, A.; Kar, P., Hole-Transporting Materials for Perovskite-Sensitized Solar Cells. *Energy Technology* 2016.
- [151] Volker, S. F.; Collavini, S.; Delgado, J. L., Organic Charge Carriers for Perovskite Solar Cells. *ChemSusChem* 2015, 8 (18), 3012-3028.
- [152] Jeon, N. J.; Noh, J. H.; Kim, Y. C.; Yang, W. S.; Ryu, S.; Seok, S. I., Solvent engineering for high-performance inorganic-organic hybrid perovskite solar cells. *Nature materials* 2014, 13 (9), 897-903.
- [153] Yu, Y.; Gao, P., Development of electron and hole selective contact materials for perovskite solar cells. *Chinese Chemical Letters* 2017.
- [154] Liu, H.; Huang, Z.; Wei, S.; Zheng, L.; Xiao, L.; Gong, Q., Nano-structured electron transporting materials for perovskite solar cells. *Nanoscale* 2016.
- [155] Yin, Z.; Wei, J.; Zheng, Q., Interfacial Materials for Organic Solar Cells: Recent Advances and Perspectives. *Advanced Science* 2016.
- [156] Oseni, S. O.; Mola, G. T., The effect of uni-and binary solvent additives in PTB7: PC 61 BM based solar cells. *Solar Energy* 2017, 150, 66-72.
- [157] Song, X.; Wang, W.; Sun, P.; Ma, W.; Chen, Z.-K., Additive to regulate the perovskite crystal film growth in planar heterojunction solar cells. *Applied Physics Letters* 2015, 106 (3), 033901.
- [158] Liu, Z.; Lee, E.C., Solvent engineering of the electron transport layer using 1,8-diiodoctane for improving the performance of perovskite solar cells. *Organic Electronics* 2015, 24, 101-105.
- [159] Boopathi, K. M.; Mohan, R.; Huang, T.-Y.; Budiawan, W.; Lin, M.-Y.; Lee, C.-H.; Ho, K.-C.; Chu, C.-W., Synergistic improvements in stability and performance of lead iodide perovskite solar cells incorporating salt additives. *Journal of Materials Chemistry A* 2016, 4 (5), 1591-1597.

- [160] Li, L.; Chen, Y.; Liu, Z.; Chen, Q.; Wang, X.; Zhou, H., The Additive Coordination Effect on Hybrids Perovskite Crystallization and High-Performance Solar Cell. *Advanced Materials* 2016, 28 (44), 9862-9868.
- [161] Wang, Y.; Luo, J.; Nie, R.; Deng, X., Planar Perovskite Solar Cells using CH<sub>3</sub>NH<sub>3</sub>PbI<sub>3</sub> Films: A Simple Process Suitable for Large-Scale Production. *Energy Technology* 2016.
- [162] Wei, Q.; Yang, D.; Yang, Z.; Ren, X.; Liu, Y.; Feng, J.; Zhu, X.; Liu, S. F., Effective solvent-additive enhanced crystallization and coverage of absorber layers for high efficiency formamidinium perovskite solar cells. *RSC Advances* 2016, 6 (62), 56807-56811.
- [163] Li, X.; Dar, M. I.; Yi, C.; Luo, J.; Tschumi, M.; Zakeeruddin, S. M.; Nazeeruddin, M. K.; Han, H.; Gratzel, M., Improved performance and stability of perovskite solar cells by crystal crosslinking with alkylphosphonic acid  $\omega$ -ammonium chlorides. *Nature chemistry* 2015.
- [164] Shi, Y.; Wang, X.; Zhang, H.; Li, B.; Lu, H.; Ma, T.; Hao, C., Effects of 4-tert-butylpyridine on perovskite formation and performance of solution-processed perovskite solar cells. *Journal of Materials Chemistry A* 2015, 3 (44), 22191-22198.
- [165] Hsu, H.L.; Chang, C.C.; Chen, C.P.; Jiang, B.H.; Jeng, R.J.; Cheng, C.H., High-performance and high-durability perovskite photovoltaic devices prepared using ethylammonium iodide as an additive. *Journal of Materials Chemistry A* 2015, 3 (17), 9271-9277.
- [166] Heo, J. H.; Im, S. H., CH<sub>3</sub>NH<sub>3</sub>PbI<sub>3</sub>/poly-3-hexylthiophen perovskite mesoscopic solar cells: Performance enhancement by Li-assisted hole conduction. *physica status solidi (RRL) Rapid Research Letters* 2014, 8 (10), 816-821.
- [167] Zhang, Z.; Yue, X.; Wei, D.; Li, M.; Fu, P.; Xie, B.; Song, D.; Li, Y., DMSO-based PbI<sub>2</sub> precursor with PbCl<sub>2</sub> additive for highly efficient perovskite solar cells fabricated at low temperature. *RSC Advances* 2015, 5 (127), 104606-104611.
- [168] Franckevicius, M.; Mishra, A.; Kreuzer, F.; Luo, J.; Zakeeruddin, S. M.; Gratzel, M., A dopant-free spirobi[cyclopenta [2,1-b: 3,4-b] dithiophene]based hole-

- transport material for efficient perovskite solar cells. *Materials Horizons* 2015, 2 (6), 613-618.
- [169] Gong, X.; Li, M.; Shi, X. B.; Ma, H.; Wang, Z. K.; Liao, L. S., Controllable Perovskite Crystallization by Water Additive for High-Performance Solar Cells. *Advanced Functional Materials* 2015, 25 (42), 6671-6678.
- [170] Bi, H.; Zhang, Y., Influence of the additives in poly (3-hexylthiophene) hole transport layer on the performance of perovskite solar cells. *Materials Letters* 2015, 161, 767-769.
- [171] Shahbazi, S.; Tsai, C.-M.; Narra, S.; Wang, C.-Y.; Shiu, H.-S.; Afshar, S.; Taghavinia, N.; Diau, E. W.-G., Ag Doping of Organometal Lead Halide Perovskites: Morphology Modification and p-Type Character. *The Journal of Physical Chemistry C* 2017, 121 (7), 3673-3679.
- [172] Pham, N. D.; Tiong, V. T.; Chen, P.; Wang, L.; Wilson, G. J.; Bell, J.; Wang, H., Enhanced perovskite electronic properties via a modified lead (ii) chloride Lewis acid–base adduct and their effect in high-efficiency perovskite solar cells. *Journal of Materials Chemistry A* 2017, 5 (10), 5195-5203.
- [173] Sun, Y.; Wu, Y.; Fang, X.; Xu, L.; Ma, Z.; Lu, Y.; Zhang, W.-H.; Yu, Q.; Yuan, N.; Ding, J., Long-term stability of organic–inorganic hybrid perovskite solar cells with high efficiency under high humidity conditions. *Journal of Materials Chemistry A* 2017.
- [174] Mohamad, D.; Freestone, B.; Masters, R.; Reinhardt, M.; Canning, S.; Rodenburg, C.; Lidzey, D., Optimized organometal halide perovskite solar cell fabrication through control of nanoparticle crystal patterning. *Journal of Materials Chemistry C* 2017, 5 (9), 2352-2359.
- [175] Chiang, C.-H.; Nazeeruddin, M. K.; Gratzel, M.; Wu, C.-G., The synergistic effect of H<sub>2</sub>O and DMF towards stable and 20% efficiency inverted perovskite solar cells. *Energy & Environmental Science* 2017, 10 (3), 808-817.
- [176] Habisreutinger, S. N.; Noel, N. K.; Snaith, H. J.; Nicholas, R. J., Investigating the Role of 4-Tert Butylpyridine in Perovskite Solar Cells. *Advanced Energy Materials* 2017, 7 (1).

- [177] Xie, L.; Hwang, H.; Kim, M.; Kim, K., Ternary solvent for  $\text{CH}_3\text{NH}_3\text{PbI}_3$  perovskite films with uniform domain size. *Physical Chemistry Chemical Physics* 2017, 19 (2), 1143-1150.
- [178] Hou, X.; Hu, Y.; Liu, H.; Mei, A.; Li, X.; Duan, M.; Zhang, G.; Rong, Y.; Han, H., Effect of guanidinium on mesoscopic perovskite solar cells. *Journal of Materials Chemistry A* 2017, 5 (1), 73-78.
- [179] Chen, S.; Yu, X.; Cai, X.; Peng, M.; Yan, K.; Dong, B.; Hu, H.; Chen, B.; Gao, X.; Zou, D., PbCl<sub>2</sub>-assisted film formation for high-efficiency heterojunction perovskite solar cells. *RSC Advances* 2016, 6 (1), 648-655.
- [180] Dong, Q.; Wang, Z.; Zhang, K.; Yu, H.; Huang, P.; Liu, X.; Zhou, Y.; Chen, N.; Song, B., Easily accessible polymer additives for tuning the crystal-growth of perovskite thin-films for highly efficient solar cells. *Nanoscale* 2016, 8 (10), 5552-5558.
- [181] Lv, M.; Lv, W.; Fang, X.; Sun, P.; Lin, B.; Zhang, S.; Xu, X.; Ding, J.; Yuan, N., Performance enhancement of perovskite solar cells with a modified TiO<sub>2</sub> electron transport layer using Zn-based additives. *RSC Advances* 2016, 6 (41), 35044-35050.
- [182] Dong, S.; Wan, Y.; Wang, Y.; Yang, Y.; Wang, Y.; Zhang, X.; Cao, H.; Qin, W.; Yang, L.; Yao, C., Polyethylenimine as a dual functional additive for electron transporting layer in efficient solution processed planar heterojunction perovskite solar cells. *RSC Advances* 2016, 6 (63), 57793-57798.
- [183] Zhao, L.; Luo, D.; Wu, J.; Hu, Q.; Zhang, W.; Chen, K.; Liu, T.; Liu, Y.; Zhang, Y.; Liu, F., High-Performance Inverted Planar Heterojunction Perovskite Solar Cells Based on Lead Acetate Precursor with Efficiency Exceeding 18%. *Advanced Functional Materials* 2016, 26 (20), 3508-3514.
- [184] Ke, W.; Xiao, C.; Wang, C.; Saparov, B.; Duan, H. S.; Zhao, D.; Xiao, Z.; Schulz, P.; Harvey, S. P.; Liao, W., Employing lead thiocyanate additive to reduce the hysteresis and boost the fill factor of planar perovskite solar cells. *Advanced Materials* 2016, 28 (26), 5214-5221.

- [185] Bag, S.; Durstock, M. F., Large Perovskite Grain Growth in Low-Temperature Solution-Processed Planar pin Solar Cells by Sodium Addition. *ACS applied materials & interfaces* 2016, 8 (8), 5053-5057.
- [186] Mabrouk, S.; Dubey, A.; Zhang, W.; Adhikari, N.; Bahrami, B.; Hasan, M. N.; Yang, S.; Qiao, Q., Increased Efficiency for Perovskite Photovoltaics via Doping the  $\text{PbI}_2$  Layer. *The Journal of Physical Chemistry C* 2016, 120 (43), 24577-24582.
- [187] Wang, L.; Moghe, D.; Hafezian, S.; Chen, P.; Young, M.; Elinski, M.; Martinu, L.; Kena-Cohen, S. p.; Lunt, R. R., Alkali Metal Halide Salts as Interface Additives to Fabricate Hysteresis-Free Hybrid Perovskite-Based Photovoltaic Devices. *ACS Applied Materials & Interfaces* 2016, 8 (35), 23086-23094.
- [188] Xie, Y.; Shao, F.; Wang, Y.; Xu, T.; Wang, D.; Huang, F., Enhanced performance of perovskite  $\text{CH}_3\text{NH}_3\text{PbI}_3$  solar cell by using  $\text{CH}_3\text{NH}_3\text{I}$  as additive in sequential deposition. *ACS applied materials & interfaces* 2015, 7 (23), 12937-12942.
- [189] He, X.; Qiu, Y.; Yang, S., Fully-Inorganic Trihalide Perovskite Nanocrystals: A New Research Frontier of Optoelectronic Materials. *Advanced Materials* 2017.
- [190] Liu, T.; Chen, K.; Hu, Q.; Zhu, R.; Gong, Q., Inverted Perovskite Solar Cells: Progresses and Perspectives. *Advanced Energy Materials* 2016.
- [191] Li, X.; Dar, M. I.; Yi, C.; Luo, J.; Tschumi, M.; Zakeeruddin, S. M.; Nazeeruddin, M. K.; Han, H.; Gratzel, M., Improved performance and stability of perovskite solar cells by crystal crosslinking with alkylphosphonic acid  $\omega$  - ammonium chlorides. *Nature chemistry* 2015, 7 (9), 703-711.
- [192] Shaikh, J. S.; Shaikh, N. S.; Shaikh, A.; Mali, S. S.; Kale, A. J.; Kanjanaboosb, P.; Hong, C. K.; Kim, J.; Patil, P. S., Perovskite solar cells: In pursuit of efficiency and stability. *Materials & Design* 2017.
- [193] Yin, J.; Cao, J.; He, X.; Yuan, S.; Sun, S.; Li, J.; Zheng, N.; Lin, L., Improved stability of perovskite solar cells in ambient air by controlling the mesoporous layer. *Journal of Materials Chemistry A* 2015, 3 (32), 16860-16866.

## 4. METAL NANO-COMPOSITE CO-BUFFER LAYER FOR CHARGE CARRIERS COLLECTION IN PEROVSKITE SOLAR CELL

Journal of Physics and Chemistry of Solids xxx (2018) xxx-xxx



Contents lists available at ScienceDirect

Journal of Physics and Chemistry of Solids

journal homepage: [www.elsevier.com](http://www.elsevier.com)



### Metal nano-composite as charge transport co-buffer layer in perovskite based solar cell

Patrick Tonui, Ehadi Abdalla A. Arbab, Genene Tessema Mola\*

*School of Chemistry & Physics, University of KwaZulu-Natal, Pietermaritzburg Campus, Private Bag X01, Scottsville, 3209, South Africa*

#### ARTICLE INFO

#### ABSTRACT

Environmentally stable and uniform silver:zinc bimetallic nano-composites (BNCs) was synthesized by co-reduction of silver:zinc ions from silver and zinc nitrates. The synthesized nano-composites were employed at the various layers of the device structure in the preparation of thin film perovskite solar cell. Experimental evidences suggest that the nano-composite exhibited core-shell type structure which has important implication for surface plasmon resonance (SPR) absorption. It was found that enhanced photo-currents have been measured from solar cells by employing the Ag:Zn nano-particles as electron transport co-buffer layer. These resulted in improved power conversion efficiency and short current density by 26% and 53%, respectively. The information gathered from the optical measurements of the nano-particles suggest that significant quenches in photoluminescence (PL) intensity was measured from Ag:Zn composite compared to monometallic Ag and Zn nano-particles which is attributed to enhanced carrier density in bimetallic phases. Scanning and tunnelling electron spectroscopies (SEM and TEM) were employed to investigate morphology, crystallinity and elemental composition of the nano-particles.

### 4.1 Introduction

Despite achieving significant progress in power conversion efficiency (PCE) of perovskite-based solar cells, within a short period of time, the poor reproducibility, instability in ambient environment and the toxicity of lead remain major challenges for mass production. However, several progresses in the material design and various device architectures have contributed for the success of perovskite solar cell. Recently, metal nanocomposite materials have attracted a lot research attention because of their potential to enhance optical and electrical properties of perovskite thin films.

The composites possess exciting electronic, optical, catalytic or photocatalytic properties which are partly inherited from parent atoms [1–4]. Different metal nanoparticles, however, have a distinct influence on the formation of perovskite thin film due to their unique chemical and physical characteristics[5–7]. The metal nanocomposites exhibited surface plasmon resonance (SPR) absorption when dispersed in solar absorber thin film. The surface plasmon resonances are caused by collective oscillations of conduction electrons on the surface of nanocomposite excited by an electromagnetic fields of the incident wave[8, 9]. The specific oscillations depend on the particles' size and shape which resulted in different absorption and emission wavelenths. Because of such attractive features of plasmonic resonance phenomenon, metallic nanoparticles (NPs) can be incorporated either in the buffer layers or the active layers of organic photovoltaic (OPV) cells devices to assist in optical absorption and charge transport processes[10].

Furthermore, the metal-nanocompoisite can serve as efficient nucleation sites to enhance the formation of perovskite crystal structures and assists to achieve large crystal size. Electron exhibits shorter diffusion length in perovskite medium compared to that of the holes, hence, a mesoporous electron transport layer (ETL) is usually used to efficiently extract and transport electrons for high device performance [12]. A metal nanoparticles can have a similar influence on the charge transport properties of OPV which can be produced in different sizes and shapes. Metal nanoparticles can have spherical, tubular, or irregular shapes and can exist in fused, aggregated or agglomerated forms. Compared to other metal nanoparticles silver plasmonic resonance can be tuned to any wavelength in the visible spectrum and exhibits one of the highest efficiency of plasmon excitation. A single Ag nanoparticle can interact with light more effectively than any other metal nanoparticle with the same dimension comprised of either organic or inorganic chromophore [13]. Moreover, silver nanoparticles absorb much more light than is physically incident on them since its light-interaction cross-section is almost ten times more than that of the geometric cross-section[13, 14].

## 4.2 Materials and Methods

### 4.2.1 Synthesis of Ag:Zn Nanocomposite

The chemicals used in the synthesis of Ag:Zn nano-composite were obtained commercially and are used without further processing. Zinc nitrate hexahydrate ( $\text{Zn}(\text{NO}_3)_2 \cdot 6\text{H}_2\text{O}$ , purity 99.98%), silver nitrate ( $\text{AgNO}_3$ , 99.5%), Sodium borohydride ( $\text{NaBH}_4$ , 99.98%), chloroform, Dimethylformamide (DMF) and Isopropyl alcohol ( $\text{CH}_3\text{CHOHCH}_3$ ) were received from Sigma Aldrich. In general, Ag:Zn bimetallic nanoparticles were prepared by simultaneous reduction of two metal ions where a solution of  $\text{NaBH}_4$  was poured into the stirring mixture of zinc nitrate and silver nitrate solutions. The aqueous solution of Zinc nitrate (20 mM), silver nitrate (40 mM) and Sodium borohydride (0.1M) were separately prepared by dissolving in deionized water and stirred for one hour at room temperature. A 20 mL solution of  $\text{Zn}(\text{NO}_3)_2 \cdot 6\text{H}_2\text{O}$  and 50 mL of  $\text{NaBH}_4$  were then simultaneously poured drop wise into 20 mL of  $\text{AgNO}_3$  solution under continuous stirring for 20 minutes at room temperature. Excess of sodium borohydride was used both to reduce the Ag:Zn ions and stabilize the formed BNPs. The resulting mixture was then filtered, washed several times with deionized water and finally the precipitate left to dry at room temperature. The chemicals used for solar cell fabrication were also obtained from Ossila Ltd these are; Phenyl-C61-butyric acid methyl ester (PCBM), Lead iodide ( $\text{PbI}_2$ ), Methylammonium iodide (MAI 98%) and Poly(3,4-ethylenedioxythiophene)-poly(styrenesulfonate) (PEDOT: PSS).

### 4.2.2 Device fabrication

All the experiments were performed in ambient condition at a humidity level of about 28% and room temperature. The devices were fabricated on indium tin oxide (ITO) coated glass substrate with dimensions of 30 mm×30 mm. The ITO substrate was partially etched with acid solution then ultrasonically cleaned successively in detergents, deionized water, acetone, and isopropyl alcohol for 15 min, respectively. The substrates were then annealed at 120°C for 30 minutes. The precursor solutions were prepared separately where  $\text{CH}_3\text{NH}_3\text{I}$  was dissolved in 1 mL of 2-isopropanol and the lead iodide (0.5 M  $\text{PbI}_2$ ) solution was prepared in 0.5 mL DMF solvent at a concentration of 20 mg/mL, respectively. The solutions were placed under con-

stant magnetic stirring overnight at 60°C. The solar cell fabrication begins by spin coating PEDOT:PSS on dried ITO coated glass substrate at 3500 rpm and then annealed at 150°C. It is followed by PbI<sub>2</sub> and MAI at 2000 rpm respectively and annealed at 90°C for 5 minutes in nitrogen atmosphere. A thin layer of PCBM was spin coated at 1200 rpm for 40 s on the top perovskite and annealed at 90°C for 5 minutes. The samples are then transferred to vacuum deposition unit where a thin layer (0.5 nm) of Ag:Zn bimetallic nanoparticle was deposited on top of PCBM followed by 60 nm aluminium electrode at a base pressure of 10<sup>-6</sup> mbar. The device structure composed of various layers of materials is provided in Fig. 1. The fabricated

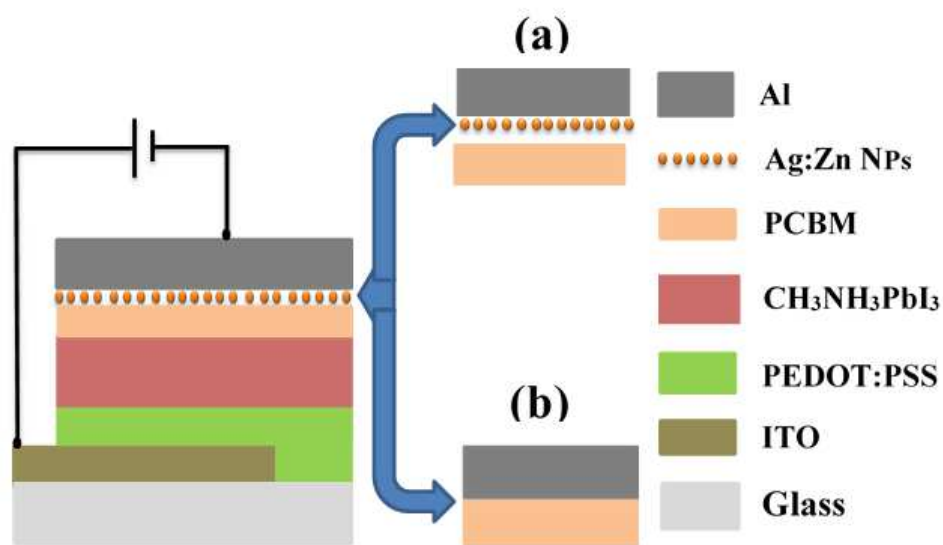


Fig. 4.1: Illustration of device structure of Psc

devices attains inverted planar-heterojunction solar cells with device architecture ITO/PEDOT: PSS/Perovskite/PCBM/Zn:Ag/Al. The current density-voltage characteristics of the devices were measured using a Keithley 2420 source meter under a simulated AM 1.5G solar irradiation at 100 mW/cm<sup>2</sup>. Photoluminescence(PL) and UV-vis spectra were measured with Rayleigh 1601 UV-vis spectrometer for optical characteristics. Zeiss high resolution scanning and tunnelling electron microscopy (HRSEM and HRTEM) as well as X-ray diffraction (XRD) analysis were used to study the perovskite morphologies and details of the synthesized nano-particles.

## 4.3 Results and Discussion

### 4.3.1 J-V Characteristics

Perovskite based solar cells were fabricated in planar and inverted structure using bi-metallic nano-composite co-buffer layer. Devices with architecture of ITO/PEDOT:PSS/perovskite with and without the addition of Ag:Zn NPs on top of PCBM were fabricated. Figures 2 displays the (J–V) curves of four OPV devies fabricated as pristine perovskite and the best three with the inclusion of Ag:Zn. A notable increase in the short-circuit current density ( $J_{SC}$ ) was observed from the devices that employed Ag:Zn buffer layer which resulted in enhancement in PCE, compared to the pristine device. However, significant lose in the device fill factor(FF) and open circuit voltage( $V_{OC}$ ) were recorded (see Fig 2 and tables II).

Tab. 4.1: Photovoltaic parameters of reference solar cells

Device	$V_{OC}$ V	$I_{SC}$ X $10^{-4}$ Amp	$J_{SC}$ $mA/cm^2$	FF %	PCE %
Diode 2	0.82	3.65	12.17	45.34	4.52
Diode 3	0.81	2.92	9.74	42.05	3.34
Diode 4	0.84	3.01	10.05	36.68	3.08
Diode 5	0.88	3.14	10.48	47.49	4.36

This could be attributed to the presence of Ag or Zn NPs that have acted as recombination centres or facilitate leakage currents [9]. A high energy difference between HOMO and LUMO is required to obtain a high  $V_{oc}$  while narrow bandgap is needed to maximize optical absorption. The slight decrease in  $V_{oc}$  could also be due to decrease on the energy difference between HOMO and LUMO of the photoactive medium brought about by Ag:Zn nanoparticles [15, 16]. According to the information provided in Tables I and II the values of  $J_{SC}$  was increased by almost a factor of two from each device fabricated with incorporation of Zn:Ag NPs co-buffer layer

Tab. 4.2: Solar cell parameters calculated from J-V curves measured by forward scanning.

Device	$V_{OC}$ V	$I_{SC}$ X $10^{-4}$ Amp	$J_{SC}$ $mA/cm^2$	FF %	PCE %
Diode 3	0.55	9.7	21.63	39.52	4.71
Diode 4	0.54	11.8	25.72	40.62	5.64
Diode 5	0.62	10.2	22.65	38.64	5.41
Diode 6	0.59	10.3	22.99	42.09	5.70

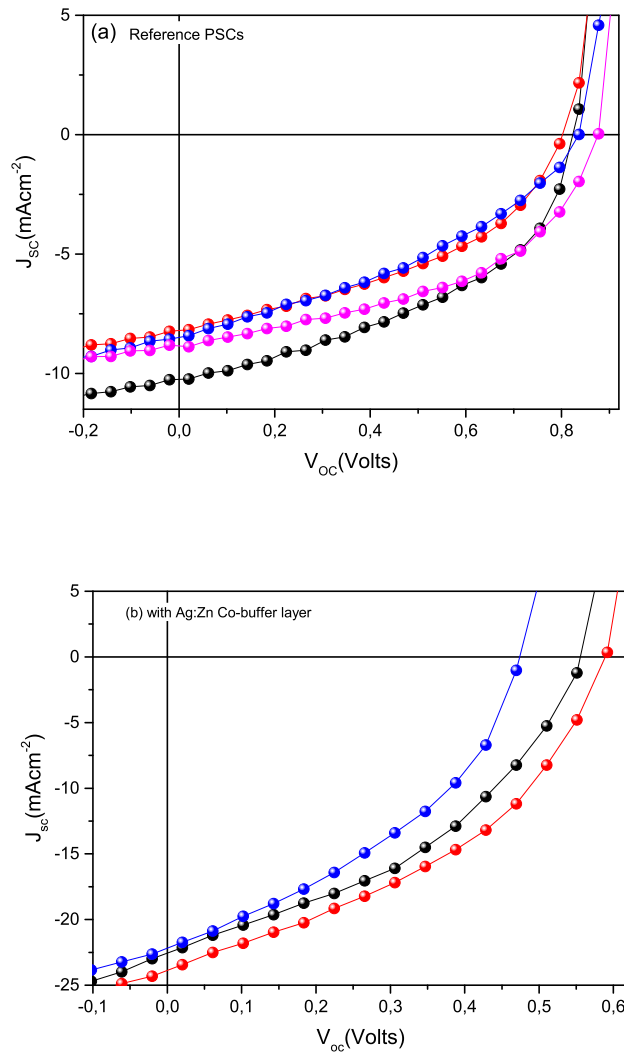


Fig. 4.2: J-V characteristic of perovskite based solar cells fabricated (a) with out metal nano-composite (b)with bimetallic nano-composite.

compared to those of reference cell. The range of the magnitude of the photocurrent from reference cell was  $9.7-12.2 \text{ mAcm}^{-2}$  while it was  $18.9-25.7 \text{ mAcm}^{-2}$  for those devices fabricated with Ag:Zn NPs. This is a clear indication of improved charge collection mechanisms together with enhanced absorption of the incident photons. As a consequence, there was an increase in PCE from 4.52% to 5.70% (26%). The increase in absorption band in the visible region was observed due to the influence from the local surface plasmon resonance (LSPR) absorption of Ag:Zn BNPs. Integration of silver:zinc bimetallic nanoparticles in perovskite fabrication as ETL led to the improvement in optical absorption both under UV and visible region indicated by red shift. Lu et al. reported that integration of mixed types of NPs improved PCE as a result LSPR-induced local field enhancement aiding charge separation and

transport, consequently increased charge carrier density and lifetime. BNPs display better optical absorption compared to single nanoparticles due to double resonance enhancement of two different nanoparticles [12, 16].

It shows incorporation of Ag:Zn BNPs between ETL and Al improves the average short-circuit current density by enhancing the charge separation and the trapping of electrons into the ETL layer at the PCBM/Al interface[15].

#### 4.3.2 Charge Transport Properties Analysis

The space-charge-limited current (SCLC) measured from the newly produced solar cell were used in the investigations of the charge transport process in the devices. The SCLCs have been taken from the current measured under dark condition. Assuming ohmic contact and trap free transport the J–V characteristics of the devices can be represented by the Mott–Gurney equation

$$J_{SCLC} = \frac{9}{8} \varepsilon_r \varepsilon_0 \mu_0 \frac{(V - V_{bi})^2}{L^3} \exp\left(\sqrt{\frac{V - V_{bi}}{L}}\right) \quad (4.1)$$

which may be expressed as

$$J = \frac{9}{8} \varepsilon_r \varepsilon_0 \mu \frac{V^2}{L^3} \quad (4.2)$$

where  $\varepsilon_r$  is the relative permittivity of the medium,  $\varepsilon_0$  is the permittivity of the vacuum,  $\mu_0$  is the mobility,  $V$  and  $V_{bi}$  are the applied and inbuilt voltages respectively and  $L$  is the thickness of the perovskite active layer.

$$V_{in} = V - V_{bi} - V_{sr} \quad (4.3)$$

Where,  $V$  is the applied voltage,  $V_{bi}$  is the built-in voltage and  $V_{sr}$  is the voltage dropped due to the series resistance. Mott–Gurney equation ignores the effect of diffusion, assumes current to be due to carriers of one polarity only and further assumes mobility independent of the field. The current density  $J$  vs  $V$  plots, illustrate three regions, the ohmic region where current increases linearly with the voltage at very low voltages, injection region where current increases exponentially with voltage and the SCLC region at higher voltages[18–23]. The mobility is a key parameter for perovskite solar cell materials since it affects the charge extraction and

Tab. 4.3: Charge transport parameter for the best four fabricated devices

Device	$\mu_0/\text{cm}^2\text{V}^{-1}\text{S}^{-1}$	$\gamma/(\text{cmV}^{-1})^{-\frac{1}{2}}$
reference	$4.598 \times 10^{-4}$	$-2.1 \times 10^{-4}$
1	$6.486 \times 10^{-3}$	$-9.2 \times 10^{-4}$
2	$1.842 \times 10^{-4}$	$-5.1 \times 10^{-4}$
3	$1.761 \times 10^{-4}$	$-1.6 \times 10^{-4}$
4	$1.528 \times 10^{-4}$	$-1.4 \times 10^{-4}$

recombination dynamics. Efficient determination of the electron and hole mobilities in perovskites is crucial. Efficient charge transport entails that the charges be able to travel from molecule to molecule but not be trapped or scattered. Therefore, charge carrier mobilities is influenced by many factors such as temperature, disorder, presence of impurities, electric field, molecular packing, charge-carrier density, size/molecular weight, and pressure. Charge mobilities can be determined experimentally by various methods which include Time-of-Flight (TOF), Space Charge Limited Current (SCLC), Charge Extraction by Linearly Increasing Voltage (CELIV) and Photo-CELIV Measurement etc[24]. The SCLC data taken from the dark currents were analysed in this investigation to determine the charge mobility. It was found that Ag:Zn NPs-doped device contains higher dark current density and mobilities compared to the reference (undoped) device (see Fig. 3 and Table III). Figure 5 illustrate best fit curves determined through SCLC method while Table 3 is extracted from Figure 3.

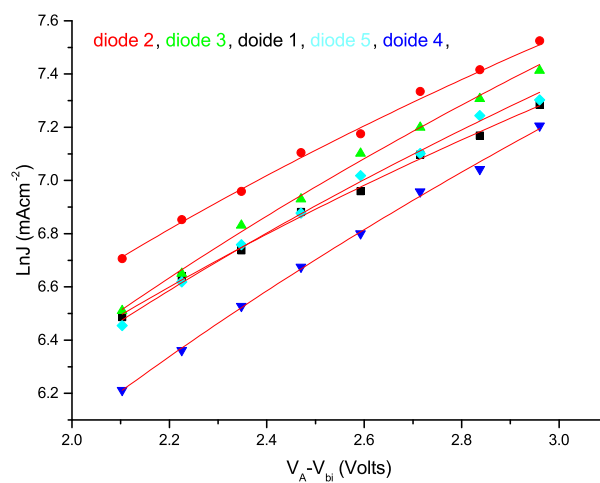


Fig. 4.3: Space charge limited current for the best 5 fabricated devices.

### 4.3.3 Photoluminescence Study

Figure 4.4 presents the photoluminescence spectra from both the silver and zinc nanoparticles. The observations show that both Silver and Zinc nanoparticles are found to enhance the luminescence of the UV band [25]. This is due to the increased number of excitons created and confirms that presence of the nanoparticles seems to quench the process of recombination. It is apparent that the perovskite film doped with Ag:Zn NPs on top of PCBM shows strong PL quenching compared to mono-metallic powders suggesting that the Ag:Zn NPs doping effectively enhanced the rate of carrier extraction at the ETL/perovskite interface. The PL results further support our findings from the (J–V) curves, that upon the addition of Ag:Zn NPs in the ETL, the  $J_{SC}$  was significantly enhanced due better hole extraction [17]. A rise in electron density of the particles results in a blue shift of SPR because the position and width of the SPR band which depends on the density of free electrons in the silver nanoparticles[26]. The synthesized Ag:Zn NPs are produced at different sized nanoparticles and clusters which can alter their surface energy bands due to interactions between the nanoparticles themselves. These results in the shift of energy band caused by spectral changes due to hybridization on the surface that leads to the formation of new surface energy bands. Absorption, rescattering and increase in grain size contribute to red shift of the maximum absorption wavelength[27, 28].

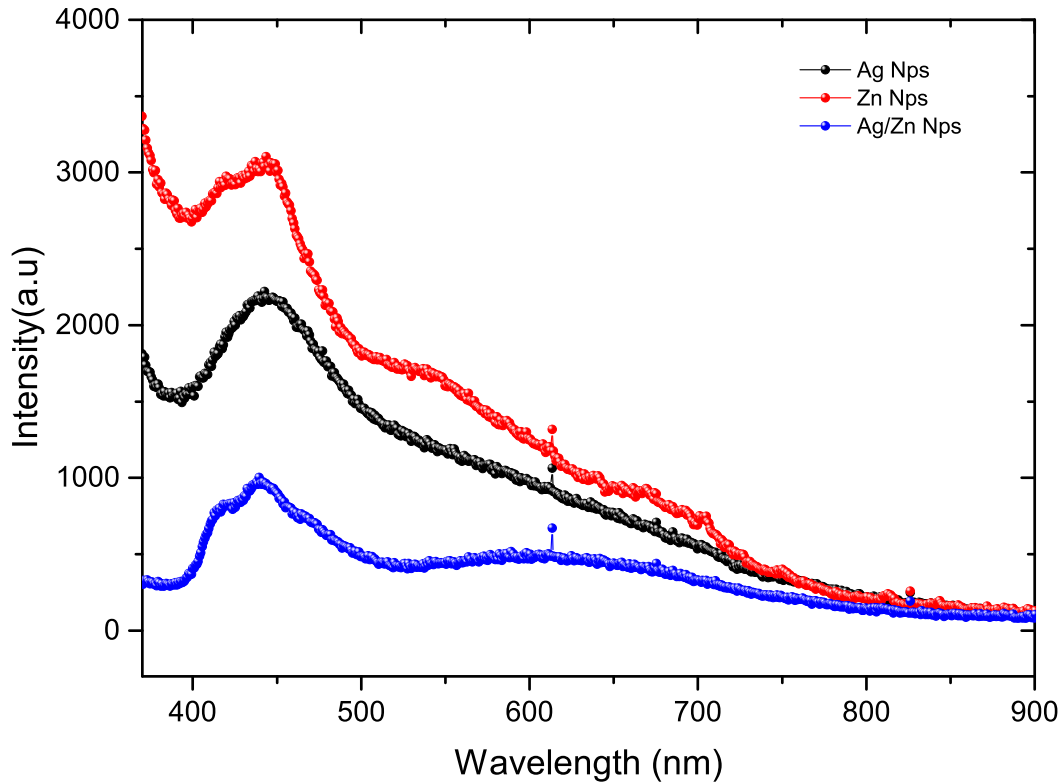


Fig. 4.4: Photoluminescence spectra of synthesized Zn, Ag and Ag:Zn BNCs.

#### 4.3.4 Optical Properties

The intensity of the absorption signal ranges between 400 and 900nm. Figure 4.5 shows the UV-vis absorption for both reference and device with Ag:Zn BNps indicating red shift in the whole range (a) more absorption and a bump appears on between 725-775nm then it start to decrease linearly up to visible region.

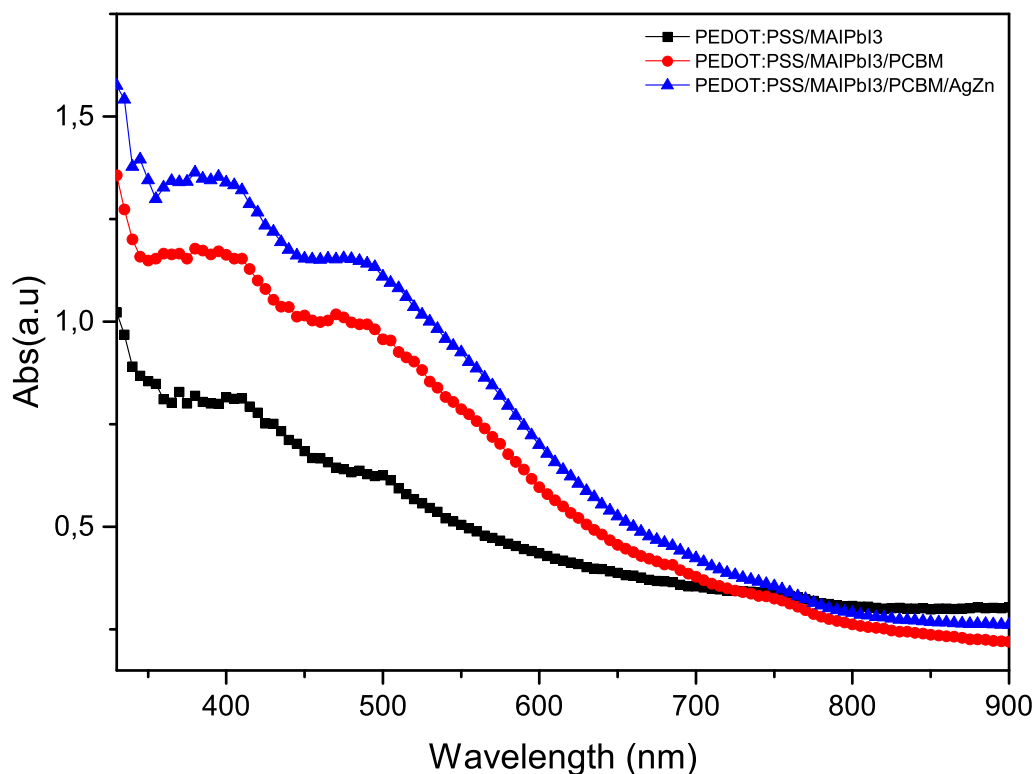


Fig. 4.5: U-V Absorbance of MAI,  $\text{PbI}_2$  and  $\text{PbMAI}_3$  solutions.

The increase in absorption band in the visible region was observed due to the influence from the surface plasmon resonance (SPR) absorption of Ag:Zn BNPs[25]. At resonance frequency, photon absorption and scattering were relatively enhanced since silver nanoparticles are efficient at absorbing and scattering light. When the frequency of incident light equals the natural frequency of free electrons oscillating against the restoring force of positive nuclei, the oscillation amplitude reaches a maximum. Maximum wavelength is therefore absorbed at resonant wavelength and resonant peak occurs at different wavelength for different metallic nanoparticles. As it is seen in figure 4.5, SPR wavelength between 400-500 nm which confirms the presence of silver nanoparticles in the fabricated device. In the UV region, the main absorption peaks of the Zn nanoparticles occurs between 370-380nm clearly observed that the absorption peaks showed a red shift which is in agreement with literatures and attributed to the size of the particles [26–35] (see Fig. 4.6). The band

gap was calculated by the Tauc's plot method (figure 4.6(inset)).

$$(\alpha h\nu)^2 = A(h\nu - E_g) \quad (4.4)$$

Where: A is a constant,  $E_g$  is the optical bandgap, h is Plank's constant, and  $\alpha$  is the absorption coefficient. The plot of  $(\alpha h\nu)^2$  versus  $h\nu$  for Ag:Zn nanoparticles is shown in Fig.7(inset). The optical bandgap of Ag:Zn nanoparticle was estimated through extrapolation of the linear portion of the  $(\alpha h\nu)^2$  versus  $h\nu$  plots. It was found to be approximately 1.677eV (figure 4.6(inset)).

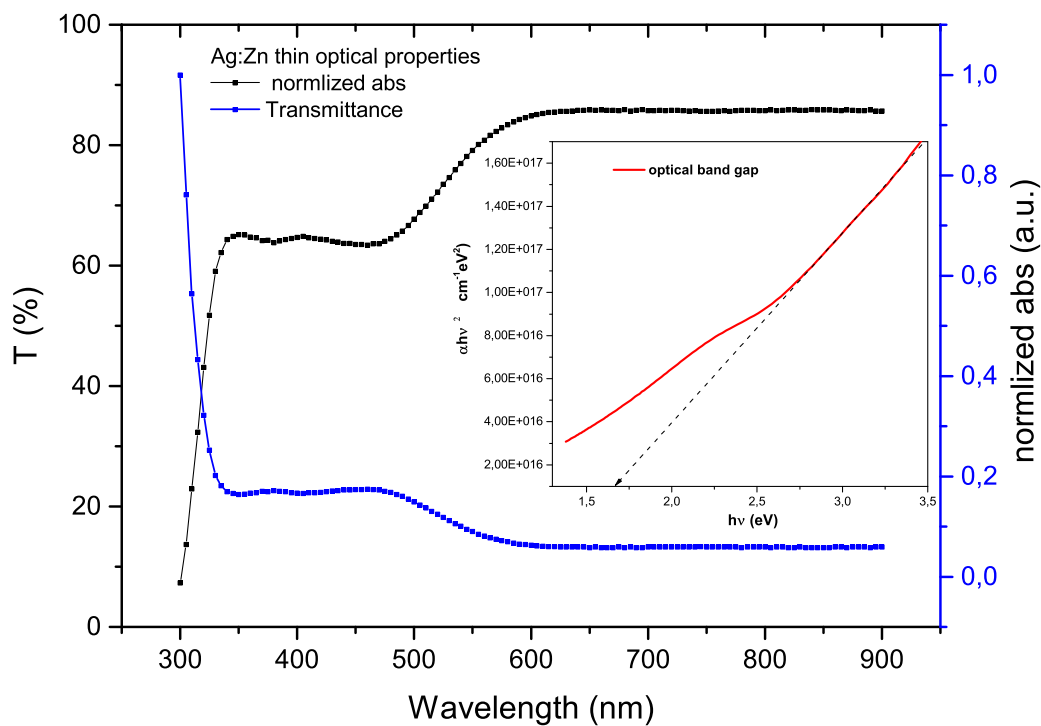


Fig. 4.6: Ag:Zn BNPs Absorbance, transmittance and optical bandgap (inset).

#### 4.3.5 Morphology

(SEM and TEM)

Figure 4.7 (a) and (b) show the microscopic structures of the synthesized metal nanoparticles in powder form. The SEM images contain various particle structures associated with Ag:Zn BNPs. The SEM micrographs consisted of uniform, spherical

core-shell Ag:Zn BNPs which are distinctly visible from each other consistent with that observed from the TEM images.

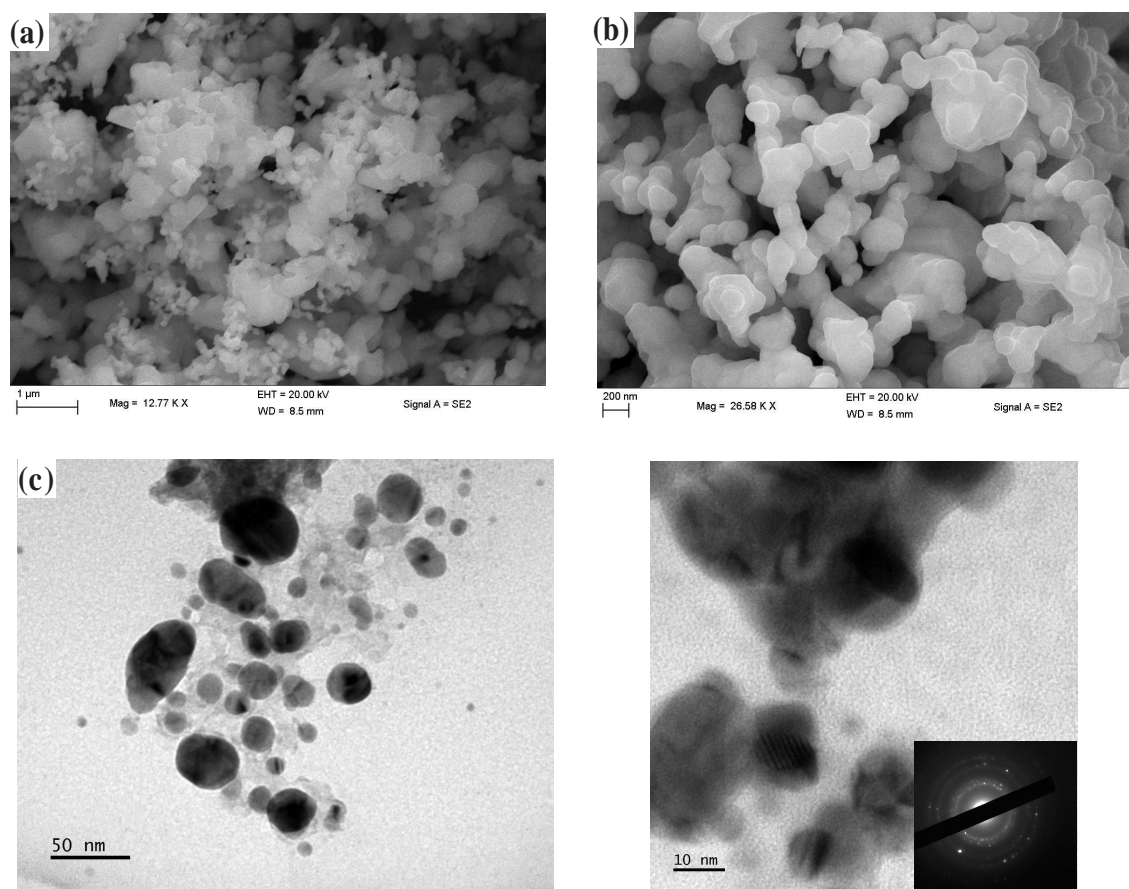


Fig. 4.7: SEM images of Ag:Zn NPs (a) and (b) TEM micrographs of Ag:Zn BNPs (c) and (d).

The results further indicated that the Zn NPs consist of fine tiny spherical and flower like shape nanoparticles. It is evident from the images that Ag NPs are non uniform dispersal clusters of spherical beadlike structure. The Ag:Zn NPs on the other hand seem to be slightly agglomerated. Furthermore, the TEM images provided in Fig. 7(c & d) have confirmed the formation of core-shell type structure. The average diameter of the nanoparticles was found approximately to be between (16 -27) nm (see table IV). TEM image also shows that the produced nanoparticles are more or less uniform in size and shape. High-resolution TEM images given in (Figure.7(d)) showed some form of regular pattern associated with their formation. The sizes of crystallites were in agreement with the calculated crystallite size as determined by the Scherer's equation discussed in section D and F. Energy dispersive X-ray spectra (EDX) measurements were carried out for device to detect the distribution of PCBM /Ag:Zn BNPs in perovskite film. The EDX spectrum confirms the presence of silver

(Ag), and zinc (Zn) in the powders of the bimetallic nanocomposite[28–31].

#### X-Ray Diffraction (XRD) Study

The XRD data provided patterns given in Figure 4.8, shows that the bimetallic nanocomposites were found to be crystalline and exhibited hexagonal wurtzite phase. It was noted that there was a decrease in intensity of the diffraction peaks of zinc nanoparticles while their FWHM increases on integration with silver nanoparticles see Table 4.4, indicating a decrease in crystallinity of the nanostructures. The substitution of  $\text{Zn}^{2+}$  ions by  $\text{Ag}^+$  ions in the Zinc crystal lattice sites results in a decrease of crystallinity and a shift in position of the main diffraction peaks as indicated in Table IV[23]. The XRD patterns as seen in Figure 4.8 displayed all the peaks for the (100), (002), (101), (102), (110), (103), (200), (112) and (201) corresponding to Zinc alongside those due to silver (111), (200),(220),(311) and (222) confirming their respective hexagonal and fcc structures.

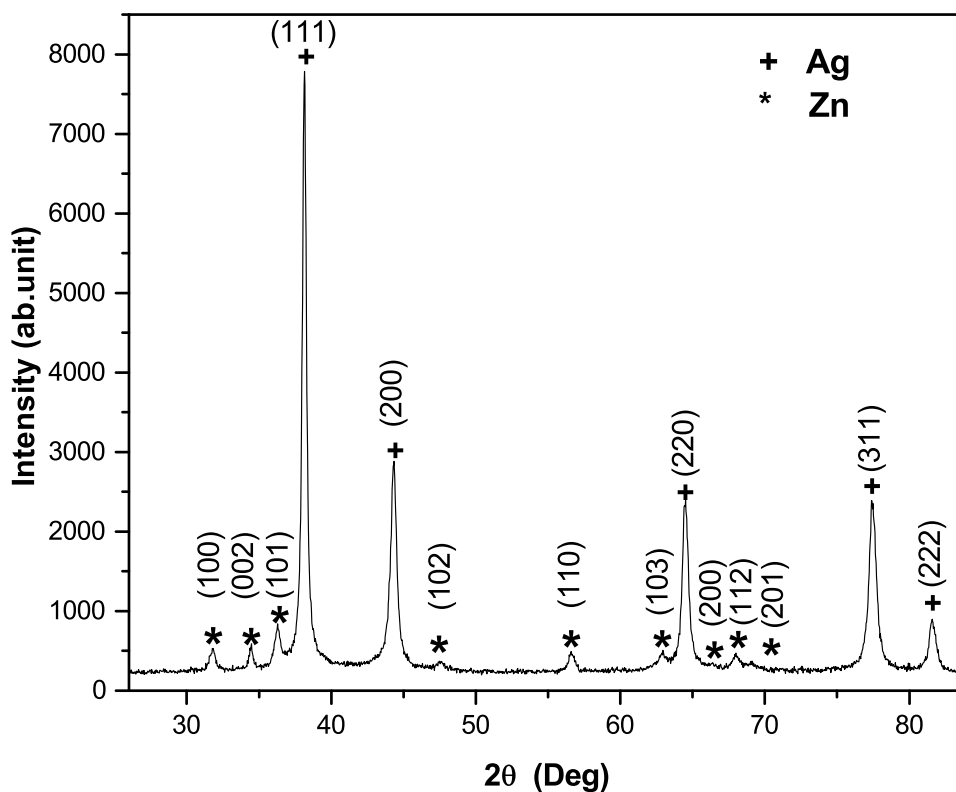


Fig. 4.8: X-Ray diffraction patterns of Ag:Zn BNCs.

Tab. 4.4: Analysis of XRD of Ag:Zn BNCs.

Peak No.	$2\theta$ (degree)	$h k l$	FWHM ( $\beta$ )	$d$ (nm)
1	38.14	(100)	0.383	22.93
2	38.12	(002)	0.317	27.70
3	38.14	(101)	0.383	22.93
4	38.14	(111)	0.385	22.81
5	44.31	(200)	0.553	16.21
6	64.48	(220)	0.503	19.51
7	77.45	(311)	0.585	18.18
8	81.59	(222)	0.423	25.91

The average crystallites size was determined through Full-width at Half Maximum (FWHM) of X-Ray diffraction peak by using Debye-Scherrer's equation as[33]

$$d = \frac{\kappa \lambda}{\beta \cos \theta} \quad (4.5)$$

Where:  $d$  is the average size of the crystallites,  $\lambda$  is the wavelength of radiation in radians ( $\text{CuK}\alpha = 1.5418\text{\AA}$ ),  $\beta$  is Full-width at Half Maxima (FWHM, in radians) and  $\theta$  is the peak position (in degrees). The grain size of the particles was calculated using the Debye Scherrer formula for the most intense peaks and the average calculated size of nanocomposites were between 16.21 nm to 27.70 nm. This broad size distribution could have been as a result of optical response introduced by multiple plasmon resonances. Table 4.4) gives a summary of the calculated results. Metal nanoparticles buffer layers lowers the work function to be closer or match with the LUMO energy level of the acceptor of the photoactive medium. This results in a decrease in the barrier level from the interfacial buffer layer to the cathode increasing charge collection. In addition having band gap higher than that of photoactive layer prevent the charge carrier recombination at the cathode electrode. During charge extraction from the photoactive medium, electron accumulate causing a shift in the Fermi level of the system to more negative potentials and closer to the conduction band of the semiconductor. This enables easy charge transfer between metal nanoparticles and the semiconductor. The smaller the size of the nanoparticles as it is observed in table IV the greater the shift in the Fermi level[38–41].

## 4.4 Conclusion

The influence of bimetallic nanocomposite was explored as co-electron transport buffer layer in perovskite solar cells. In this investigation, we have demonstrated that incorporation of Ag:Zn bimetallic nanoparticles in the preparation perovskite based solar cell led to improved device performance which mainly attributed to the local surface plasmon resonance of metal nanocomposite. The phenomenon has further caused red shift in the optical absorbance, that resulted in high photocurrent density which enhanced PCE from 4.52% to 5.70%. Therefore, the incorporation of bimetallic nanoparticles in perovskite based solar cells is promising strategy for improving both stability and PCE. The results can get better if controlled environments is used in the fabrication of the devices. On the other, hand the use of metal nanocomposite buffer layer can serve as capping material to contain the amount of toxic lead escaping into the environment. More needs to be done in optimization of the thickness and concentrations of both silver and zinc nanoparticles. This study thus reveals a new and cost-effective method for fabrication of solution processable thin film solar cells by employing metal nanocomposites.

## 4.5 Acknowledgments

This work is partially supported by National Research Foundation(NRF)(Grant numbers 92786 and 85589), South Africa.

## References

- [1] Thakur, U. K.; Kisslinger, R.; Shankar, K., One-dimensional electron transport layers for perovskite solar cells. *Nanomaterials* 2017, 7 (5), 95.
- [2] Hu, Z.; Dong, S.; Xue, Q.; Xu, R.; Yip, H.-L.; Huang, F.; Cao, Y., In-situ synthesis of metal nanoparticle-polymer composites and their application as efficient interfacial materials for both polymer and planar heterojunction perovskite solar cells. *Organic Electronics* 2015, 27, 46-52.
- [3] Hsu, H.-L.; Juang, T.-Y.; Chen, C.-P.; Hsieh, C.-M.; Yang, C.-C.; Huang, C.-L.; Jeng, R.-J., Enhanced efficiency of organic and perovskite photovoltaics from shape-dependent broadband plasmonic effects of silver nanoplates. *Solar Energy Materials and Solar Cells* 2015, 140, 224-231.
- [4] Carretero-Palacios, S.; Jiménez-Solano, A.; Míguez, H., Plasmonic nanoparticles as light-harvesting enhancers in perovskite solar cells: a user's guide. *ACS energy letters* 2016, 1 (1), 323-331.
- [5] Li, T.; Pan, Y.; Wang, Z.; Xia, Y.; Chen, Y.; Huang, W., Additive engineering for highly efficient organic–inorganic halide perovskite solar cells: recent advances and perspectives. *Journal of Materials Chemistry A* 2017.
- [6] Zaleska-Medynska, A.; Marchelek, M.; Diak, M.; Grabowska, E., Noble metal-based bimetallic nanoparticles: the effect of the structure on the optical, catalytic and photocatalytic properties. *Advances in colloid and interface science* 2016, 229, 80-107.
- [7] Sharma, G.; Kumar, A.; Sharma, S.; Naushad, M.; Dwivedi, R. P.; AlOthman, Z. A.; Mola, G. T., Novel development of nanoparticles to bimetallic nanoparticles and their composites: A review. *Journal of King Saud University-Science* 2017.
- [8] Liu, X.; Iocozzia, J.; Wang, Y.; Cui, X.; Chen, Y.; Zhao, S.; Li, Z.; Lin, Z., Noble metal–metal oxide nanohybrids with tailored nanostructures for efficient solar

- energy conversion, photocatalysis and environmental remediation. *Energy & Environmental Science* 2017, 10 (2), 402-434.
- [9] Liu, Y.; Lang, F.; Dittrich, T.; Steigert, A.; Fischer, C.-H.; Köhler, T.; Plate, P.; Rappich, J.; Lux-Steiner, M. C.; Schmid, M., Enhancement of photocurrent in an ultra-thin perovskite solar cell by Ag nanoparticles deposited at low temperature. *RSC Advances* 2017, 7 (3), 1206-1214.
- [10] Saheed O. Oseni and Genene Tessema Mola, Properties of functional layers in inverted thin film organic solar cells, *Solar Energy Materials & Solar Cells*, 160 (2017) 241–256
- [11] Tonui, P.; Oseni, S. O.; Sharma, G.; Yan, Q.; Mola, G. T., Perovskites photovoltaic solar cells: An overview of current status. *Renewable and Sustainable Energy Reviews* 2018, 91, 1025-1044.
- [12] Stratakis, E.; Kymakis, E., Nanoparticle-based plasmonic organic photovoltaic devices. *Materials Today* 2013, 16 (4), 133-146.
- [13] Evanoff, D. D.; Chumanov, G., Size-controlled synthesis of nanoparticles. 2. Measurement of extinction, scattering, and absorption cross sections. *The Journal of Physical Chemistry B* 2004, 108 (37), 13957-13962.
- [14] Kreibig, U.; Vollmer, M., *Optical properties of metal clusters*. Springer Science & Business Media: 2013; Vol. 25.
- [15] Guo, X.; Zhou, N.; Lou, S. J.; Smith, J.; Tice, D. B.; Hennek, J. W.; Ortiz, R. P.; Navarrete, J. T. L.; Li, S.; Strzalka, J., Polymer solar cells with enhanced fill factors. *Nature Photonics* 2013, 7 (10), 825.
- [16] Brabec, C. J.; Cravino, A.; Meissner, D.; Sariciftci, N. S.; Fromherz, T.; Rispen, M. T.; Sanchez, L.; Hummelen, J. C., Origin of the open circuit voltage of plastic solar cells. *Advanced Functional Materials* 2001, 11 (5), 374-380.
- [17] Kakavelakis, G.; Alexaki, K.; Stratakis, E.; Kymakis, E., Efficiency and stability enhancement of inverted perovskite solar cells via the addition of metal nanoparticles in the hole transport layer. *RSC Advances* 2017, 7 (21), 12998-13002.

- [18] Lu, L.; Luo, Z.; Xu, T.; Yu, L., Cooperative plasmonic effect of Ag and Au nanoparticles on enhancing performance of polymer solar cells. *Nano Letters* 2012, 13 (1), 59-64.
- [19] Ahn, S.; Jang, W.; Park, J. H.; Wang, D. H., Morphology fixing agent for [6, 6]-phenyl C 61-butyric acid methyl ester (PC 60 BM) in planar-type perovskite solar cells for enhanced stability. *RSC Advances* 2016, 6 (57), 51513-51519.
- [20] Kim, G.-W.; Shinde, D. V.; Park, T., Thickness of the hole transport layer in perovskite solar cells: performance versus reproducibility. *RSC Advances* 2015, 5 (120), 99356-99360.
- [21] Neumann, K.; Thelakkat, M., Perovskite solar cells involving poly (tetraphenylbenzidine) s: investigation of hole carrier mobility, doping effects and photovoltaic properties. *RSC Advances* 2014, 4 (82), 43550-43559.
- [22] Bell, J. T.; Mola, G. T., Improved charge transport in P3HT: PCBM bulk heterojunction PV cell under ambient environment. *Physica B: Condensed Matter* 2014, 437, 63-66.
- [23] Reid, O. G.; Munechika, K.; Ginger, D. S., Space charge limited current measurements on conjugated polymer films using conductive atomic force microscopy. *Nano letters* 2008, 8 (6), 1602-1609.
- [24] Xolani G. Mbuyise, Elhadi A.A. Arbab, K. Kaviyarasu, G. Pellicane, M. Maaza, Gene Tessema Mola, Zinc oxide doped single wall carbon nanotubes in hole transport buffer layer, *Journal of Alloys and Compounds* 706 (2017) 344-350
- [25] Deibel, C.; Dyakonov, V., Polymer? fullerene bulk heterojunction solar cells. *Reports on Progress in Physics* 2010, 73 (9), 096401.
- [26] Guidelli, E.; Baffa, O.; Clarke, D., Enhanced UV emission from silver/ZnO and gold/ZnO core-shell nanoparticles: photoluminescence, radioluminescence, and optically stimulated luminescence. *Scientific reports* 2015, 5, 14004.
- [27] Smitha, S.; Nissamudeen, K.; Philip, D.; Gopchandran, K., Studies on surface plasmon resonance and photoluminescence of silver nanoparticles. *Spectrochimica Acta Part A: Molecular and Biomolecular Spectroscopy* 2008, 71 (1), 186-190.

- [28] Zhang, A.; Zhang, J.; Fang, Y., Photoluminescence from colloidal silver nanoparticles. *Journal of Luminescence* 2008, 128 (10), 1635-1640.
- [29] B. A. Taleatu, E. Omotoso, C. Lal, W. O. Makind K. T. Ogundele, E. Ajenifuja, A. R. Lasisi, M. A. Eleruja and G. T. Mola, XPS and some surface characterizations of electrodeposited MgO nanostructure, *Surf. Interface Anal.*, 46, (2014 ), 372–377
- [30] M.V. Arularasu, M. Anbarasu, S. Poovaragan, R. Sundaram, K. Kanimozhi, C. Maria Magdalane, K. Kaviyarasu, F.T. Thema, D Letsholathebe, Genene T. Mola, M. Maaza, Structural, optical, morphological and microbial studies on SnO<sub>2</sub> nanoparticles prepared by co-precipitation method, *Journal of nanoscience and nanotechnology*, Vol. 8 (5), (2018), 3511-3517
- [31] Saoud, K.; Alsoubaihi, R.; Bensalah, N.; Bora, T.; Bertino, M.; Dutta, J., Synthesis of supported silver nano-spheres on zinc oxide nanorods for visible light photocatalytic applications. *Materials Research Bulletin* 2015, 63, 134-140.
- [32] Budhiraja, N.; Sharma, A.; Dahiya, S.; Parmar, R.; Vidyadharan, V., Synthesis and optical characteristics of silver nanoparticles on different substrates. *International Letters of Chemistry, Physics and Astronomy* 2013, 14, 80.
- [33] Gopinath, K.; Kumaraguru, S.; Bhakyaraj, K.; Mohan, S.; Venkatesh, K. S.; Esakkirajan, M.; Kaleeswarran, P.; Alharbi, N. S.; Kadaikunnan, S.; Govindarajan, M., Green synthesis of silver, gold and silver/gold bimetallic nanoparticles using the *Gloriosa superba* leaf extract and their antibacterial and antibiofilm activities. *Microbial pathogenesis* 2016, 101, 1-11.
- [34] Kumar, M.; Kojori, H. S.; Kim, S. J.; Park, H.-H.; Kim, J.; Yun, J.-H., Plasmonic effect-enhanced Ag nanodisk incorporated ZnO/Si metal–semiconductor–metal photodetectors. *Journal of Photonics for Energy* 2016, 6 (4), 042508-042508.
- [35] Islam, M. A.; Khan, I., ZnO/Ag Composite Nanoparticles for Surface Plasmon Resonance Based Sensor Application in UV-Vis Region. *International Journal Of Advancements in Research and Technology* 2012, 1 (1).
- [36] Kirkland, A. I.; Haigh, S. J., *Nanocharacterisation*. Royal Society of Chemistry: 2015.

- 
- [37] Michael, R. J. V.; Sambandam, B.; Muthukumar, T.; Umapathy, M. J.; Manoharan, P. T., Spectroscopic dimensions of silver nanoparticles and clusters in ZnO matrix and their role in bioinspired antifouling and photocatalysis. *Physical Chemistry Chemical Physics* 2014, 16 (18), 8541-8555.
- [38] Lai, T.-H.; Tsang, S.-W.; Manders, J. R.; Chen, S.; So, F., Properties of interlayer for organic photovoltaics. *Materials Today* 2013, 16 (11), 424-432.
- [39] Walker, B.; Choi, H.; Kim, J. Y., Interfacial engineering for highly efficient organic solar cells. *Current Applied Physics* 2017, 17 (3), 370-391.
- [40] Xiao, B.; Wu, H.; Cao, Y., Solution-processed cathode interfacial layer materials for high-efficiency polymer solar cells. *Materials Today* 2015, 18 (7), 385-394.
- [41] Ishii, H.; Sugiyama, K.; Ito, E.; Seki, K., Energy level alignment and interfacial electronic structures at organic/metal and organic/organic interfaces. *Advanced materials* 1999, 11 (8), 605-625.

## 5. EFFECT OF DUAL PLASMONIC RESONANCE ABSORPTION IN THIN FILM PEROVSKITE SOLAR CELL

### **Abstract**

Silver/Copper (Ag:Cu) nanocomposite were successfully synthesized from aqueous solutions of silver and copper nitrates by chemical reduction method. The nanocomposite is incorporated into Poly (3, 4-ethylenedioxythiophene): poly (styrene sulfonate) (PEDOT:PSS) hole transport layer with aim to improve the charge transport processes in perovskite based solar cell. The optical and morphological properties of the synthesized nano particles were studied using UV-Visible, X-ray diffraction (XRD), High Resolution Scanning and Electron microscopies (HRSEM and HRTEM), respectively. Substantial improvement on the measured photo-currents was observed from newly fabricated thin film perovskite solar cell which shows over 100% growth in the devices short circuit current ( $J_{sc}$ ) that resulted in 24% increase in power conversion efficiency (PCE). The loss in open circuit voltage and leakage current manifested in the magnitude of the fill factor of the devices are the major factors that prevents from attaining the full potential of the effect of the metal nano-particles in the hole transport layer (HTL).

### **5.1 Introduction**

The rapid population growth and industrialization has put researchers, industrialists and engineers at crossroads to search for alternative sources of renewable energy. It is an endeavour to meet the world's growing energy demand and mitigate overreliance on fossil fuels such as oil, coal and gas which has resulted in heavy global warming. Solar energy is one of the most abundant renewable energy source which is yet to be tapped sufficiently to curb the energy problems. Harvesting and

storing this clean source of energy requires new technologies to satisfy the ever increasing energy demand and reduce environmental pollution. One of the recently emerged solar cell technology is solution processable thin film perovskite solar cell which has attracted a great deal of attention. The power conversion efficiency of perovskite based solar cells has grown rapidly from 3.81% to 22.1% within a period of seven years [1, 2]. Some of the main advantages of the perovskite solar cell are its wide optical absorption band, tunability of the energy band gap, high charge carrier mobilities and power conversion efficiency. However, the stability of perovskite film under ambient environment and low reproducibility in device fabrication remain challenging. Though there is sufficient charge carrier diffusion length in perovskite medium the nature of the interfacing conditions between the active layer and the electrodes plays significant role in the charge collection process. The incorporation of metal nano-composite in PEDOT:PSS hole transport layer is expected to reduce charge recombination during charge carrier extraction and transport. The optical and electronic properties of the metal nanoparticles can be adjusted by controlling their size and constituents. Plasmonic metal nanoparticles are some of the strategies that have been employed to narrow the energy band gap of the solar absorber, enhance electron-hole charge separation and reduce charge recombination in semiconductor medium [5–7]. Metal nanoparticles can assist in improving optical absorption through light scattering due to the formation of local surface plasmon resonances (LSPR) effects resulting from metal surface electrons plasma [3, 7].

Different noble transition metal nanoparticles have been investigated for integration in various layers of the device structure in the preparation of thin film solar cells [8, 9]. Silver NPs have been incorporated with several transition metal semiconductor nanoparticles with different materials, shapes, sizes, concentrations and distributions to improve the properties and efficiency of the solar cells. Plasmonic nanoparticles have often been integrated in HTL buffer layer (PEDOT:PSS) to improve the conductivity of the polymer medium and assist the charge transport processes [5, 10–13]. The band gap of transition metal nanoparticles can be extended to include infrared region through proper tuning of preparation conditions, shape, size, refractive index, composition and structure of the nanoparticles [14]. In this work we synthesized Ag:Cu bimetallic nanocomposites (BNCs) in order to investigate their effect in PEDOT:PSS hole transport buffer layer in the preparations of

perovskite solar cell.

## 5.2 Materials and Methods

### 5.2.1 Synthesis of Ag:Cu Nanocomposite

Phenyl-C61-butyric acid methyl ester (PCBM), Lead iodide ( $\text{PbI}_2$ ), Methylammonium iodide (98% MAI) and Poly(3,4-ethylenedioxythiophene)-poly(styrenesulfonate) (PEDOT: PSS) were purchased from Ossila while Copper nitrate hydrate (99.999%  $\text{Cu}(\text{NO}_3)_2 \cdot \text{H}_2\text{O}$ ), silver nitrate (99.5%  $\text{AgNO}_3$ ), Sodium borohydride (99.98%  $\text{NaBH}_4$ ), chloroform, Dimethylformamide (DMF) and Isopropyl alcohol ( $\text{CH}_3\text{CHOHCH}_3$ ) were from Sigma Aldrich. Polyvinyl Pyrrolidone (PVP molecular weight 25000-30000), Merck, Germany) was used as the capping agent while ascorbic acid (99.5%, Associated Chemicals Enterprises, South Africa) and  $\text{NaBH}_4$  was used as the reducing agents. All the chemicals were of analytical grade and used as purchased without further purification. 5.0g of PVP and 1.75g of ascorbic acid are first separately dissolved in 50 mL of deionized water. Then the two solutions are mixed and stirred at  $60^\circ\text{C}$  for 10 minutes. 0.25 M of copper (II) nitrate, 0.1 M silver nitrate aqueous solutions were also separately prepared by dissolving in deionized water and stirred for one hour in ice bath for 0.3 M Sodium borohydride. 50 mL solution of  $\text{Cu}(\text{NO}_3)_2 \cdot \text{H}_2\text{O}$  and 50 mL of  $\text{AgNO}_3$  were then simultaneously poured dropwise into 50 mL of  $\text{NaBH}_4$  solution with continued stirring for 20 minutes at room temperature. The obtained mixture were separated by centrifugation at 5000 rpm for 30 minutes, filtered, washed several times with deionized water and finally the precipitate left to dry at room temperature.

### 5.2.2 Device fabrication

All the experiments were performed in ambient condition with a humidity level of about 28% at room temperature. The devices were fabricated on an indium tin oxide (ITO) coated glass substrate with dimensions of 30 mm×30mm. The ITO substrate was partially etched with acid solution then ultrasonically cleaned successively in detergents, deionized water, acetone, and isopropyl alcohol for 15 min, respectively. It was then annealed at  $120^\circ\text{C}$  for 30 minutes. The precursor solutions were pre-

pared separately where  $\text{CH}_3\text{NH}_3\text{I}$  was dissolved in 1 mL of 2-isopropanol and the lead iodide solution was formed from 0.5 M  $\text{PbI}_2$  in 0.5 mL DMF solvent at a concentration of 20 mg/mL, respectively. The solutions were under constant magnetic stirring overnight at  $60^\circ\text{C}$ . The solar cell fabrication begins by spin coating PEDOT:PSS mixed with 0.7% of Ag:Cu nanocomposites on dried ITO coated glass substrate at 3500 rpm and then annealed at  $150^\circ\text{C}$ . It is followed by  $\text{PbI}_2$  and MAI at 2000 rpm respectively and annealed at  $90^\circ\text{C}$  for 5 minutes in nitrogen atmosphere. A thin layer of PCBM was spin coated at 1200 rpm for 40 s on the top of perovskite and annealed at  $90^\circ\text{C}$  for 5 minutes. The samples are then transferred vacuum deposition unit where 60 nm aluminium electrode was deposited at a base pressure of  $10^{-6}$ . The device structure illustrating various layers of materials is provided in Fig. 5.1. The fabricated devices attains inverted planar-heterojunction solar cells with device architecture ITO/PEDOT:PSS/ Ag:Cu/perovskite/PCBM//Al. The current density-voltage characteristics of the devices were measured using a Keithley 2420 source meter under a simulated AM 1.5G solar irradiation at  $100 \text{ mW}/\text{cm}^2$ . The active area was approximately  $0.03 \text{ cm}^2$ . UV-Vis spectra were measured with Rayleigh 1601 UV-Vis spectrometer for structural characterization. Zeiss high resolution scanning and tunnelling electron microscopy (HRSEM and HRTEM) as well as X-ray diffraction analysis were used to study the perovskite morphologies and details of the synthesized nanoparticles.

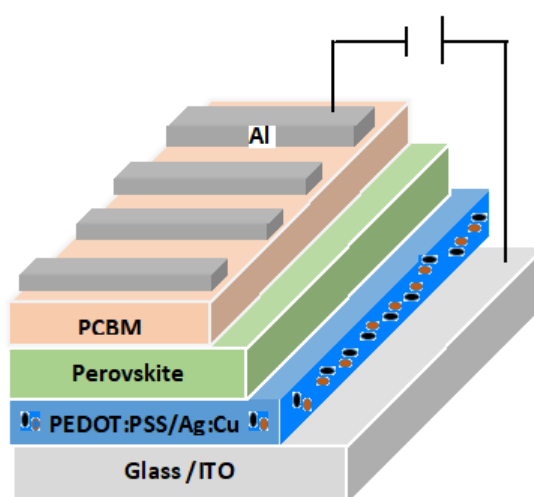


Fig. 5.1: Illustration of device structure of Psc.

## 5.3 Results and Discussion

### 5.3.1 J-V Characteristics

Thin film Perovskite solar cells are fabricated with and without the inclusion of Ag:Cu nano-composite in PEDOT:PSS hole transport layer. The current-voltage characteristics measured from the newly fabricated devices are given in Fig. 5.2 where the top panel is taken from devices without Ag:Cu in HTL while the bottom panel are from metal-nano-composite doped HTL. According to the result provided in Table 5.1 and 5.2 the devices doped with Ag:Cu nano-composite exhibited low fill factor an indication of leakage current due to the presence of the metal nano-particles. However, we observed that significant enhancement in the measured photocurrent where the magnitude of the short circuit current almost doubled compared to the pristine hole transport layer. This is attributed to the effect of the metal nano-particles in the process of charge extraction. Tables 5.1 and 5.2 illustrates summary results from the solar cell parameters taken under ambient environment. According to the data provided in the tables the power conversion efficiency of the solar cell increased from from 5.05% to 6.28% mainly from enhanced current density ( $J_{sc}$ ). However, the devices fabricated with metal nano-particles exhibited significant loss in open circuit voltage and fill factors which are attributed to interfacial conditions such as mismatch between the energy levels, short circuiting and leakage current.

Tab. 5.1: J-V characteristic curves of reference solar cell without BNCs.

Device	$V_{OC}$ V	$I_{SC}$ X $10^{-4}$ Amp	$J_{SC}$ $mA/cm^2$	FF %	PCE %
without					
Diode 2	0.84	3.75	12.50	48.29	5.05
Diode 3	0.83	3.32	11.08	44.72	4.13
Diode 4	0.85	3.04	10.13	37.60	3.23
Diode 5	0.86	3.00	10.00	48.47	4.19
with Ag:Cu					
Diode 3	0.63	17.6	29.30	31.53	5.84
Diode 4	0.67	15.2	25.33	30.93	5.24
Diode 5	0.67	17.4	28.97	32.16	6.28
Diode 6	0.67	14.6	24.38	32.13	5.28

The improved collection of photo-current could be associated with enlarged active layer/PEDOT: PSS interfacial area and improved PEDOT: PSS conductivity due to alteration in the morphology of the PEDOT:PSS and metal nano-particles blend[15]. The reduction in  $V_{oc}$  can be attributed to larger interface area introduced by increase

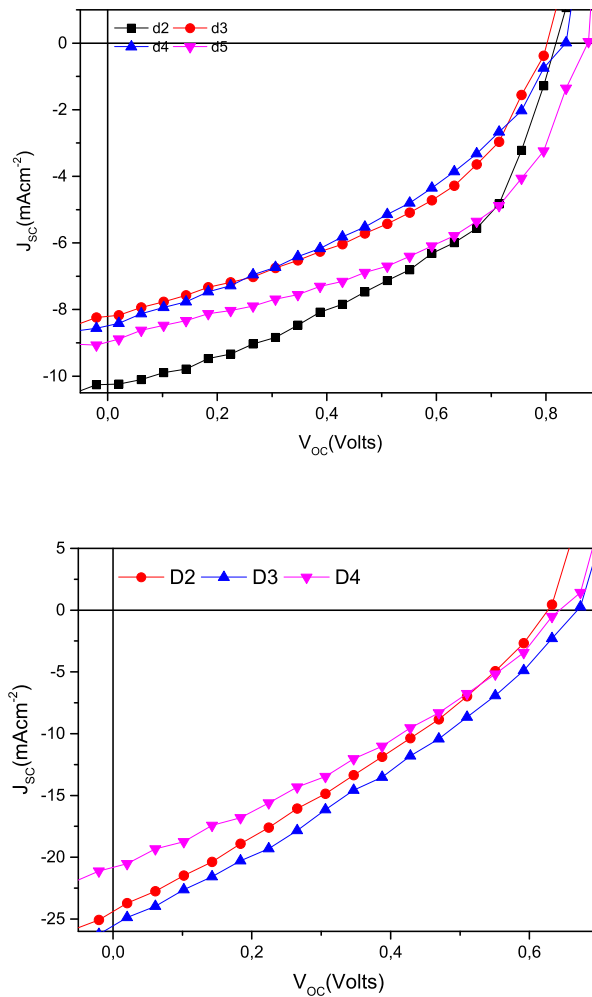


Fig. 5.2: J-V characteristic curves of device without and with Ag:Cu bimetallic nanoparticles.

in nano-composites size, which raised the recombination rate at the same time. The maximum power conversion efficiency recorded in this experiment with Ag:Cu was 6.28% which is 24% growth compared the reference cell with a PCE of 5.05%. In addition to the nano particles contribution in increasing inter facial area between active layer and HTL, they also exhibited the phenomenon called local surface plasmon resonance (LSPR) which can serve as light trapping mechanism through scattering. LSPR can also generate strong electromagnetic field in the vicinity of the nano -particle that could assist in exciton dissociations.

### 5.3.2 Charge Transport Properties Analysis

Current-voltage characteristics of the solar cells are measured under dark condition to understand the charge transport process in the devices. We employed space

charge limited current (SCLC) where all traps in the medium are filled and the charge mobility depends on the applied bias voltage. The SCLC data are compared to Mott-Gurney model which assumes that active layer is trap-free, current to be due to carriers of one polarity, carrier diffusion is negligible in active layer and electric field at the injecting electrode is zero [16–19]. Mott-Gurney equation was fitted to the SCLC data to obtain important charge transport parameters. It is to be noted here that the dark current are not affected by the LSPR since there is no interaction with electromagnetic radiation. However, the dark current exhibited improved device performance for the samples with Ag:Cu NPs doped hole transport layer compared pristine one. This is due to low series resistance as a result of improved conductivity of PEDOT:PSS transport layer [20, 21]. The charge mobilities and field activation factors (Table 5.2) derived from the solar cells are comparable to those reported in literatures.

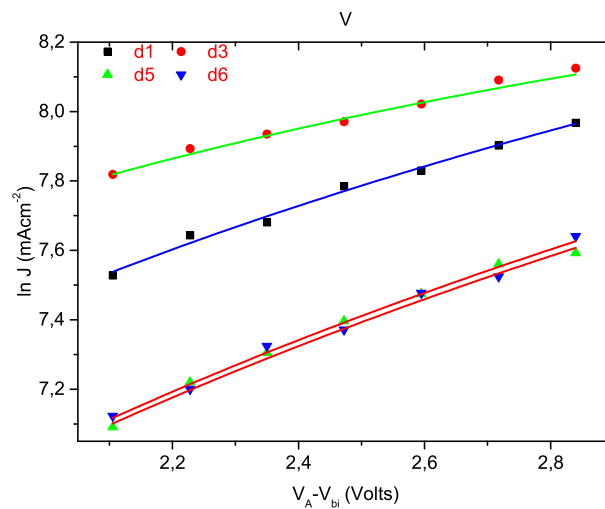


Fig. 5.3: Space Charge limited currents for device with and without Ag:Cu BNCs.

Tab. 5.2: Charge transport parameter for the best four fabricated devices

Device	$\mu_0/cm^2 V^{-1} S^{-1}$	$\gamma/(cm V^{-1})^{-\frac{1}{2}}$
Reference	$4.60 \times 10^{-4}$	$-2.1 \times 10^{-4}$
Diode 1	$2.14 \times 10^{-3}$	$-2.9 \times 10^{-4}$
Diode 2	$6.69 \times 10^{-4}$	$-5.2 \times 10^{-4}$
Diode 3	$8.45 \times 10^{-4}$	$-1.5 \times 10^{-4}$
Diode 4	$8.42 \times 10^{-4}$	$-1.5 \times 10^{-4}$

### 5.3.3 Optical Properties

Figure 5.4 shows the UV–Vis absorption spectra for both reference and devices with Ag:Cu BNPs which depend on the shape, size and surrounding environment of the synthesized nanoparticles. The effect of the nanoparticles structures is identified on the position and intensity of LSPR. The localized surface plasmon resonance (LSPR) characteristic bands maximum around 380 nm and 420 nm which indicates the contribution of Ag nanoparticles. The broad absorption bands of two humps at around 440 and 500nm corresponds to copper nanoparticles contribution [22, 23]. This could be as a result of lack of uniformity in the shape and size of the copper nanoparticles. It can be observed from UV/Vis absorption spectra (Fig. 5.4) that the Ag:Cu BNCs demonstrated broader optical absorption in the wavelength ranges of 420 nm to 510 nm and then decreases linearly up to 760 nm. The UV/Vis spectra further indicates red shift between the wavelength ranges 450 nm to 750 nm. This could attributed to the effect BNCs resulting from the two metallic nanoparticles complementing each other in enhancing optical absorption over a larger wavelength region from dual resonance enhancement of two different nanoparticles[16, 24].

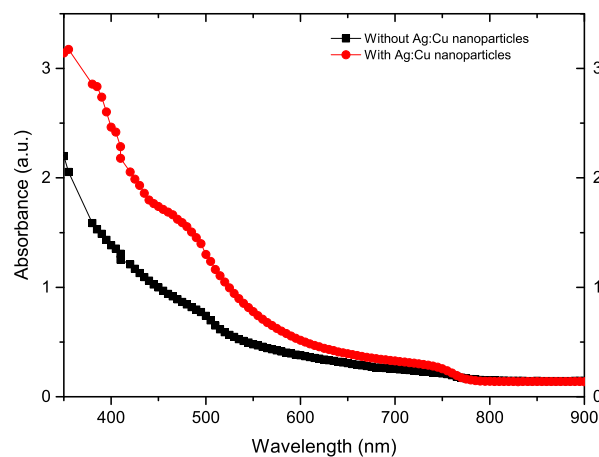


Fig. 5.4: U-V Optical absorbance of devices with and without Ag:Cu BNCs.

Tab. 5.3: EDX data of Ag:Cu core-shell nanoparticles

Sample	Element	Weight %	Atomic %
1	Ag	35.65	16.44
	Cu	50.09	39.22
2	Ag	38.68	11.95
	Cu	32.62	17.10
3	Ag	46.95	22.17
	Cu	38.23	30.64
4	Ag	28.45	12.87
	Cu	57.45	44.11

### 5.3.4 Morphology

#### *Scanning Electron Microscopy (SEM)*

Figure 5.5 depicts HRSEM images of the synthesized BNCs with and without PEDOT: PSS. Ag:Cu BNCs are eccentric core-shell nano-particles type with spherical shapes which are distinctly visible from each other. The silver and copper atoms uniformly distributed over the whole matrix. It is worth noting that incorporation of the nano-composite into the HTL exhibited no strong alteration between the PEDOT: PSS layers with and without BNCs except for slight agglomeration of Cu cores embedded in an Ag shells. This showed that Ag:Cu nano-particles were completely embedded in the PEDOT: PSS layer.

The composition and elemental mapping of prepared bimetallic nano-particles were obtained using an energy dispersive X-ray microanalysis system attached to the SEM. The Ag:Cu powder films were dispersed with deionised water on carbon disks. Figure 5c and Table IV shows the EDX spectra and composition percentages. The widespread distribution of Ag:Cu nanoparticle sizes could be as a result of agglomeration of Copper uncapped by PVP and inhomogeneous formation and nucleation of Cu nano-particles. Energy dispersive X-ray spectra (EDX) measurements were carried out for device to detect the distribution of PCBM /Ag:Cu and BNCs in perovskite film. The EDX spectrum confirms the presence of silver (Ag)and copper(Cu) as shown in table 5.4 and Figure 5.5c.

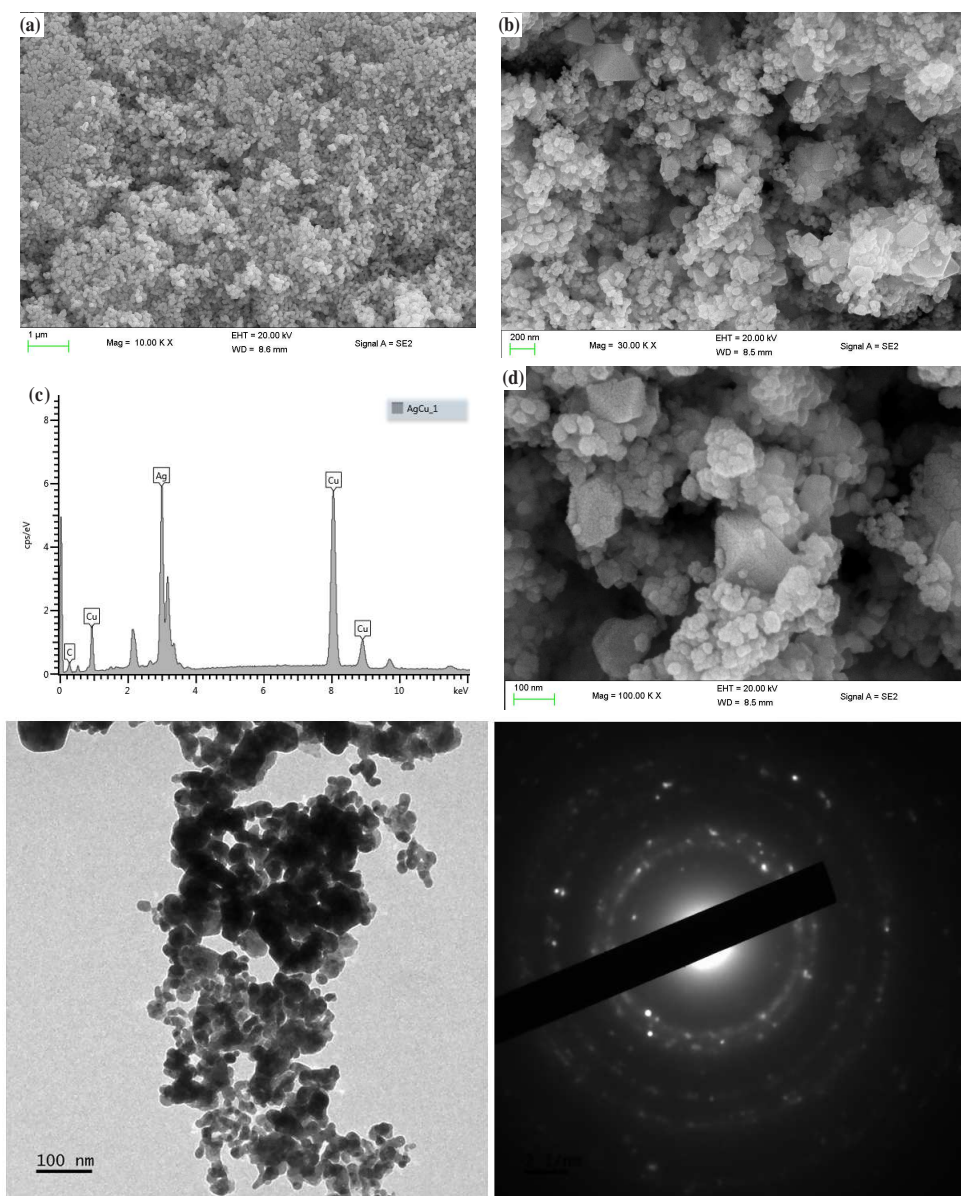


Fig. 5.5: Synthesized Ag:Cu nano-composite in powder form

### *Transmission Electron Microscopy Analysis (TEM)*

HRTEM analysis was conducted to investigate the physical size, distribution and morphology of the synthesized nano-particles. Figure 5.5 shows the images of Ag:Cu core-shell nanoparticles. It can be seen that the synthesized nanoparticles exhibit mostly spherical core-shell and somehow close to hexagonal structure. The particle distribution of the obtained Ag:Cu NPs is similar to that from our SEM observations.

Tab. 5.4: Analysis of XRD of Ag:Cu bimetallic nanoparticles.

Peak No.	$2\theta$ (degree)	$h k l$	FWHM ( $\beta$ )	$d$ (nm)
1	36.32	(111)	0.766	11.40
2	38.16	(111)	0.766	11.47
3	42.43	(111)	0.766	11.62
4	44.27	(200)	0.766	11.70
5	61.42	(220)	0.766	12.60
6	64.64	(220)	0.766	12.82
7	73.74	(220)	0.766	13.54
8	77.53	(311)	0.766	13.89
9	81.68	(222)	0.766	14.31

### X-Ray Diffraction (XRD) Study

Figure 5.6 shows the electron diffraction pattern of Ag:Cu core-shell structure nanoparticles synthesized by co reduction method. The sample exhibited nine distinct peaks at  $2\theta = 36.32^\circ, 38.16^\circ, 42.43^\circ, 44.27^\circ, 61.42^\circ, 64.64^\circ, 73.74^\circ, 77.53^\circ$  and  $81.68^\circ$ . The peaks corresponds to (111), (200), (220), (222) (311) planes of the face-

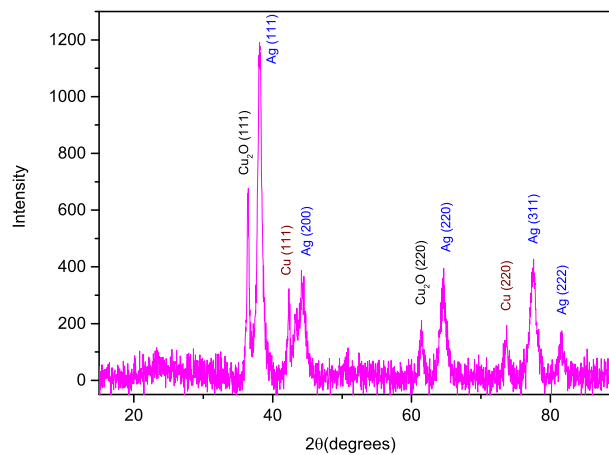


Fig. 5.6: XRD patterns of the synthesized (a) Ag: Cu NPs

centered cubic structure of silver metal and (111), (220) planes of the face-centered cubic structure of copper. The results obtained were in good agreement with the diffraction planes of pure silver (JCPDS 89-3722) and those of pure copper (JCPDS 85-1326). In addition the XRD pattern of the nanoparticles synthesized also displays for planes (111) and (220) peaks of copper oxide ( $\text{Cu}_2\text{O}$ ) which we attributed to partial oxidation of copper in ambient atmosphere. Our results further indicate that the crystallite size of the synthesized Ag:Cu nanoparticles determined using Scherrer's equation were distributed within the range of 11.40-14.31 nm as shown

in Table 5.5.

## 5.4 Conclusion

The influence of local surface plasmon resonance (LSPR) on perovskite solar cells was investigated by incorporating Ag:Cu NCs into the HTL. We demonstrated that incorporation of bimetallic nanocomposites in perovskite solar cell fabrication led to enhanced charge collection and improved performances. However, we have observed significant loss of the open circuit voltage due to energy level mismatches at the interface between active layer and the electrodes. Furthermore, the low device fill factor suggested the existence of leakage current that impedes device rectification. The use of metal nano-composite in HTL enhanced the device current density from  $12.50 \text{ mAcm}^{-2}$  to  $29.30 \text{ mAcm}^{-2}$  which corresponds to the change in PCE from 5.05% to 6.28%, respectively. The improvement in PCE was compromised due to the loss in open circuit voltage. Therefore, the incorporation of bimetallic nanocomposites in perovskite based solar cells can be promising strategy for enhancing both stability and PCE. However, Better strategies need to be investigated to mitigate the loss in  $V_{OC}$  and leakage current.

## Acknowledgments

This work is supported by National Research Foundation (NRF)(Grant numbers 92786 and 85589), South Africa.

## References

- [1] Kojima, A.; Teshima, K.; Shirai, Y.; Miyasaka, T., Organometal halide perovskites as visible-light sensitizers for photovoltaic cells. *Journal of the American Chemical Society* 2009, 131 (17), 6050-6051.
- [2] Jeon, N. J.; Noh, J. H.; Yang, W. S.; Kim, Y. C.; Ryu, S.; Seo, J.; Seok, S. I., Compositional engineering of perovskite materials for high-performance solar cells. *Nature* 2015, 517 (7535), 476-480.
- [3] Choy, W. C., The emerging multiple metal nanostructures for enhancing the light trapping of thin film organic photovoltaic cells. *Chemical Communications* 2014, 50 (81), 11984-11993.
- [4] Sha, W.; Choy, W.; Chew, W. In *Comprehensive study of plasmonic effects in organic solar cells*, 34th Progress In Electromagnetics Research Symposium, PIERS 2013, 2013.
- [5] Zhou, N.; Lopez-Puente, V.; Wang, Q.; Polavarapu, L.; Pastoriza-Santos, I.; Xu, Q.-H., Plasmon-enhanced light harvesting: applications in enhanced photocatalysis, photodynamic therapy and photovoltaics. *RSC Advances* 2015, 5 (37), 29076-29097.
- [6] Liu, X.; Wang, D.; Li, Y., Synthesis and catalytic properties of bimetallic nanomaterials with various architectures. *Nano Today* 2012, 7 (5), 448-466.
- [7] Lim, E. L.; Yap, C. C.; Teridi, M. A. M.; Teh, C. H.; bin Mohd Yusoff, A. R.; Jumali, M. H. H., A review of recent plasmonic nanoparticles incorporated P3HT: PCBM organic thin film solar cells. *Organic Electronics* 2016, 36, 12-28.
- [8] Gan, Q.; Bartoli, F. J.; Kafafi, Z. H., Plasmonic-enhanced organic photovoltaics: Breaking the 10% efficiency barrier. *Advanced materials* 2013, 25 (17), 2385-2396.

- 
- [9] Stratakis, E.; Kymakis, E., Nanoparticle-based plasmonic organic photovoltaic devices. *Materials Today* 2013, 16 (4), 133-146.
- [10] Chaudhuri, R. G.; Paria, S., Core/shell nanoparticles: classes, properties, synthesis mechanisms, characterization, and applications. *Chem. Rev* 2012, 112 (4), 2373-2433.
- [11] Garcia, M. A., Surface plasmons in metallic nanoparticles: fundamentals and applications. *Journal of Physics D: Applied Physics* 2011, 44 (28), 283001.
- [12] Delsante, S.; Borzone, G.; Novakovic, R.; Piazza, D.; Pigozzi, G.; Janczak-Rusch, J.; Pilloni, M.; Ennas, G., Synthesis and thermodynamics of Ag–Cu nanoparticles. *Physical Chemistry Chemical Physics* 2015, 17 (42), 28387-28393.
- [13] Zhao, J.; Zhang, D.; Zhang, X., Preparation and characterization of copper/silver bimetallic nanowires with core-shell structure. *Surface and Interface Analysis* 2015, 47 (4), 529-534.
- [14] Bansal, A.; Sekhon, J. S.; Verma, S., Scattering efficiency and LSPR tunability of bimetallic Ag, Au, and Cu nanoparticles. *Plasmonics* 2014, 9 (1), 143-150.
- [15] Chen, F.-C.; Wu, J.-L.; Lee, C.-L.; Hong, Y.; Kuo, C.-H.; Huang, M. H., Plasmonic-enhanced polymer photovoltaic devices incorporating solution-processable metal nanoparticles. *Applied Physics Letters* 2009, 95 (1), 182.
- [16] Lu, L.; Luo, Z.; Xu, T.; Yu, L., Cooperative plasmonic effect of Ag and Au nanoparticles on enhancing performance of polymer solar cells. *Nano Letters* 2012, 13 (1), 59-64.
- [17] Neumann, K.; Thelakkat, M., Perovskite solar cells involving poly (tetraphenylbenzidine) s: investigation of hole carrier mobility, doping effects and photovoltaic properties. *RSC Advances* 2014, 4 (82), 43550-43559.
- [18] Reid, O. G.; Munechika, K.; Ginger, D. S., Space charge limited current measurements on conjugated polymer films using conductive atomic force microscopy. *Nano letters* 2008, 8 (6), 1602-1609.
- [19] Moiz, S. A.; Khan, I. A.; Younis, W. A.; Karimov, K. S., Space Charge–Limited Current Model for Polymers. In *Conducting Polymers*, InTech: 2016.

- 
- [20] Kalfagiannis, N.; Karagiannidis, P.; Pitsalidis, C.; Panagiotopoulos, N.; Gravalidis, C.; Kassavetis, S.; Patsalas, P.; Logothetidis, S., Plasmonic silver nanoparticles for improved organic solar cells. *Solar Energy Materials and Solar Cells* 2012, 104, 165-174.
- [21] Li, X.; Deng, Z.; Yin, Y.; Zhu, L.; Xu, D.; Wang, Y.; Teng, F., Efficiency enhancement of polymer solar cells with Ag nanoparticles incorporated into PEDOT:PSS layer. *Journal of Materials Science: Materials in Electronics* 2014, 25 (1), 140-145.
- [22] Taner, M.; Sayar, N.; Yulug, I. G.; Suzer, S., Synthesis, characterization and antibacterial investigation of silver–copper nanoalloys. *Journal of Materials Chemistry* 2011, 21 (35), 13150-13154.
- [23] Paszkiewicz, M.; Gotabiewska, A.; Rajska, t.; Kowal, E.; Sajdak, A.; Zaleska-Medynska, A., Synthesis and characterization of monometallic (Ag, Cu) and bimetallic Ag-Cu particles for antibacterial and antifungal applications. *Journal of Nanomaterials* 2016, 2016, 6.
- [24] Li, X.; Choy, W. C.; Huo, L.; Xie, F.; Sha, W. E.; Ding, B.; Guo, X.; Li, Y.; Hou, J.; You, J., Dual plasmonic nanostructures for high performance inverted organic solar cells. *Advanced Materials* 2012, 24 (22), 3046-3052.

## 6. ELECTRON TRANSPORT CO-BUFFER LAYER FOR IMPROVED CHARGE EXTRACTION IN POLYMER SOLAR CELL

### **Abstract**

Silver: copper bimetallic nanoparticles were synthesized by co-reduction of silver and copper ions from silver and copper nitrates aqueous solutions. The effects of the synthesized Ag:Cu nanoparticles on polymer film solar absorber composed of poly(3-hexylthiophene) : phenyl-C61-butyric acid methyl ester (P3HT:PC<sub>61</sub>BM) was investigated in terms of changes in optical and electrical properties of the films. The nature of the metal nano-composite was studied using High-resolution scanning and transmission electron microscopy (HRSEM and HRTEM) respectively. The optical absorption of the solar absorber films were improved due to presence of surface plasmon resonance effect (SPR) caused by Ag:Cu nanoparticles that resulted in an increase in short-circuit current density ( $J_{sc}$ ) from 8.4 to 10 mAcm<sup>-2</sup> (19%) and improved power conversion efficiency (PCE) from 3.5 to 4.7% (34%).

### **6.1 Introduction**

Over the past few years there has been upsurge in the price of fossil fuels due to continuous rise in energy demand due to high growth of global population. This has propelled scientists and researchers to seek alternative sources of renewable energy to address challenge in environmental pollution and satisfy the ever increasing demand for energy. Third generation of solution processed thin film solar cell include; organic solar cells, tandem solar cells, dye sensitized solar cells, and hybrids (organic /inorganic based solar cells)[1–6]. Organic photovoltaic cells solar cells employ organic polymers and small molecules as the photoactive layer for light absorption and charge generation. In the last two decades lots of research efforts

have been focused on improving the device performance of organic photovoltaics. Polymer solar cells have attracted a lot of interest due to simplicity of solar cell fabrication, low temperatures, cheap manufacturing costs, flexibility, lightweight with possibility of large-scale production using roll to roll printing techniques. The short diffusion lengths of free charge carriers (electron-hole) in polymer medium has limited the thickness of the photoactive layer to ( $< 150$  nm). As a consequence, the solar absorber has reduced both optical absorption and low short-circuit current density in polymer based solar cells. The incorporation of metal nanoparticles as interfacial layers in organic photovoltaic solar cells has been reported to increase the light trapping and absorption without affecting the size of the photoactive layer. This is attributed to the LSPR effect and the light scattering effect of metal nanoparticles [7–14]. A wide variety of processing parameters are known to influence the morphology of the fabricated devices which explain why most experimental results do not give consistent results when repeated. Thick films are required for maximum absorption of solar radiation however light can easily escape the solar absorber in thin films which require a compromise strategy to balance between optical absorption and reduced series resistance of the solar absorber.

## 6.2 Materials and Methods

Acetone ( $C_3H_6O$ ), Poly(3,4-ethylenedioxythiophene)-poly(styrenesulfonate) (PEDOT: PSS), poly(3-hexylthiophene) (P3HT) and phenyl-C<sub>61</sub>-butyric acid methyl ester (PC<sub>61</sub>BM) were purchased from Ossila while Copper nitrate hydrate (99.999%  $Cu(NO_3)_2 \cdot H_2O$ ), silver nitrate (99.5%  $AgNO_3$ ), Sodium borohydride (99.98%  $NaBH_4$ ), chloroform, and Isopropyl alcohol ( $CH_3CHOHCH_3$ ) were from Sigma Aldrich. Polyvinyl Pyrrolidone (PVP molecular weight 25000-30000), Merck, Germany) was used as the capping agent while ascorbic acid (99.5%, Associated Chemicals Enterprises, South Africa) and  $NaBH_4$  was used as the reducing agents. All the chemicals were of analytical grade and used as purchased without further purification.

### 6.2.1 Synthesis of Ag:Cu Nanocomposite

The synthesis of the bimetallic nano-composite begins with the preparation of a solution from 2.5.0g of PVP and 0.9 of ascorbic acid which are separately dissolved

in 50 mL of deionized water. Then the two solutions are mixed and stirred at 60°C for 10 minutes. 0.20 M of copper (II) nitrate, 0.1 M silver nitrate aqueous solutions were also separately prepared by dissolving in deionized water and stirred for one hour in ice bath for 0.3 M Sodium borohydride. 50 mL solution of  $\text{Cu}(\text{NO}_3)_2 \cdot \text{H}_2\text{O}$  and 50 mL of  $\text{AgNO}_3$  were then simultaneously poured dropwise into 50 mL of  $\text{NaBH}_4$  solution with continued stirring for 20 minutes at room temperature. The obtained mixture were separated by centrifugation at 6000 rpm for 30 minutes, filtered, washed several times with deionized water and finally the precipitate left to dry at room temperature.

### 6.2.2 Device fabrication

The solar cells are fabricated using a solar absorber containing poly(3-hexylthiophene) and phenyl-C61-butyric acid methyl ester(P3HT:PC<sub>61</sub>BM) blend. The solution of the photo-active layer is prepared in chloroform solvent with and without the inclusion of the nanoparticles. Four different solutions of P3HT:PC<sub>61</sub>BM(1:1 weight ratio) in chloroform at 20mg/ml concentrations were prepared with 0, 2, 3 and 4% of Ag:Cu nanoparticles by weight. All the four blends were kept stirring at 40°C for four hours to obtain the uniform blends. The devices were fabricated on an indium tin oxide (ITO) coated glass substrate purchased from Luminescence Technology Corporation which were then cut to the size of 30 mm×30mm. The ITO substrate was partially etched with acid solution then ultrasonically cleaned successively in detergents, deionized water, acetone, and isopropyl alcohol for 15 min, respectively. It was then annealed at 120°C for 30 minutes. The solar cell fabrication begins by spin coating PEDOT: PSS on dried ITO coated glass substrate at 3500 rpm for 3 s then 60 s and annealed at 150°C. It is followed by a mixture 3% by weight of Ag:Cu nanoparticles and P3HT: PCBM in chloroform at 2500 rpm and annealed at 90°C for 5 minutes in nitrogen atmosphere. The samples are then transferred vacuum deposition unit where 0.4nm of Lithium fluoride and 60 nm aluminium electrode were deposited at a base pressure of  $10^{-6}$ . The device structure illustrating various layers of materials is provided in Figure. 6.1 The fabricated devices attains inverted planar-heterojunction solar cells with device architecture ITO/PEDOT:PSS:P3HT:PC<sub>60</sub>BM:Ag:Cu /LiF/Al.

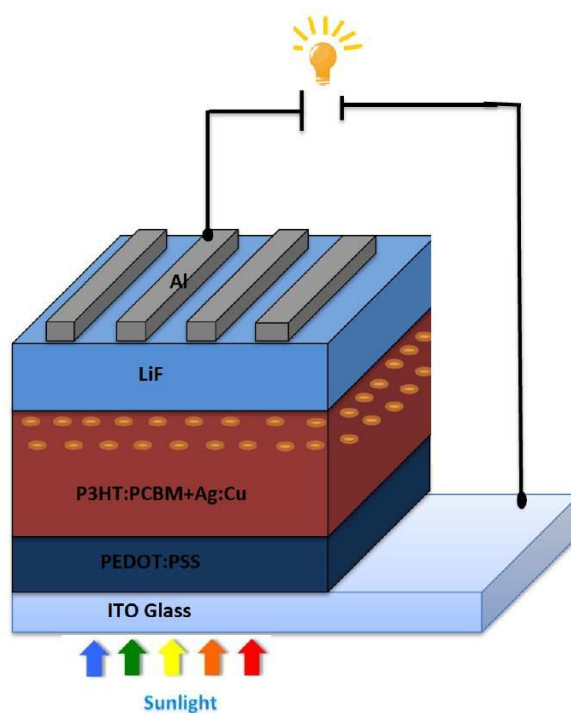


Fig. 6.1: Fabricated polymer solar cell structure.

## 6.3 Results and Discussion

### 6.3.1 J-V Characteristics

The current density–voltage (J–V) characteristics curves have been taken from the newly fabricated devices under 1 Sun light illumination at  $100 \text{ mW/cm}^2$  (AM1.5 solar spectrum) and dark condition. The first panel of Fig. 6.2 shows the J–V curves measured from the solar cells fabricated with metal nano-particles in the solar absorber. More photocurrent has been measured from the solar cells with metal NPs (see panel 2 to Fig. 6.2). The integration of the Ag:Cu nanoparticles into P3HT:PCBM binary blends extended the optical absorption range of solar spectrum. As a result charge extraction and transport properties were enhanced as reflected by higher short circuit current density and the power conversion efficiencies (PCEs) in the fabricated device compared to the pristine devices see Tables 6.1, 6.2 and Figure 6.2. The maximum current density measured in the current experiment was  $11.4 \text{ mA/cm}^2$ . However the performance of the devices highly depends on the amount of metal nanoparticles in the solar absorber of the devices. For example, the incorporation of the metal nanoparticles at the concentration of 3% by weight of Ag:Cu NPs into P3HT:PCBM: active layer increases the current density from  $8.0 \text{ mA/cm}^2$  to

11.4 mA/cm<sup>2</sup>. Moreover, the metal NPs increases charge mobility and conductivity of the solar absorber[15, 16]. It was also observed that both FF and  $V_{oc}$  decreases at higher concentrations of the metal nanoparticles which could be attributed to the current leakage in the solar cells caused by direct contact between Ag:Cu NPs and electrodes which resulted in electrons quenching. The devices incorporated with 3% Ag:Cu NPs produced the greatest enhancements in  $J_{sc}$  due to the dual effects of Ag and Cu NPs.

Tab. 6.1: J-V characteristic curves of reference solar cell without Ag:Cu NPs.

Device	$V_{OC}$ V	$J_{SC}$ mA/cm <sup>2</sup>	FF %	PCE %	R at $V_{oc}$ $\Omega$	R at $I_{sc}$ $\Omega$
Diode 1	0.59	8.0	53.5	3.3	205	4508
Diode 2	0.58	7.6	54.7	3.3	264	6452
Diode 3	0.56	7.3	53.5	3.1	383	3940
Diode 6	0.58	8.0	52.4	3.2	259	4213

Tab. 6.2: With Ag:Cu NPs.

Device	$V_{OC}$ V	$J_{SC}$ mA/cm <sup>2</sup>	FF %	PCE %	R at $V_{oc}$ $\Omega$	R at $I_{sc}$ $\Omega$
Diode 2	0.57	9.8	52.1	4.6	88	2627
Diode 4	0.57	11.4	53.3	4.7	336	2723
Diode 5	0.57	10.0	53.3	4.7	336	2723
Diode 6	0.55	9.1	47.0	3.5	162	2485

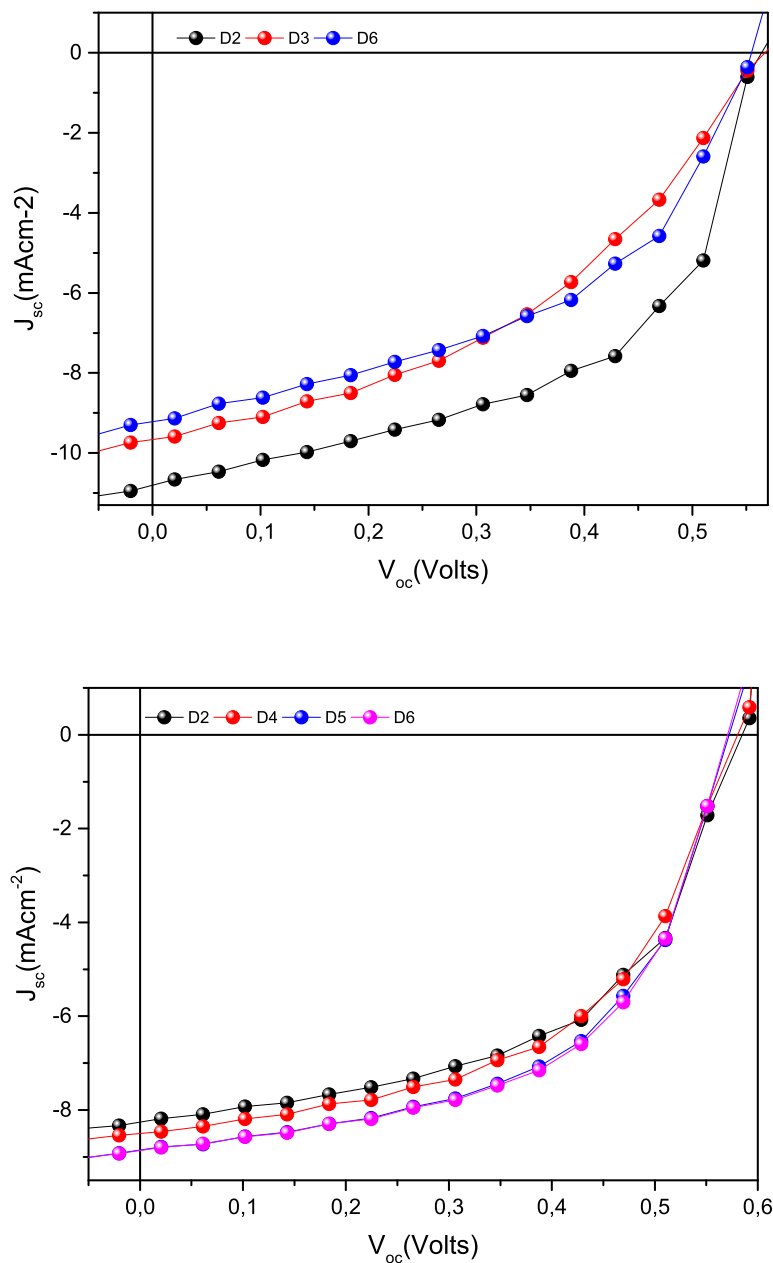


Fig. 6.2: J-V characteristic curves of solar cell with and without Ag:Cu BNCs.

### 6.3.2 Charge Transport Properties Analysis

Figure 6.3 displays the J-V curves recorded dark conditions for both types of devices fabricated with and without metal NPs. In both cases, the solar cell diodes shows a rectification behaviour and the amount of current appeared to be similar in the forward voltage. However, in reverse voltage the devices devices with silver copper bimetallic nanoparticles shows a higher dark current density and better

rectification compared to those without. This suggest a reduction in both carrier recombination and leakage current and consequently improved carrier transport and collection which could be partly due to improved polymer morphology. Blending the metal nanoparticles (NPs) into an active layer effectively decreases series resistance, improve the carrier mobility and increases cell efficiency[17]

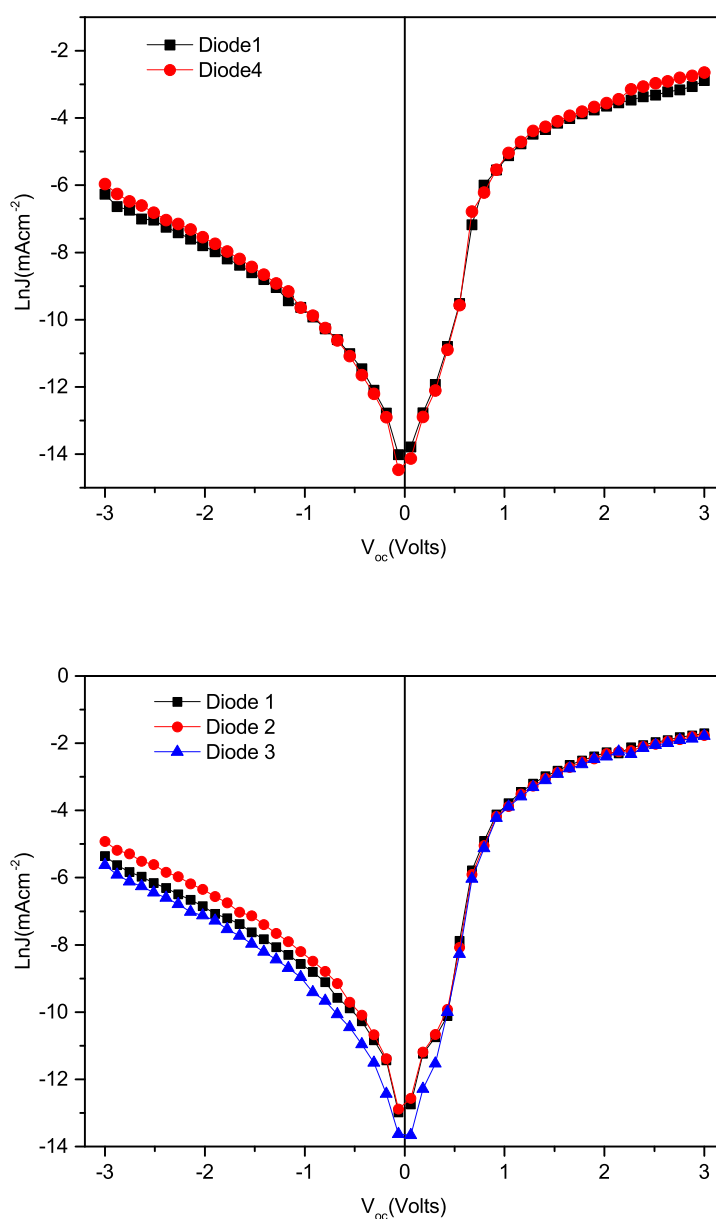


Fig. 6.3: Dark Ln J-V characteristic curves of device without(a) and with Ag:Cu BNCs (b).

*Charge mobility* The carrier mobility was derived from the space charge limited current (SCLC) model at low voltage using the field-dependent form of the Mott–Gurney law. Mott–Gurney equation ignores the effect of diffusion, assumes current to be

due to carriers of one polarity only.

$$J_{SCLC} = \frac{9}{8} \varepsilon_r \varepsilon_0 \mu_0 \frac{(V - V_{bi})^2}{L^3} \exp\left(\sqrt{\frac{V - V_{bi}}{L}}\right) \quad (6.1)$$

which may be expressed as

$$J = \frac{9}{8} \varepsilon_r \varepsilon_0 \mu_0 \frac{V^2}{L^3} \quad (6.2)$$

where  $\varepsilon_r$  is the relative permittivity of the medium,  $\varepsilon_0$  is the permittivity of the vacuum,  $\mu_0$  is the mobility,  $V$  and  $V_{bi}$  are the applied and inbuilt voltages respectively and  $L$  is the thickness of the photoactive layer.

$$V_{in} = V - V_{bi} - V_{sr} \quad (6.3)$$

Where,  $V$  is the applied voltage,  $V_{bi}$  is the built-in voltage and  $V_{sr}$  is the voltage dropped due to the series resistance. The results were fitted to a space charge limited form in order to extract the mobility from the SCLC region of the curve. According Figure 6.4, the model agrees well with the measured SCLC from the solar cells. The zero field mobility derived from the fits and summerised in table 6.2 are comparable to the values provided in literatures.

Tab. 6.3: Charge transport parameter for the best three fabricated devices

Device	$\mu_0/\text{cm}^2\text{V}^{-1}\text{S}^{-1}$	$\gamma/(\text{cmV}^{-1})^{-\frac{1}{2}}$
reference	$5.08 \times 10^{-4}$	$-1.1 \times 10^{-4}$
1	$8.50 \times 10^{-3}$	$-5.8 \times 10^{-4}$
2	$8.39 \times 10^{-3}$	$-5.6 \times 10^{-4}$
3	$8.39 \times 10^{-3}$	$-5.6 \times 10^{-4}$

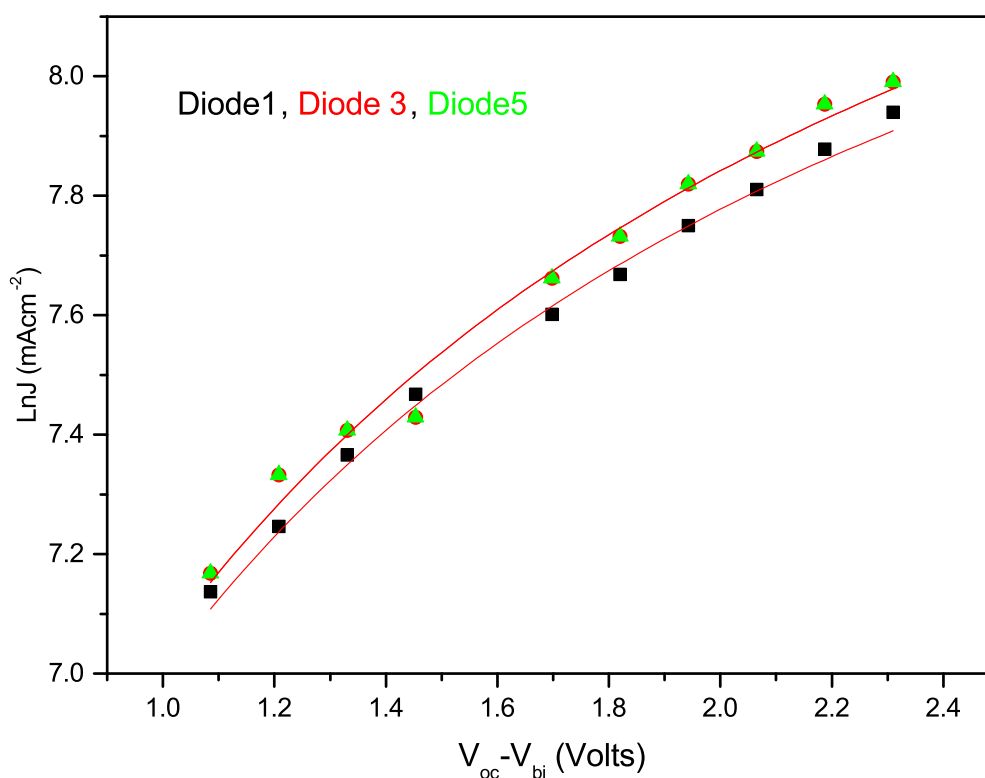


Fig. 6.4: Space charge limited current for the best 3 fabricated devices

## 6.4 Optical Properties

### 6.4.1 UV/Vis Analysis

The optical absorption of the photoactive films containing different concentrations Ag:Cu nanoparticles were investigated using UV-Vis spectrophotometer. The spectra were taken for films composed of ITO/PEDOT:PSS/ P3HT:PCBM:Ag:Cu. Glass and ITO was taken as the references for baseline subtraction and do not have absorption

in the visible and infrared regions. The spectra provided in Figure 6.5 shows two humps (broad absorption spectrum) which are attributed to LSPR and the polymer blend. The first hump appearing between 350 and 410nm corresponding to that of Ag nanoparticles (410nm) and the second (a hump) appears in all the samples between 450 to 625nm associated with P3HT and the surface plasmonic resonance range of Cu nanoparticles around 600nm[18]. The samples with 2% and 3% Ag:Cu nanoparticles are shifted to longer wavelengths see Figure 6.5 These are in agreement with those reported in literature.

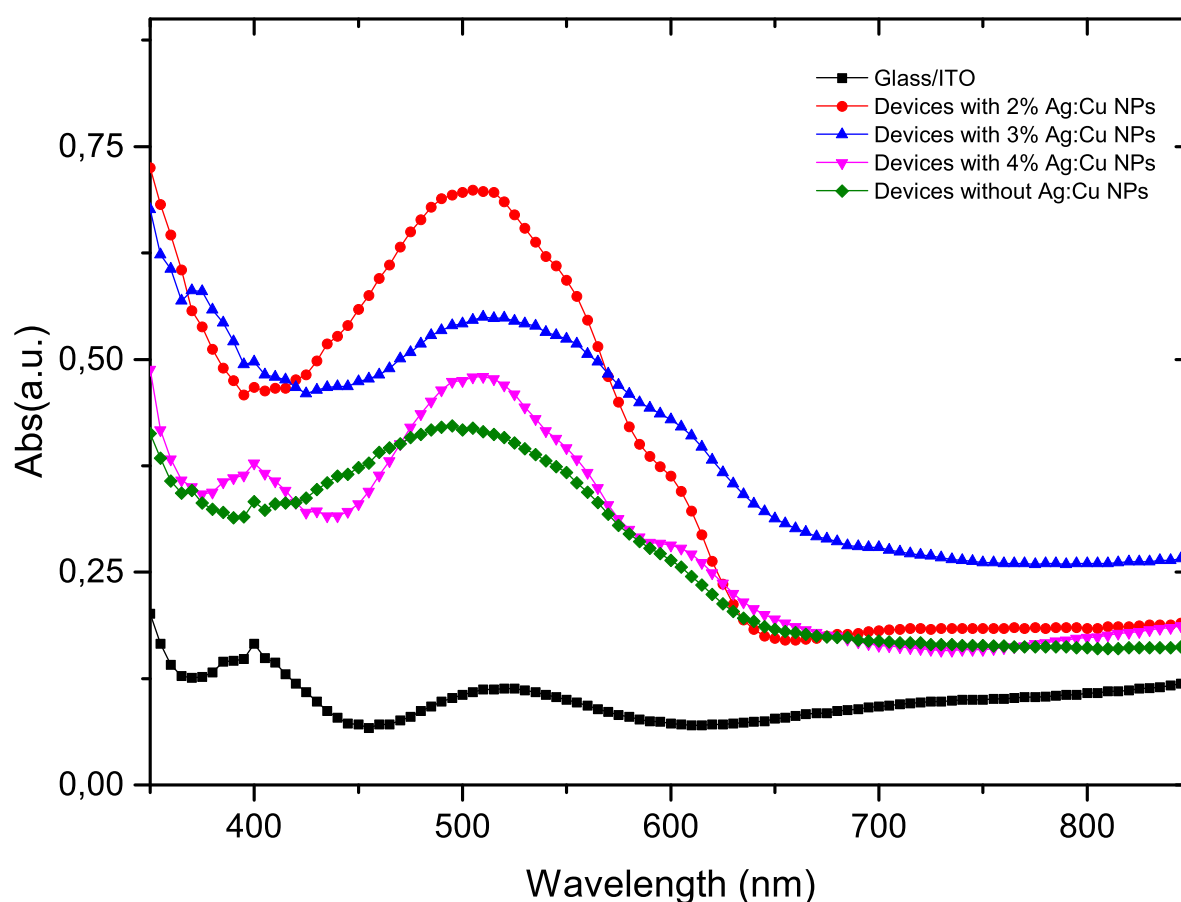


Fig. 6.5: U-V Optical absorbance of devices with and without Ag:Cu BNPs.

## 6.5 Morphology

### 6.5.1 Scanning Electron Microscopy (SEM)

The characterization of the synthesized metal nanoparticles were conducted using a number of spectrometers. The surface morphology and elemental mapping of the synthesized Ag:Cu nanoparticles were carried out using HRSEM. Figure 6.6 shows the uniform distribution of the elemental silver and copper powder as indicated by various colours. The SEM image show the flower-like structure containing uniformly distributed elements and well dispersed particles of nearly the same size. It is evident from the SEM images that there are hexagonal pyramid like structures suggesting the formation of a uniform silver shell over the surface of the Cu nanoparticles as confirmed by TEM analysis. In fact, in some instances the TEM images showed an incomplete phase of the core shell type structure as well as single phase which can be characterized by the different colours of the images. The presence of such diverse nano-particles structures would promote the occurrence of LSPR excitation at the small size of the nanoparticles and multiple scattering of light inside the photoactive layer. The interpenetrating network of the dispersed nanoparticles provided alternative pathways for charge transport which resulted in enhanced PCE. A high dispersion of NPs in the active layer improves carrier mobility and results in improved power conversion efficiency[19].

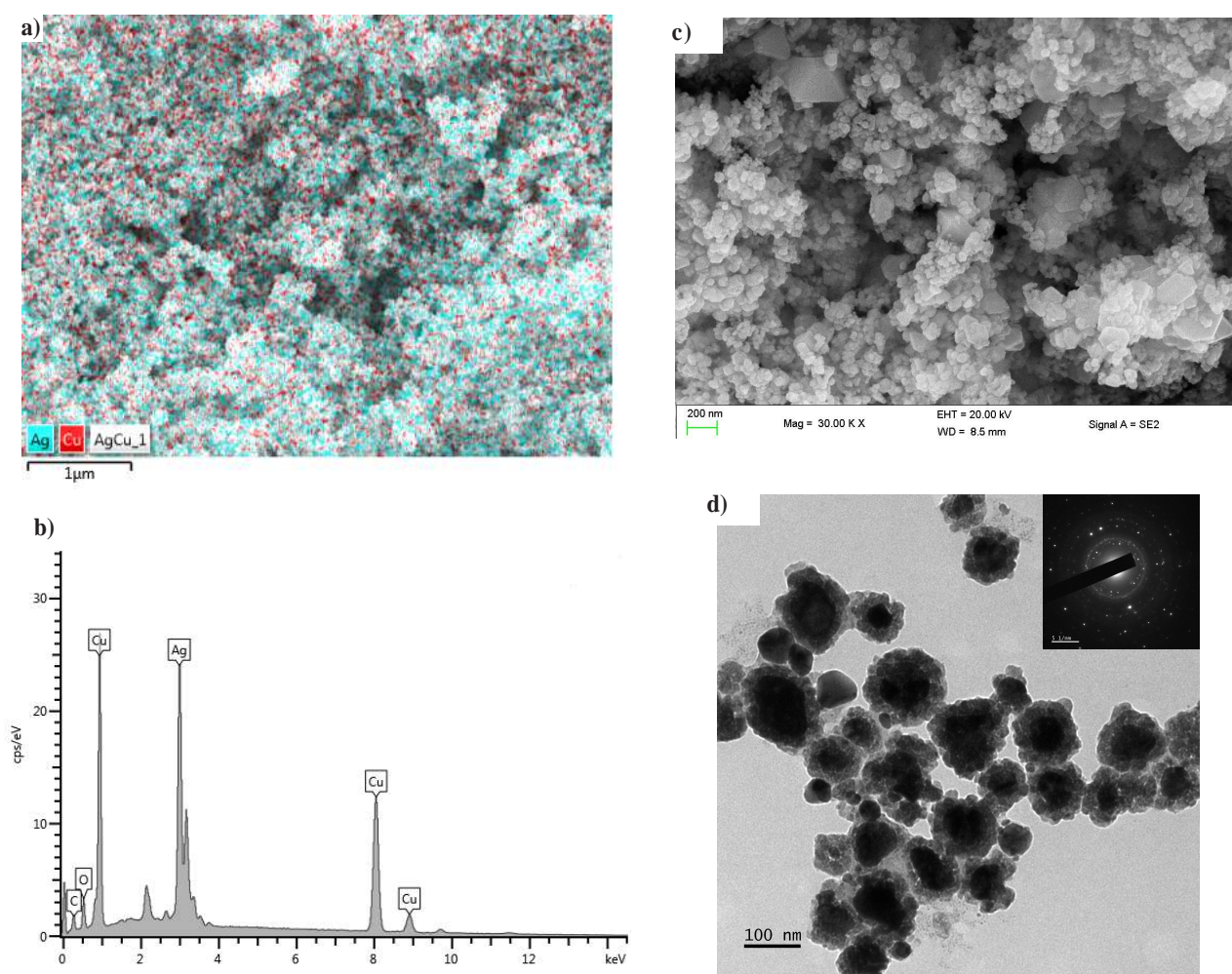


Fig. 6.6: SEM micrographs showing surface morphology with elemental mapping of Ag:Cu BNCs powder

Furthermore the energy dispersive X-ray Energy dispersive X-ray spectra (EDX) measurements were carried out determine the elemental and percentage distribution of silver and copper on the synthesized bimetallic nanoparticles. According to the information derived from the EDX spectrum confirms the presence of silver (Ag) and copper (Cu) at different concentrations as shown in table 6.4 and Figure 6.7. TEM images taken from powder phase of metal nanoparticles is given in Figure 6.8 which clearly shows the formation of various shapes, structures and sizes of the bimetallic nanocomposites. According to TEM images provided in Figure 6.8, the nanoparticles exhibited spherical shape although they are close to core-shell (Cu@Ag) bimetallic nanoparticles. This indicated that Cu nanoparticles were first formed by reduction of  $\text{Cu}(\text{NO}_3)_2 \cdot \text{H}_2\text{O}$  by  $\text{NaBH}_4$  which then acted as a seed where silver nanoparticles dispersed on it to form core-shell structure. Copper and silver nanoparticles were evenly distributed over the whole cluster shown in Figure

Tab. 6.4: EDX data of Ag-Cu core-shell nanoparticles

Sample	Element	Weight %	Atomic %
1	Ag	35.65	16.44
	Cu	50.09	39.22
2	Ag	38.68	11.95
	Cu	32.62	17.10
3	Ag	46.95	22.17
	Cu	38.23	30.64
4	Ag	28.45	12.87
	Cu	57.45	44.11

6.8. The results further confirmed that the silver nanoparticles uniformly covered copper nanoparticles. The ring-like diffraction pattern alongside in Figure 6.8b indicates that the synthesized bimetallic NPs are crystalline structures.

### 6.5.2 X-Ray Diffraction (XRD) Study

The XRD patterns of the Ag: Cu bimetallic nanoparticles as shown in Figure 6.9 consists of strong peaks for (111), (200), (220), (222) and (311) planes corresponding to Ag face-centred cubic (fcc) structure. While the (111) and (220) also consistent with the (fcc) phase of pure copper (JCPDS 85-1326)[20, 21]. The relatively high-diffraction intensity of the (1 1 1) compared with that of the (2 0 0), (2 2 0), (2 2 2) and (3 1 1) for Ag nanoparticles suggests that the (1 1 1) plane was the predominant. These peaks also match to the Ag standard spectrum (JCPDS No. 89-3722), indicating presence of pure Ag nanoparticles in the prepared sample[15]. The XRD pattern of the nanoparticles synthesized also displays for planes (111) and (220) peaks of copper oxide ( $\text{Cu}_2\text{O}$ ). This indicates that the synthesized silver shell did not prevent oxide formation at the surface of the copper core and as a result some copper nanoparticles was partially oxidized in ambient atmosphere despite the use of PVP as a capping agent[20, 22, 23]. The average size of nanoparticles, determined by the Scherrer's equation, was estimated to range between 9.90 nm to 12.42 nm as provided in table 6.5.

Tab. 6.5: Analysis of XRD of Ag:Cu bimetallic nanoparticles.

Peak No.	$2\theta$ (degree)	$h k l$	FWHM ( $\beta$ )	$d$ (nm)
1	36.5	(111)	0.883	9.90
2	38.2	(111)	0.883	9.94
3	42.35	(111)	0.884	10.08
4	44.42	(200)	0.885	10.15
5	61.39	(220)	0.885	10.93
6	64.49	(220)	0.833	11.11
7	73.55	(220)	0.884	11.73
8	77.45	(311)	0.883	12.04
9	81.70	(222)	0.883	12.42

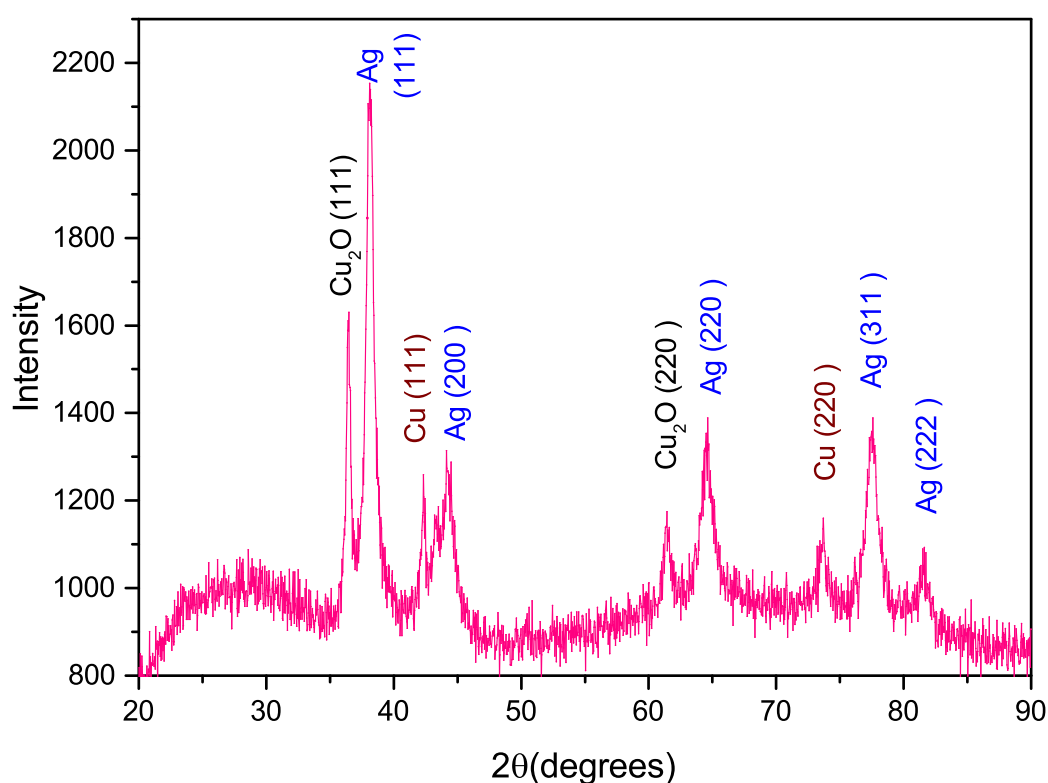


Fig. 6.7: XRD patterns of the synthesized (a) Ag: Cu NPs

## Conclusion

The effect of silver:copper nanoparticles in organic molecules solar absorber was investigated. The results clearly demonstrated that plasmonic bimetallic nanoparticles can significantly enhance the solar cell performance because of the LSPR effect in the photoactive medium. The overall enhancement in power conversion efficiency

of the devices was largely due to contribution of the bimetallic nanoparticles. The study provides a facile cost effective method for preparation of bimetallic nanoparticles and subsequent incorporation in the fabrication of OPV. The method can be extended to obtain both organic/inorganic semiconductor functional nanoparticles for fabrication of gas sensors and other photonic devices. Further research needs to be carried out to precisely control the size and determine the shape of the nanoparticles for specific applications.

## **Acknowledgments**

This work is partially supported by National Research Foundation (NRF)(Grant numbers 92786 and 85589), South Africa.

## References

- [1] Huang, H.; Huang, J., Organic and Hybrid Solar Cells. Springer: 2014.
- [2] Tiwari, S.; Tiwari, T.; Carter, S. A.; Scott, J. C.; Yakhmi, J., Advances in Polymer-Based Photovoltaic Cells: Review of Pioneering Materials, Design, and Device Physics. In Handbook of Ecomaterials, Springer: 2018; pp 1-48.
- [3] Oseni, S. O.; Mola, G. T., Properties of functional layers in inverted thin film organic solar cells. Solar Energy Materials and Solar Cells 2017, 160, 241-256.
- [4] Tonui, P.; Oseni, S. O.; Sharma, G.; Yan, Q.; Mola, G. T., Perovskites photovoltaic solar cells: An overview of current status. Renewable and Sustainable Energy Reviews 2018, 91, 1025-1044.
- [5] Mbuyise, X. G.; Arbab, E. A.; Kaviyarasu, K.; Pellicane, G.; Maaza, M.; Mola, G. T., Zinc oxide doped single wall carbon nanotubes in hole transport buffer layer. Journal of Alloys and Compounds 2017, 706, 344-350.
- [6] Arbab, E. A.; Mola, G. T., V<sub>2</sub>O<sub>5</sub> thin film deposition for application in organic solar cells. Applied Physics A 2016, 122 (4), 1-8.
- [7] Lu, L.; Luo, Z.; Xu, T.; Yu, L., Cooperative plasmonic effect of Ag and Au nanoparticles on enhancing performance of polymer solar cells. Nano Letters 2012, 13 (1), 59-64.
- [8] Omrani, M. K.; Fallah, H., Improving light trapping of polymer solar cell via doping a new array of triple core-shell spherical nanoparticles utilizing realistic modeling. Solar Energy 2018, 163, 600-609.
- [9] Liu, K.; Bi, Y.; Qu, S.; Tan, F.; Chi, D.; Lu, S.; Li, Y.; Kou, Y.; Wang, Z., Efficient hybrid plasmonic polymer solar cells with Ag nanoparticle decorated TiO<sub>2</sub> nanorods embedded in the active layer. Nanoscale 2014, 6 (11), 6180-6186.

- [10] Lim, E. L.; Yap, C. C.; Teridi, M. A. M.; Teh, C. H.; bin Mohd Yusoff, A. R.; Jumali, M. H. H., A review of recent plasmonic nanoparticles incorporated P3HT: PCBM organic thin film solar cells. *Organic Electronics* 2016, 36, 12-28.
- [11] Chen, X.; Zuo, L.; Fu, W.; Yan, Q.; Fan, C.; Chen, H., Insight into the efficiency enhancement of polymer solar cells by incorporating gold nanoparticles. *Solar Energy Materials and Solar Cells* 2013, 111, 1-8.
- [12] Enrichi, F.; Quandt, A.; Righini, G. C., Plasmonic enhanced solar cells: Summary of possible strategies and recent results. *Renewable and Sustainable Energy Reviews* 2018, 82, 2433-2439.
- [13] Taleatu, B.; Omotoso, E.; Lal, C.; Makinde, W.; Ogundele, K.; Ajenifuja, E.; Lasisi, A.; Eleruja, M.; Mola, G., XPS and some surface characterizations of electrodeposited MgO nanostructure. *Surface and Interface Analysis* 2014, 46 (6), 372-377.
- [14] Arularasu, M.; Anbarasu, M.; Poovaragan, S.; Sundaram, R.; Kanimozhi, K.; Magdalane, C. M.; Kaviyarasu, K.; Thema, F.; Letsholathebe, D.; Mola, G. T., Structural, optical, morphological and microbial studies on SnO<sub>2</sub> nanoparticles prepared by co-precipitation method. *Journal of nanoscience and nanotechnology* 2018, 18 (5), 3511-3517.
- [15] Sarkar, J.; Bhattacharyya, M.; Kumar, R.; Mandal, N.; Mallik, M., Synthesis and characterizations of Cu–Ag core–shell nanoparticles. *Advanced Science Letters* 2016, 22 (1), 193-196.
- [16] Kalfagiannis, N.; Karagiannidis, P.; Pitsalidis, C.; Panagiotopoulos, N.; Gravalidis, C.; Kassavetis, S.; Patsalas, P.; Logothetidis, S., Plasmonic silver nanoparticles for improved organic solar cells. *Solar Energy Materials and Solar Cells* 2012, 104, 165-174.
- [17] Vangelidis, I.; Theodosi, A.; Beliatis, M. J.; Gandhi, K. K.; Laskarakis, A.; Patsalas, P.; Logothetidis, S.; Silva, S. R. P.; Lidorikis, E., Plasmonic Organic Photovoltaics: Unraveling Plasmonic Enhancement for Realistic Cell Geometries. *Acs Photonics* 2018, 5 (4), 1440-1452.

- [18] Miyakawa, M.; Hiyoshi, N.; Nishioka, M.; Koda, H.; Sato, K.; Miyazawa, A.; Suzuki, T. M., Continuous syntheses of Pd@ Pt and Cu@ Ag core-shell nanoparticles using microwave-assisted core particle formation coupled with galvanic metal displacement. *Nanoscale* 2014, 6 (15), 8720-8725.
- [19] He, Y.; Liu, C.; Li, J.; Zhang, X.; Li, Z.; Shen, L.; Guo, W.; Ruan, S., Improved power conversion efficiency of inverted organic solar cells by incorporating Au nanorods into active layer. *ACS applied materials & interfaces* 2015, 7 (29), 15848-15854.
- [20] Choi, E.; Lee, S.; Piao, Y., A solventless mix-bake-wash approach to the facile controlled synthesis of core-shell and alloy Ag-Cu bimetallic nanoparticles. *CrystEngComm* 2015, 17 (31), 5940-5946.
- [21] Hikmah, N.; Idrus, N.; Jai, J.; Hadi, A. In Synthesis and characterization of silver-copper core-shell nanoparticles using polyol method for antimicrobial agent, IOP Conference Series: Earth and Environmental Science, IOP Publishing: 2016; p 012050.
- [22] Aslan, E.; Patir, I. H.; Ersoz, M., Cu nanoparticles electrodeposited at liquid-liquid interfaces: a highly efficient catalyst for the hydrogen evolution reaction. *Chemistry-A European Journal* 2015, 21 (12), 4585-4589.
- [23] Kheawhom, S.; Panyarueng, P., Synthesis and Characterization of Copper-Silver Core-Shell Nanoparticles by Polyol Successive Reduction Process. *MRS Online Proceedings Library Archive* 2014, 1630.

## 7. CONCLUSION

Over the last two decades there has been great improvement towards the realization of solution processable thin film solar cells. A lot of effort has been invested to attain commercial grade power conversion efficiency from organic molecule based photovoltaic cells (OPV). However, because of the limitations of the polymer solar absorber and low charge carrier mobilities in the medium the efficiency of OPV reaches as close as 13%. Thus, OPVs having benefited from material development, preparation conditions and device optimization over the years to attain the results. On the other hand perovskites based solar cells have achieved a remarkable improvement with power conversion efficiency over 22% within a short period of time (less than ten years). This is attributed to wide optical absorption range, high charge mobilities and diffusion length compared to OPV solar absorber. Reproducibility, stability, durability and lifetime in addition to use of toxic lead and chlorinated solvents in perovskite still remain major challenges for commercialization. It is envisaged that with the current understanding more details about hybrid solar cells will be uncovered that will allow the design and fabrication of more efficient photovoltaic devices.

The current investigation intended to address some of the challenges facing perovskite and organic solar cell through the use of metal nano-particles. We have conducted an efficient and cost effective method to synthesis metal nano-composite particularly Ag:Zn and Ag:Cu. The nanocomposite were tested at various layers of the device structure to improve solar cell performance and stability. We have achieved a number experimental results which are reported in chapter 4, 5, and 6. Most of whom are already published in referred journals. Despite measuring enhanced photo-current, from the use of metal nano-particles at different layers of the device structure, it is noted however that metal nano-composite induces leakage current which reduces device fill factor and open circuit voltages.

Generally, the overall photovoltaic performance depends on the improvement of the

---

$V_{oc}$  and  $J_{sc}$  and FF), hence, more research attention should be geared towards the development of narrow bandgap materials to increase optical absorption and harvest more in the red and infrared regions of the solar spectrum. There is a need to find interfacial buffer layers which have appropriate alignment with HOMO and LUMO levels to match the donor with acceptor in order to maximize exciton generation and charge extraction. The concentration of synthetic nanoparticles are bound to increase in the near future hence there is need to examine fully and understand their harmful effect on human and environment.